DEUTSCHES ELEKTRONEN-SYNCHROTRON

in der HELMHOLTZ-GEMEINSCHAFT

DESY 08-118

August 2008

arXiv:0808.1846v1 [physics.acc-ph] 13 Aug 2008

Theory of Edge Radiation

Gianluca Geloni, Vitali Kocharyan, Evgeni Saldin, Evgeni Schneidmiller and Mikhail Yurkov

Deutsches Elektronen-Synchrotron DESY, Hamburg

ISSN 0418-9833

NOTKESTRASSE 85 - 22607 HAMBURG

Theory of edge radiation

Gianluca Geloni, Vitali Kocharyan, Evgeni Saldin,
Evgeni Schneidmiller and Mikhail Yurkov

Deutsches Elektronen-Synchrotron (DESY), Hamburg, Germany

Abstract

We formulate a complete theory of Edge Radiation based on a novel method relying on Fourier Optics techniques. Similar types of radiation like Transition Undulator Radiation are addressed in the framework of the same formalism. Special attention is payed in discussing the validity of approximations upon which the theory is built. Our study makes consistent use of both similarity techniques and comparisons with numerical results from simulation. We discuss both near and far zone. Physical understanding of many asymptotes is discussed. Based on the solution of the field equation with a tensor Green's function technique, we also discuss an analytical model to describe the presence of a vacuum chamber. In particular, explicit calculations for a circular vacuum chamber are reported. Finally, we consider the use of Edge Radiation as a tool for electron beam diagnostics. We discuss Coherent Edge Radiation, Extraction of Edge Radiation by a mirror, and other issues becoming important at high electron energy and long radiation wavelength. Based on this work we also study the impact of Edge Radiation on XFEL setups and we discuss recent results.

Key words:
edge radiation, near-field, undulator transition radiation, electron-bunch diagnostics, x-ray free-electron laser (XFEL)
PACS: 41.60.Cr, 42.25.-p, 41.75.-Ht

1 Introduction

Synchrotron Radiation (SR) sources from bending magnets are brilliant, and cover the continuous spectral range from microwaves to X-rays. However, in order to optimally meet the needs of basic research with SR, it is desirable to provide specific radiation characteristics, which cannot be obtained from bending magnets, but require special magnetic setups, called insertion devices. These are installed along the particle beam path between two bending magnets, and introduce no net beam deflection. Therefore, they can be incorporated in a given beamline without changing its geometry. Undulators are a typical example of such devices, generating specific radiation characteristics in the short wavelength range.

The history of SR utilization in the long wavelength region (from micrometer to millimeter) is more recent than that in the short wavelength range. Long wavelength SR sources may have a strong potential for infrared spectroscopy or imaging techniques. In fact, they are some order of magnitude brighter than standard thermal sources in the same spectral range.

Large angles are required to extract long wavelength SR from bending magnets, because the "natural" opening angle in this case increases up to several tens milliradians in the far-infrared range. However, the situation changes dramatically if a straight section is introduced between two bends, like in Fig. 1(a). Long-wavelength radiation emitted by relativistic electrons in this setup is called Edge Radiation (ER), and presents a significantly smaller opening angle than standard SR from bends (see, among others, [1]-[14]). In other words, in the long wavelength region (compared to the critical bending-magnet radiation wavelength) a simple straight section between bends can play the role of a kind of insertion device.

ER and bending magnet radiation have equivalent brightness. In fact, the physical process of ER emission is not different from that of radiation emission from a single bend. However, radiation from the setup in Fig. 1(a) exhibits special features. Due to a narrower opening angle of ER over SR from bends, as the wavelength gets longer ER yields significant advantages in terms of simplicity of the photon beamline.

ER theory is a part of the more general SR theory, very much like Undulator Radiation (UR) theory is a part of SR theory. Similarly to the UR case, also for ER the knowledge of the applicability region of the far-field formulas and corrections for near-field effects are of practical importance. In most practical cases, the distance between ER source and observer (i.e. the first optical element of the photon beamline) are comparable or even much smaller than the length of the straight section, which plays the role of the length of the

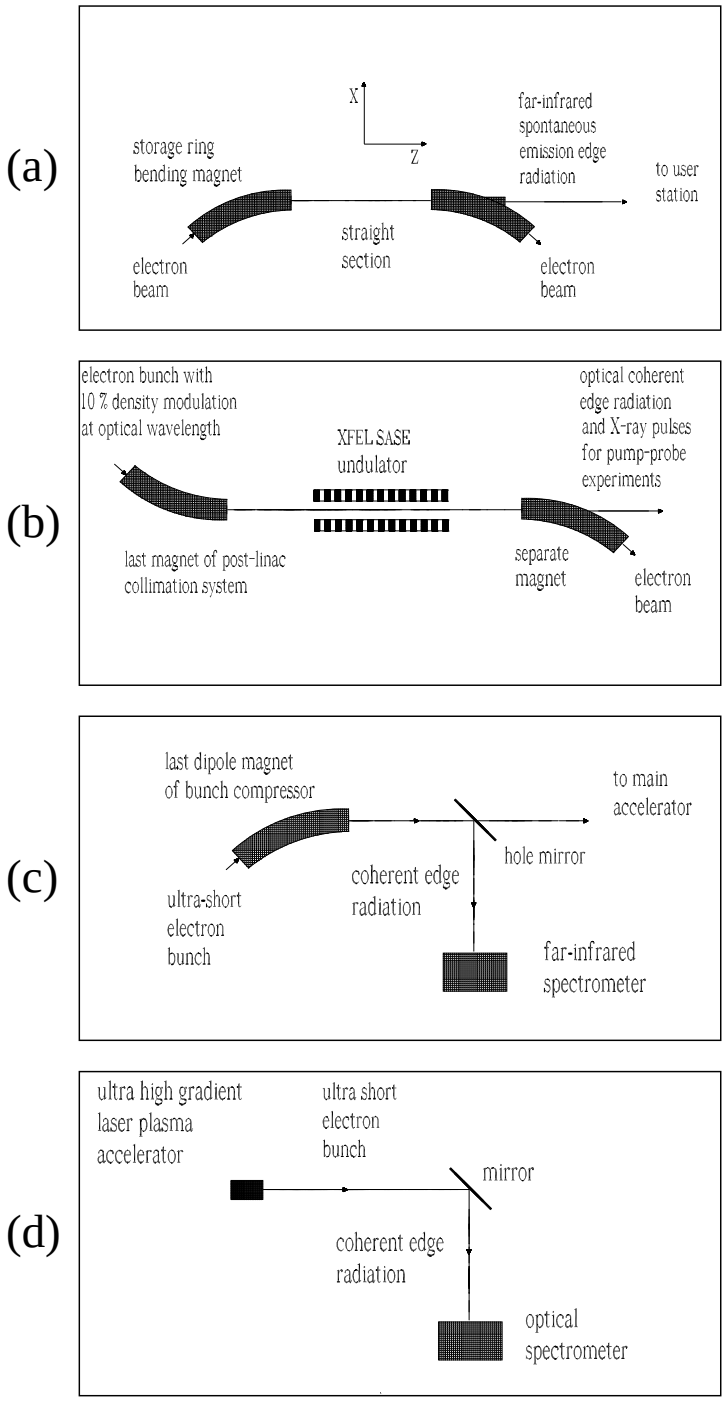

Fig. 1. Four main types of edge radiation setups: (a) Far-infrared beamline for synchrotron radiation source using edge radiation. (b) Arrival-time monitor for XFEL source using optical coherent edge radiation. (c) Electron bunch length monitor for XFEL using far-infrared coherent edge radiation. (d) Ultra-short electron bunch diagnostic for laser-plasma accelerator facility using optical coherent edge radiation.

insertion device for ER.

In this paper we developed a theory of near-field ER based on Fourier Optics (FO) techniques. These techniques can be exploited without limitations for ER setups, because the paraxial approximation can always be applied in the case of electrons in ultra-relativistic motion [15]. The use of the paraxial approximation allows reconstruction of the field in the near-zone from the knowledge of the far-field data. The solvability of the inverse problem for the field allows characterization of any ER setup, starting from the far-zone field, in terms of virtual sources. These sources exhibit a plane wavefront, and can be pictured as waists of laser-like beams. Using this kind of description we develop our theory in close relation with laser-beam optics. In particular, usual FO can be exploited to characterize the field at any distance, providing a tool for designing and analyzing ER setups.

It is the purpose of this article to discuss the principles of production and properties for all applications of ER. First, we treat the relatively simple case of ER from a setup composed by straight section and two bending magnets at its ends (see Fig. 1(a)). We begin calculating an analytical expression for ER from a single electron in the far-zone. Then, we characterize the near-zone with the help of the virtual-source technique. Two alternative techniques for the field propagation are given, based on a single virtual source located in the middle of the ER setup, and based on two virtual sources located at its edges.

Based on this study-case we turn to analyze a more complicated setup, consisting of an undulator preceded and followed by two straight sections and two bends (see Fig. 1(b)). ER from this kind of setup is commonly known as Transition Undulator Radiation (TUR). The first study on TUR appeared more than a decade ago in [16]. In that work it was pointed out for the first time that, since an electron entering or leaving an undulator experiences a sudden change in longitudinal velocity, highly collimated radiation with broadband spectrum, similar to transition radiation, had to be expected in the low-frequency region in addition to the usual UR. Reference [16] constitutes a theoretical basis for many other studies. Here we remind only a few [9, 17, 18, 19, 20], dealing both with theoretical and experimental issues. More recently, TUR has been given consideration in the framework of X-ray Free-Electron Laser (XFEL) projects like [21, 22, 23]. For example, an arrival-time monitor for XFELs using infrared coherent ER from a setup similar to that in Fig. 1(b) has been proposed in [24], which should be used for pump-probe experiments with femtosecond-scale resolution. In view of these applications, there is a need to extend the characterization of TUR to the near-zone, and to the coherent case. From this viewpoint, specification of what precedes and follows the undulator is of fundamental importance. As has been recognized for TUR many years ago [9], if this information

is not known, any discussion about the intensity distribution of TUR is meaningless. According to our approach, the two straight sections and the undulator in the setup in Fig. 1(b) will be associated to virtual sources with plane wavefronts. The field from the setup can then be described, in the near as well as in the far-zone, as a superposition of laser-like beams, radiating at the same wavelength and separated by different phase shifts.

Our study makes consistent use of both dimensional analysis and comparisons with outcomes from numerical simulation. All simulations in this paper are performed with the help of the computer code SRW [25].

There are, however, situations when existing computer codes cannot predict the radiation characteristics. One of these is the case when perturbations of the long-wavelength radiation by vacuum chambers are present, which may potentially affect the performance of ER setups. Since the diffraction size of the THz radiation exceeds the vacuum chamber dimensions, characterization of far-infrared ER must be performed accounting for the presence of a waveguide. In order to deal with this situation we developed a theory of ER in a waveguide. The task to be solved differs from the unbounded-space case only in the formulation of boundary conditions. The paraxial approximation applies as in the unbounded-space case. Only, on perfectly conducting walls the electric field must be orthogonal to the vacuum chamber surface. As in the unbounded-space case, one can use the Green's function approach to solve the field equations. The presence of different boundary conditions complicates the solution of the paraxial equation for the field, which can nevertheless be explicitly found by accounting for the tensorial nature of the Green's function. Here we take advantage of a mode expansion approach to calculate ER emission in the metallic waveguide structure. We solve the field equations with a tensor Green's function technique, and we extract figure of merits describing in a simple way the influence of the vacuum chamber on the radiation pulse as a function of the problem parameters. We put particular emphasis on a vacuum chamber with circular cross-section, which is natural for future linac-based sources (XFELs and Energy Recovery Linacs (ERLs) [26]).

Finally, we address the long-standing interest of electron beam characterization for linac-based sources and laser-plasma accelerators. One possibility to perform electron-beam diagnostics in these kind of facilities is to use coherent ER. This is an attractive tool, because it can provide valuable and detailed information on the electron beam. By detecting coherent ER, 3D distributions, divergence, micro-bunching may be measured in principle (See Figs. 1(c) and (d)). Usually, electrons in accelerators are highly collimated and monochromatic. In this case, coherent ER can be used for longitudinal and transverse beam-size monitoring. In contrast to this, electrons generated in laser-plasma interactions have different properties compared with

those in conventional accelerators. Namely, in this case, electrons have both divergence angle and energy distribution. We address applications of coherent ER by studying, first, the relatively simple case when only the influence of longitudinal and transverse structure factor of the electron bunch is accounted for. In particular, we give particular attention to the case when microbunching at optical wavelengths is imprinted onto an electron bunch, and we analyze the more complicated case of a bunch produced in a laser-plasma accelerator, i.e. accounting for divergence angle distribution of the beam. Energy distribution can be easily accounted for, based on this analysis. The problem of extraction of ER by a mirror, strictly related to diagnostics applications, is included too.

2 General relations for edge radiation phenomena

2.1 Physical discussion of some numerical experiment

This Section constitutes an attempt to introduce ER theory to readers in as intuitive and simple a fashion as possible by simulating the angular spectral flux as a function of observation angles for the geometry in 1(a). For this purpose we take advantage of the code SRW [25], which provides a numerical solution of Maxwell's equations.

The origin of a Cartesian coordinate system is placed at the center of straight section. The z-axis is in the direction of straight section and electron motion is in xz plane. Parameters of the problem are the radiation wavelength λ, the radius of the bend R, the relativistic Lorentz factor γ, the length of the straight section L and, additionally, the position of the observation plane down the beamline, z. We work in the far zone. In this Section it is operatively defined as a region where z is large enough, so that the simulated angular spectral flux does not show dependence on z anymore.

ER carries advantages over bending magnet radiation in the limit for $\lambda\!\!\!^{-}/\lambda\!\!\!^{-}_c \gg 1$, where $\lambda\!\!\!^{-}_c \sim R/\gamma^3$ (here $\lambda\!\!\!^{-} = \lambda/(2\pi)$ is the reduced wavelength) is the critical wavelength of bending magnet radiation. We will work, therefore, in this limit. We set $\gamma = 3.42 \cdot 10^4$ (17.5 GeV), $R = 400$ m, which are typical values for XFELs. Note that in this case $\lambda_c \simeq 0.1$Å. Here we take $\lambda = 400$ nm. We begin with the case $L = 0$ (bending magnet), and we increase the straight section length (see Fig. 2). As one can see from the figure, radiation becomes more collimated, up to about $L \simeq \gamma^2 \lambda\!\!\!^{-} \simeq 100$ m (case (d)), where the collimation angle reaches $1/\gamma \sim 30\mu$rad. Further increase of L only leads to the appearance of finer structures in the radiation profile. It is important to remark that the total number of photons in the ±1 mrad window shown

in Fig. 2(a) is roughly the same in the $\pm 100 \mu$rad window in Fig. 2(d). It is clear that the length of the straight section L is strongly related with the collimation of the radiation.

2.2 Similarity techniques

To study ER further we apply similarity techniques. Similarity is a special symmetry where a change in scale of independent variables can be compensated by a similarity transformation of other variables. This is a familiar concept in hydrodynamics, where the cardinal example is given by the Reynolds number. Similarity allows one to reduce the number of parameters to a few dimensionless ones that are directly linked to the physics of the process, and that control it in full. Such parameters are found by analysis of the underlying equations characterizing the system under study. In this Section we limit ourselves to list them, to show their correctness with the help of the code SRW, and to describe their physical meaning. This allows one to obtain general properties of the ER process. A comprehensive theory of ER will be presented in the following Sections.

For the setup in Fig. 1(a), two dimensionless parameters controlling the radiation characteristics can be extracted from Maxwell's equations. In the next Section we will show how these parameters can be derived. Here we limit ourselves to write them:

$$\delta \equiv \frac{\sqrt[3]{R^2 \lambda\!\!\!^{-}}}{L}, \quad \phi \equiv \frac{L}{\gamma^2 \lambda\!\!\!^{-}}. \tag{1}$$

The detector is supposed to be far away from the source so that the above-given definition of far-zone holds.

The most important general statement concerning ER is that all possible situations correspond to different values of the two dimensionless parameters δ and ϕ.

Note that the working limit $\lambda\!\!\!^{-}/\lambda\!\!\!^{-}_c \gg 1$ means $\phi \cdot \delta \ll 1$ in terms of dimensionless parameters. For any two cases characterized by the same values of δ and ϕ the angular spectral flux from set up in Fig. 1(a) will "look" the same in terms of angles scaled to $\sqrt{\lambda\!\!\!^{-}/L}$, i.e. $\hat{\theta} = \theta/\sqrt{\lambda\!\!\!^{-}/L}$. In other words, data for different sets of problem parameters corresponding to the same values of δ and ϕ reduce to a single curve when properly normalized. We tested the scaling properties of ER by running numerical simulations with the first principle computer code SRW. We used two different sets of dimensional parameters corresponding to the same case in terms of parameters δ and ϕ,

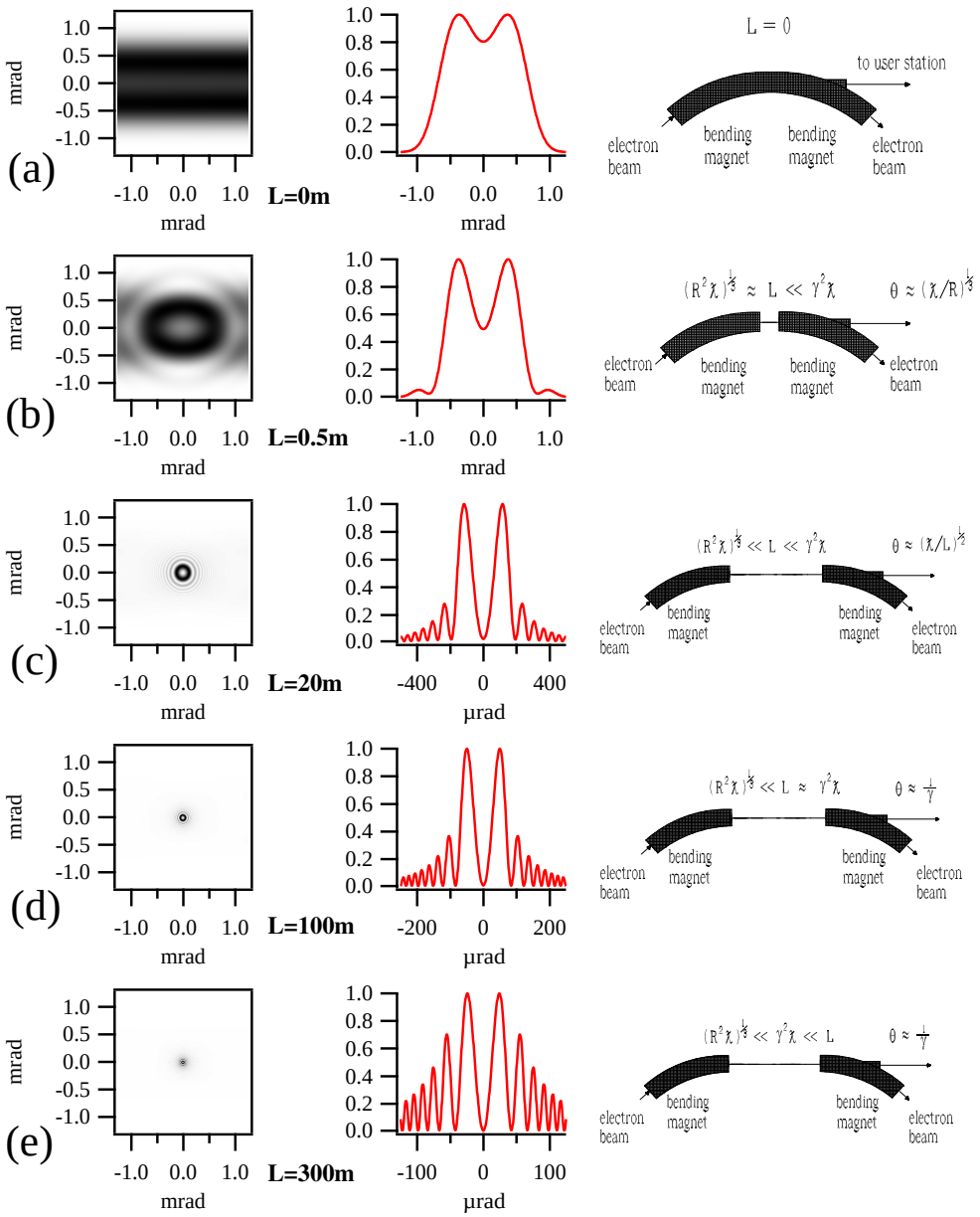

Fig. 2. Illustrative calculations of the effect of bending magnet separation on the directivity diagram of the radiation. The bending magnet radius $R = 400$ m, the relativistic factor $\gamma = 3.42 \cdot 10^4$, and the wavelength of interested $\lambda = 400$ nm are fixed, while the straight section length varies from $L = 0$ up to $L \gg \gamma^2 \lambda \simeq 100$ m. In this setup (as well as in all others in this paper) $\lambda \gg \lambda_c \simeq 0.1$Å. Case (a) is a bending magnet setup. Case (b) is a complex setup, where the radiation beam divergence is practically the same as in (a). Case (c) illustrates an ER setup. Bending magnet separation dramatically lowers the radiation beam divergence. (d) Optimal bending magnet separation. The straight section length $L \simeq \gamma^2 \lambda$ corresponds to a radiation beam divergence $\theta \simeq 1/\gamma$. (e) Further increase of L only leads to the appearance of finer structures in the radiation profile. 2D plots on the left show the angular spectral flux as a function of the horizontal and vertical angles θ_x and θ_y for various lengths of the straight section. Middle plots are obtained cutting the 2D angular spectral flux profile at $x = 0$. Right plots show a schematic of the considered layout.

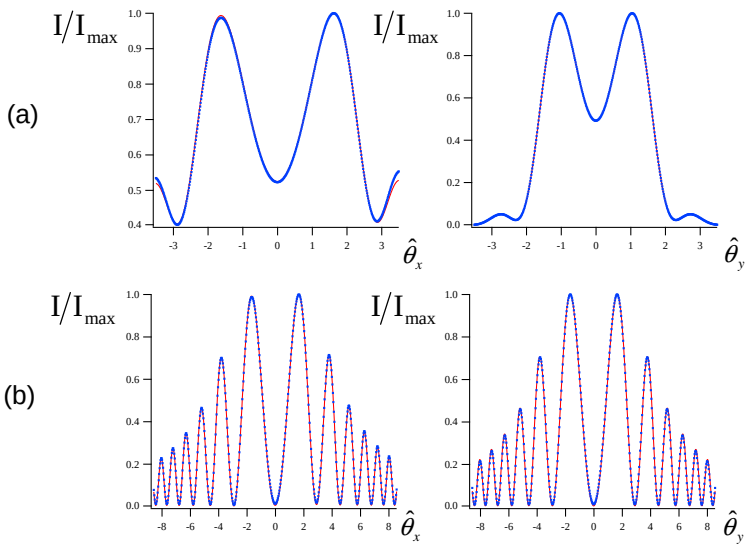

Fig. 3. Verification of similarity techniques. Left and right plots show the normalized angular spectral flux as a function of the horizontal and vertical angles $\hat{\theta}_x$ and $\hat{\theta}_y$ respectively (at $\hat{\theta}_y = 0$ and $\hat{\theta}_x = 0$ respectively). (a) Case $\delta \simeq 0.43$ and $\phi \simeq 6.7 \cdot 10^{-3}$. Solid curve is the result of SRW calculations with $L = 0.5$ m, $R = 400$ m, $\lambda = 400$ nm at 17.5 GeV. Dotted curve is the result for $L = 1$ m, $R = 800$ m, $\lambda = 800$ nm at 17.5 GeV. (b) Case $\delta \ll 1$ and $\phi \simeq 4$. Solid curve is the result of SRW calculations with $L = 300$ m, $R = 400$ m, $\lambda = 400$ nm, at 17.5 GeV (corresponding to $\delta \simeq 7 \cdot 10^{-4}$). Dotted curve is the result for $L = 150$ m, $R = 400$ m, $\lambda = 800$ nm at 8.5 GeV (corresponding to $\delta \simeq 2 \cdot 10^{-3}$).

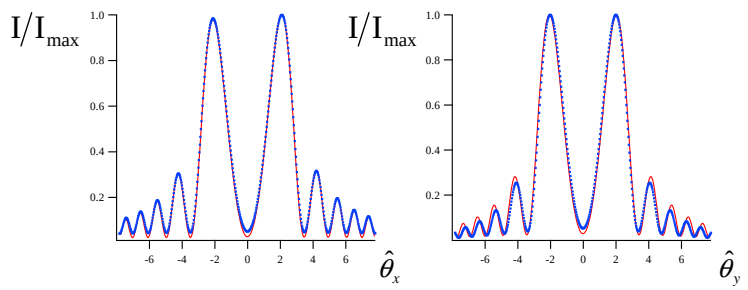

Fig. 4. Illustration of self-similarity techniques. Left and right plots show the normalized angular spectral flux as a function of the horizontal and vertical angles $\hat{\theta}_x$ and $\hat{\theta}_y$ respectively (at $\hat{\theta}_y = 0$ and $\hat{\theta}_x = 0$ respectively). The angular spectral flux profile asymptotically approaches the self-similar form $I/I_{\max} = F(\hat{\theta}_x, \hat{\theta}_y)$ for $\delta \ll 1$ and $\phi \ll 1$. Solid curve is the result of SRW calculations with $\delta \simeq 0.02$ and $\phi \simeq 0.13$. Dotted curve is refers to the case $\delta = 0.01$ and $\phi = 0.27$ instead.

and we checked that the angular spectral fluxes normalized to their maximal values are identical. Results are presented in Fig. 3 and Fig. 4, where the normalized angular spectral flux is indicated with $I/I_{\max}$.

When $\delta \sim 1$, the presence of the bending magnet radiation strongly influences the radiation profile (see Fig. 3(a)). When δ decreases up to $\delta \ll 1$, one

can neglect bending magnet contributions (see Fig. 3(b)): what is left in this case is ER. These situations are realized, for example, if one works at fixed $\lambda\!\!\!^{-}$, γ and R while increasing the length L as in the case of Fig. 2. It follows that δ is responsible for the relative weight of ER and bending magnet radiation contributions in the radiation profile. Since we are interested in ER emission, it is natural to consider more in detail the limit for $\delta \ll 1$. In this case, results are independent on the actual value of δ, and the only parameter left is ϕ. This fact can be seen from Fig. 3(b), where the two sets of dimensional parameters refer to two different value of $\delta \ll 1$. We will name this situation the sharp-edge asymptote.

In the limit for $\phi \ll 1$, the opening angle of the radiation is independent of the actual value of ϕ too. In this case we obtain the universal plot shown in Fig. 4, and one talks about a self-similar behavior of the angular spectral flux profile, which asymptotically approaches the self-similar form $I/I_{\max} = F(\hat{\theta}_x, \hat{\theta}_y)$. Note that the separation distance L between the bends dramatically lowers the radiation beam divergence, but the characteristic angle of emission is still larger than $1/\gamma$. In fact, radiation peaks at $\theta \simeq 2.2\sqrt{\lambda\!\!\!^{-}/L}$. When ϕ increases, radiation becomes better and better collimated, up to angles $\theta \sim 1/\gamma$. This happens for values $\phi \simeq 1$. Radiation has reached the best possible collimation angle and further increase of ϕ (see Fig. 3(b)) only modifies fine structures in the radiation profile.

2.3 Qualitative description

It is possible to present intuitive arguments to explain why all problem parameters (R, γ, L and $\lambda\!\!\!^{-}$) are effectively grouped in δ and ϕ.

To this purpose let us consider first the parameter δ. By definition, $1/\delta$ is a measure of the straight section length L in units of a characteristic length $\sqrt[3]{R^2\lambda\!\!\!^{-}}$.

To explain the meaning of the quantity $\sqrt[3]{R^2\lambda\!\!\!^{-}}$, following [27] we consider Fig. 5(a), and we focus on the region of parameters $\lambda\!\!\!^{-} \ll R$ and $\gamma^2 \gg 1$. A posteriori, this region of parameters will turn out to correspond to an angular dimension along the trajectory $2\theta \ll 1$ within the bending magnet. Radiation from an electron passing through the setup is observed through a spectral filter by a fixed observer positioned on the tangent to the bend at point P. Electromagnetic sources propagate through the system, as a function of time, as shown in Fig. 5(b). However, electromagnetic signals emitted at time t' at a given position $x(t')$ arrives at the observer position at a different time t, due to finite speed of light. As a result, the observer in Fig. 5(a) sees the electromagnetic source motion as a function of t. What one

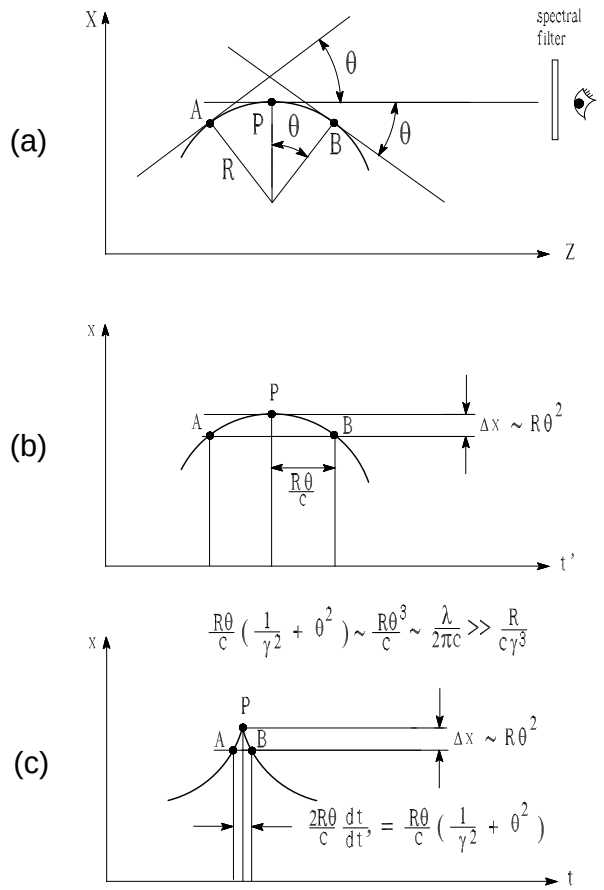

Fig. 5. Geometry for SR from a bending magnet.

needs to know, in order to calculate the electric field, is the apparent motion $x(t)$ shown in Fig. 5(c), which is a hypocycloid, and not the real motion $x(t')$. In fact, the electric field at the observation point is proportional to the second derivative of the x-coordinate with respect to the retarded time t, because the observer sees everything as delayed. We discuss the case when the source is heading towards the observer. Using the fact that $\theta \ll 1$, one obtains the well-known relation $dt/dt' = 1/2 \cdot (1/\gamma^2 + \theta^2)$. The observer sees a time-compressed motion of the sources, which go from point A to point B in an apparent time corresponding to an apparent distance $2R\theta dt/(dt')$. Let us assume (this assumption will be justified in a moment) $\theta^2 > 1/\gamma^2$. In this case one has $2R\theta dt/(dt') \simeq R\theta^3$. Obviously one can distinguish between radiation emitted at point A and radiation emitted at point B only when $R\theta^3 \gg \lambda\!\!\!^{-}$, i.e. for $\theta \gg (\lambda\!\!\!^{-}/R)^{1/3}$. This means that, as concerns the radiative process, we cannot distinguish between point A and B on the bend such that $R\theta \lesssim (R^2\lambda\!\!\!^{-})^{1/3}$. It does not make sense at all to talk about the position where electromagnetic signals are emitted within $L_{fb} = (R^2\lambda\!\!\!^{-})^{1/3}$ (here we are assuming that the bend is longer than L_{fb}). This characteristic length is called the formation length for the bend. The formation length can also be considered as a longitudinal size of a single-electron source. Note that

a single electron always produces diffraction-limited radiation $d \cdot \Delta\theta \sim \lambda\!\!\!^{-}$, d being the transverse size and $\Delta\theta$ the divergence of the source. Since $d \sim L_{fb}\Delta\theta$, it follows that the divergence angle $\Delta\theta$ is strictly related to L_{fb} and $\lambda\!\!\!^{-}$: $\theta \sim \sqrt{\lambda\!\!\!^{-}/L_f}$. One may check that, using $L_{fb} \sim \sqrt[3]{R^2\lambda\!\!\!^{-}_c}$, one obtains $\theta \sim \sqrt[3]{\lambda\!\!\!^{-}/R}$; in particular, at $\lambda\!\!\!^{-} \sim \lambda\!\!\!^{-}_c \sim R/\gamma^3$ one obtains $\theta \sim 1/\gamma$, as is well-known for bending magnet radiation.

Let us now consider the case of a straight section of length L inserted between the two halves of a bend. Since we cannot distinguish between points within L_{fb}, the case $L = 0$ is obviously indistinguishable from the case $L \ll L_f$. Significant deviations from the bending magnet case are to be expected when $L \gtrsim L_{fb}$, i.e. when $\delta \lesssim 1$. This hints to the fact that δ is responsible for the relative weight of ER and bending magnet radiation contributions in the radiation profile.

Let us now discuss the parameter ϕ. By definition, ϕ is a measure of the straight section length L in units of a characteristic length $\gamma^2\lambda\!\!\!^{-}$. One can still use the same reasoning considered for the bend to define a region of the trajectory where it does not make sense to distinguish between different points. In the case of a straight section of length L connecting A and B, $dt/dt' = 1/(2\gamma^2)$. It follows that the apparent distance AB is equal to $L/(2\gamma^2)$. Since it does not make sense to distinguish between points within the apparent electron trajectory such that $L/(2\gamma^2) \lesssim \lambda\!\!\!^{-}$, one obtains a critical length of interest $\sim \gamma^2\lambda\!\!\!^{-}$. This hints to the fact that for values $\phi \simeq 1$ radiation has reached the best collimation angle.

Note that for ultrarelativistic systems in general, the formation length is always much longer than the radiation wavelength. This is related with a large compression factor dt/dt'. For comparison, in the case of non-relativistic motion the compression factor $dt/dt' \simeq 1$, and the formation length is simply of order of the radiation wavelength. The counterintuitive result follows, that for ultrarelativistic systems one cannot localize sources of radiation within a macroscopic part of the trajectory.

3 Paraxial approximation

In the next two Sections we present a complete theory of ER. All electrodynamical theories are based on the presence of small or large parameters.

In general, the theory of Synchrotron Radiation (SR) is based on the exploitation, for ultra-relativistic particles, of the small parameter γ^{-2}. By this, Maxwell's equations are reduced to much simpler equations with the help of paraxial approximation. ER theory constitutes a particular case of SR

theory, based on the extra small-parameter δ.

Here and everywhere else in this paper we will make consistent use of Gaussian units.

In this Section we deal with the paraxial approximation of Maxwell's equations. We will treat both near and far zone cases, with special attention to the applicability region of equations describing ER in different regions of the parameter space.

Whatever the method used to present results, one needs to solve Maxwell's equations in unbounded space. We introduce a cartesian coordinate system, where a point in space is identified by a longitudinal coordinate z and transverse position $\vec{r}$. Accounting for electromagnetic sources, i.e. in a region of space where current and charge densities are present, the following equation for the field in the space-frequency domain holds in all generality:

$$c^2\nabla^2\vec{\tilde{E}} + \omega^2\vec{\tilde{E}} = 4\pi c^2\vec{\nabla}\bar{\rho} - 4\pi i\omega\vec{\tilde{j}}\,, \tag{2}$$

where $\bar{\rho}(z,\vec{r},\omega)$ and $\vec{\tilde{j}}(z,\vec{r},\omega)$ are the Fourier transforms [1] of the charge density $\rho(z,\vec{r},t)$ and of the current density $\vec{j}(z,\vec{r},t)$. Eq. (2) is the well-known Helmholtz equation. Here $\vec{\tilde{E}}$ indicates the Fourier transform of the electric field in the space-time domain.

A system of electromagnetic sources in the space-time can be conveniently described by $\rho(z,\vec{r},t)$ and $\vec{j}(z,\vec{r},t)$. Considering a single electron and using the Dirac delta distribution, we can write

$$\rho\left(z,\vec{r},t\right) = -e\delta\left(\vec{r}-\vec{r}_0(t)\right)\delta(z-z_0(t)) = -\frac{e}{v_z(z)}\delta\left(\vec{r}-\vec{r}_0(z)\right)\delta\left(\frac{s(z)}{v}-t\right) \tag{3}$$

$$\vec{j}(z,\vec{r},t) = \vec{v}(t)\rho\left(z,\vec{r},t\right)\ , \tag{4}$$

where $(z_0(t),\vec{r}_0(t))$ and $\vec{v}(t)$ are, respectively, position and velocity of the particle at a given time t in a fixed reference frame, v_z is the longitudinal velocity of the electron , and $(-e)$ is the electron charge. Additionally, we

[1] We explicitly write the definitions of the Fourier transform and inverse transform of a function $f(t)$ in agreement with the notations used in this paper. The Fourier transform and inverse transform pair reads:

$$\tilde{f}(\omega) = \int \mathrm{d}t\ f(t)\exp\left[i\omega t\right]\ ;\ \ f(t) = \frac{1}{2\pi}\int \mathrm{d}\omega\ \tilde{f}(\omega)\exp\left[-i\omega t\right].$$

defined the curvilinear abscissa $s(z) = vt(z)$, where $v = \left|\vec{v}(t(z))\right|$ is a constant. In the space-frequency domain the electromagnetic sources transform to:

$$\bar{\rho}(\vec{r}, z, \omega) = -\frac{e}{v_z(z)}\delta\left(\vec{r} - \vec{r}_0(z)\right)\exp\left[\frac{i\omega s(z)}{v}\right] \tag{5}$$

and

$$\vec{\bar{j}}(\vec{r}, z, \omega) = \vec{v}(z)\bar{\rho}(\vec{r}, z, \omega) \tag{6}$$

Since we will only be interested in the transverse components of the field, from now on we will consider the transverse field envelope $\vec{\tilde{E}}$, a 2D vector defined in the space-frequency domain as $\vec{\tilde{E}} = \vec{\bar{E}}_\perp \exp[-i\omega z/c]$, the symbol "$\perp$" indicating projection on the transverse plane. By substitution in Helmholtz equation we obtain

$$\left(\nabla^2 + \frac{2i\omega}{c}\frac{\partial}{\partial z}\right)\vec{\tilde{E}} = \frac{4\pi e}{v_z(z)}\exp\left[i\omega\left(\frac{s(z)}{v} - \frac{z}{c}\right)\right]\left[\frac{i\omega}{c^2}\vec{v}_\perp(z) - \vec{\nabla}_\perp\right]\delta\left(\vec{r} - \vec{r}_0(z)\right), \tag{7}$$

where, according to our notation, $\vec{\nabla}_\perp$ indicates a gradient with respect to transverse coordinates only, and $\vec{v}_\perp$ is the transverse velocity of the electron. Eq. (7) is still fully general and may be solved in any fixed reference system (x, y, z) of choice with the help of an appropriate Green's function.

When the longitudinal velocity of the electron, v_z, is close to the speed of light c, one has $\gamma_z^2 \gg 1$, where $\gamma_z^{-2} = 1 - v_z^2/c^2$. The Fourier components of the source are then almost synchronized with the electromagnetic wave travelling at the speed of light. Note that this synchronization is the reason for the time compression factor described in Section 2.3. In this case, the phase $\omega(s(z)/v - z/c)$ is a slow function of z compared to the wavelength. For example, in the particular case of motion on a straight section, one has $s(z) = z/v_z$, so that $\omega(s(z)/v - z/c) = \omega z/(2\gamma_z^2 c)$, and if $\gamma_z^2 \gg 1$ such phase grows slowly in z with respect to the wavelength. For a more generic motion, one similarly obtains:

$$\omega\left(\frac{s(z_2) - s(z_1)}{v} - \frac{z_2 - z_1}{c}\right) = \int_{z_1}^{z_2} d\bar{z}\frac{\omega}{2\gamma_z^2(\bar{z})c}\,, \tag{8}$$

Mathematically, the phase in Eq. (8) enters in the Green's function solution of Eq. (7) as a factor in the integrand. As we integrate along z, the factor $\omega(s(z)/v - z/c)$ leads to an oscillatory behavior of the integrand over a certain

integration range in z. Such range can be identified with the value of $z_2 - z_1$ for which the right hand side of Eq. (8) is of order unity, and it is naturally defined as the radiation formation length L_f of the system at frequency ω. Of course there exist some freedom in the choice of such definition: "order of unity" is not a precise number, and reflects the fact that there is no abrupt threshold between "oscillatory" and "non-oscillatory" behavior of the integrand in the solution of Eq. (7). It is easy to see by inspection of Eq. (8) that if v_z is sensibly smaller than c, but still of order c, i.e. $v_z \sim c$ but $1/\gamma_z^2 \sim 1$, then $L_f \sim \lambda\!\!\!^{-}$. On the contrary, when v_z is very close to c, i.e. $1/\gamma_z^2 \ll 1$, the right hand side of Eq. (8) is of order unity for $L_f = z_2 - z_1 \gg \lambda\!\!\!^{-}$. When the radiation formation length is much longer than $\lambda\!\!\!^{-}$, $\vec{\vec{E}}$ does not vary much along z on the scale of $\lambda\!\!\!^{-}$, that is $\mid \partial_z \widetilde{E}_{x,y} \mid \ll \omega/c \mid \widetilde{E}_{x,y} \mid$. Therefore, the second order derivative with respect to z in the ∇^2 operator on the left hand side of Eq. (7) is negligible with respect to the first order derivative, and Eq. (7) can be simplified to

$$\left(\nabla_\perp{}^2 + \frac{2i\omega}{c}\frac{\partial}{\partial z}\right)\vec{\vec{E}} = \frac{4\pi e}{c}\exp\left[i\omega\left(\frac{s(z)}{v} - \frac{z}{c}\right)\right]\left[\frac{i\omega}{c^2}\vec{v}_\perp(z) - \vec{\nabla}_\perp\right]\delta\left(\vec{r} - \vec{r}_0(z)\right) \ , \tag{9}$$

where, as said before, we consider transverse components of $\vec{\vec{E}}$, and we substituted $v_z(z)$ with c, based on the fact that $1/\gamma_z^2 \ll 1$. Eq. (9) is Maxwell's equation in paraxial approximation. Eq. (7), which is an elliptic partial differential equation, has thus been transformed into Eq. (9), that is of parabolic type. Note that the applicability of the paraxial approximation depends on the ultra-relativistic assumption $\gamma^2 \gg 1$ but not on the choice of the z axis. If, for a certain choice of the longitudinal z direction, part of the trajectory is such that $\gamma_z^2 \sim 1$, the formation length is very short ($L_f \sim \lambda\!\!\!^{-}$), and the radiated field is practically zero. As a result, Eq. (9) can always be applied, i.e. the paraxial approximation can always be applied, whenever $\gamma^2 \gg 1$.

Complementarily, it should also be remarked here that the status of the paraxial equation Eq. (9) in Synchrotron Radiation theory is different from that of the paraxial equation in Physical Optics. In the latter case, the paraxial approximation is satisfied only by small observation angles. For example, one may think of a setup where a thermal source is studied by an observer positioned at a long distance from the source and behind a limiting aperture. Only if a small-angle acceptance is considered the paraxial approximation can be applied. On the contrary, due to the ultra-relativistic nature of the emitting electrons, contributions to the SR field from parts of the trajectory with formation length $L_f \gg \lambda\!\!\!^{-}$ (the only non-negligible) are highly collimated. As a result, the paraxial equation can be applied at any angle of interest, because it practically returns zero field at angles where it should

not be applied.

Finally, since the characteristic scale of variation of $\vec{\vec{E}}$ is much larger than λ, the paraxial approximation is valid up to distances of the observer from the electromagnetic sources of order λ.

The Green's function for Eq. (9), namely the solution corresponding to the unit point source can explicitly be written in an unbounded region as

$$G(\vec{r}-\vec{r'},z-z') = -\frac{1}{4\pi|z-z'|}\exp\left[i\omega\frac{|\vec{r}-\vec{r'}|^2}{2c|z-z'|}\right], \tag{10}$$

Note that when $z-z' < 0$ the paraxial approximation does not hold, and the paraxial wave equation Eq. (9) should be substituted, in the space-frequency domain, by the more general Helmholtz equation. However, the radiation formation length for $z-z' < 0$ is very short with respect to the case $z-z' > 0$, i.e. there is effectively no radiation for observer positions $z - z' < 0$. As a result, in this paper we will consider only $z - z' > 0$. The reason why $|z - z'|$ is present in Eq. (10) (while $z - z' > 0$ always) is that, mathematically, the Green's function G is actually related to the *operator* on the left hand side of Eq. (9), and not to the whole equation. For example, when dealing with wavefront propagation, one must consider the homogeneous version of Eq. (9), and the same Green's function in Eq. (10) can be used, as we will see, to propagate the electric field. In this case, propagation can be performed in the backward direction as well, i.e. for $z - z' < 0$.

Note that Eq. (10) automatically include information about the boundary condition for the field. In the present case, since we are dealing with unbounded space, the field vanishes at large distance from the sources. Due to this fact, the Green's function in Eq. (10) is a scalar function, while in general it admits tensorial values. Using the definition of Green's function, and carrying out integration over transverse coordinates we obtain

$$\begin{aligned}\vec{\vec{E}} = \frac{4\pi e}{c}\int_{-\infty}^{z} dz' \left\{\frac{i\omega}{c^2}\vec{v}_\perp(z')G\left(\vec{r}-\vec{r}_0(z'),z-z'\right) + \left[\vec{\nabla}'_\perp G\left(\vec{r}-\vec{r'},z-z'\right)\right]_{\vec{r'}=\vec{r}_0(z')}\right\} \\ \times\exp\left[i\omega\left(\frac{s(z)}{v}-\frac{z}{c}\right)\right],\end{aligned} \tag{11}$$

where$\vec{\nabla}'_\perp$ indicates derivative with respect to $\vec{r'}$. Explicit substitution of Eq. (10) yields the following result

$$\vec{\vec{E}}(z,\vec{r}) = -\frac{i\omega e}{c^2}\int_{-\infty}^{z} dz' \frac{1}{z-z'}\left[\frac{\vec{v}_\perp(z')}{c} - \frac{\vec{r}-\vec{r}_0(z')}{z-z'}\right] \times \exp\left\{i\omega\left[\frac{|\,\vec{r}-\vec{r}'\,|^2}{2c(z-z')} + \int_0^{z'} d\bar{z}\frac{1}{2\gamma_z^2(\bar{z})c}\right]\right\}, \quad (12)$$

where we the choice of integration limits in $d\bar{z}$ indicate that the electron arrives at position $z = 0$ at time $t_a = 0$. Eq. (12) is valid at any observation position z such that the paraxial approximation is valid, i.e. up to distances between the observer and the electromagnetic sources comparable with the radiation wavelength. One may recognize two terms in Eq. (12). The first in $\vec{v}_\perp(z')$ can be traced back to the current term on the right hand side of Eq. (7), while the second, in $\vec{r} - \vec{r}_0(z')$, corresponds to the gradient term on the right hand side of Eq. (7).

Eq. (12) is used as starting point for numerical codes like SRW. The only approximation used is the paraxial approximation. This rules out the possibility of using SRW to study the region of applicability of the paraxial approximation. However, once the paraxial approximation is granted for valid, SRW, or Eq. (12), can be used to investigate the applicability of ER theory, which is built within the constraints of the paraxial approximation. Note that the evaluation of the field begins with the knowledge of the trajectory followed by the electron, which is completely generic. In other words, one needs to know the electromagnetic sources to evaluate the field at any position z down the beamline.

Alternatively, the knowledge of the far-zone field distribution, i.e. a limit of Eq. (12), allows one to specify an algorithm to reconstruct the field in the near zone up to distances of the observer from the sources much larger than $\lambda\!\!\!^{-}$. An important characteristic of this algorithm is that it works within the region of applicability of the paraxial approximation, $\gamma^2 \gg 1$ only. Such algorithm was developed in [15] to deal with SR problems in full generality, and will be used in this paper to develop our ER theory. It follows three major steps.

I. The first step is the characterization of ER emission in the far zone. From Eq. (12) follows directly:

$$\vec{\vec{E}}(z,\vec{\theta}) = -\frac{i\omega e}{c^2 z}\int_{-\infty}^{z} dz' \left(\frac{\vec{v}_\perp(z')}{c} - \vec{\theta}\right)$$

$$\times \exp\left[i\omega \int_0^{z'} \frac{d\bar{z}}{2c\gamma_z^2(\bar{z})} + \frac{i\omega}{2c}\left(z\,\theta^2 - 2\vec{\theta}\cdot\vec{r}_0(z') + z'\theta^2 \right) \right], \tag{13}$$

where $\vec{\theta} = \vec{r}/z$ defines the observation direction, and $\theta \equiv |\vec{\theta}|$. Note that the concept of formation length is strictly related to the concept of observation angle of interest. In fact, given a certain formation length L_f, and substituting it into the phase in $z'\theta^2$ in Eq. (13), one sees that the integrand starts to be highly oscillatory for angles $\theta \simeq \sqrt{\lambda/L_f}$. Eq. (13) is taken as the starting point for our algorithm.

II. The second step consists in interpreting the far-zone field in Eq. (13) as a laser-like beam, generated by one or more virtual sources. These sources are not present in reality, because they are located at positions inside the magnetic setup, but they produce the same field as that of the real system. Hence the denomination "virtual". A virtual source is similar, in many aspects, to the waist of a laser beam and, in our case, exhibits a plane wavefront. It is then completely specified, for any given polarization component, by a real-valued amplitude distribution of the field, located at a fixed longitudinal position.

Suppose we know the field at a given plane at z, and we want to calculate the field at another plane at z_s. In paraxial approximation and in free space, the homogeneous version of Eq. (9) holds for the complex envelope $\vec{\vec{E}}$ of the Fourier transform of the electric field along a fixed polarization component, that is $[{\nabla_\perp}^2 + (2i\omega/c)\partial_z]\vec{\vec{E}} = 0$. One has to solve this equation with a given initial condition at z, which defines a Cauchy problem. We obtain

$$\vec{\vec{E}}(z_s, \vec{r}) = -\frac{2i\omega}{c} \int d\vec{r'}\, \vec{\vec{E}}(z, \vec{r'}) G\left(\vec{r} - \vec{r'}, z_s - z \right), \tag{14}$$

where the integral is performed over the transverse plane and the Green's function G in unbounded space is given in Eq. (10). Similarly as before, it is important to remark that since $\vec{\vec{E}}$ is a slowly-varying function with respect to the wavelength, one cannot resolve the evolution of the field on a longitudinal scale of order of the wavelength within the accuracy of the paraxial approximation. In order to do so, the paraxial equation should be replaced by the more general Helmholtz equation. Let us now consider the limit $z \longrightarrow \infty$, with finite ratio $\vec{r'}/z$. In this case, the exponential function in Eq. (14) can be expanded giving

$$\vec{\vec{E}}(z_s,\vec{r}) = \frac{i\omega}{2\pi c z}\int d\vec{r'}\,\vec{\vec{E}}(z,\vec{r'})\exp\left[-\frac{i\omega}{2cz}\left(r^2 - 2\vec{r}\cdot\vec{r'} + \frac{z_s r^2}{z}\right)\right]. \tag{15}$$

Letting $\vec{\theta} = \vec{r'}/z$ we have

$$\vec{\vec{E}}\left(z_s,\vec{\theta}\right) = \frac{i\omega z}{2\pi c}\int d\vec{\theta}\exp\left[-\frac{i\omega\theta^2}{2c}(z+z_s)\right]\vec{\vec{E}}\left(z,\vec{\theta}\right)\exp\left[\frac{i\omega}{c}\vec{r}\cdot\vec{\theta}\right], \tag{16}$$

where the transverse vector $\vec{r}$ defines a transverse position on the virtual source plane at $z = z_s$. Eq. (16) allows to calculate the field at the virtual source once the field in the far zone is known. The specification of the virtual source amounts to the specification of an initial condition for the electric field, that is then propagated at any distance. From this viewpoint, identification of the position $z = z_s$ with the virtual source position is possible independently of the choice of z_s. In other words, like in laser physics, the SR field can be propagated starting from any point z_s. However, there are choices that are more convenient than others, exactly like in laser physics the waist plane is privileged with respect to others. The most convenient choice of z_s is the one that allows maximal simplification of the phase contained in the far-zone field $\widetilde{E}(\vec{\theta})$ with the quadratic phase factor in θ^2 in Eq. (16). In practical situations of interest it is possible to choose z_s in such a way that the field at the virtual source exhibits a plane wavefront, exactly as for the waist of a laser beam. Finally, in some cases, it is convenient to consider the far zone field $\widetilde{E}(\vec{\theta})$ as a superposition of different contributions. In this way, more than one virtual source can be identified and treated independently, provided that different contributions are finally summed together.

III. The third, and final step, consists in the propagation of the field from the virtual sources in paraxial approximation. Each source $\vec{\vec{E}}(z_s,\vec{r})$ generates the field

$$\vec{\vec{E}}(z,\vec{r}) = \frac{i\omega}{2\pi c(z-z_s)}\int d\vec{r'}\,\vec{\vec{E}}(z_s,\vec{r'})\exp\left[\frac{i\omega\left|\vec{r}-\vec{r'}\right|^2}{2c(z-z_s)}\right], \tag{17}$$

as follows directly from Eq. (14).

Here it should be stressed that the inverse field problem, which relies on far-field data only, cannot be solved without application of the paraxial approximation.

If the paraxial approximation were not applicable, we should have solved the homogeneous version of Eq. (2). Boundary conditions would have been

constituted by the knowledge of the field on a open surface (for example, a transverse plane) and additionally, by Rayleigh-Sommerfeld radiation condition at infinity, separately for all polarization components of the field. However, this would not have been enough to reconstruct the field at any position in space. In order to do so, we would have had to specify the sources. In fact, the boundary conditions specified above allow one to solve the direct transmission problem, but not the inverse one.

Since, however, the paraxial approximation is applicable, the inverse field problem turns out to have unique and stable solution. A conservative estimate of the accuracy of the paraxial approximation is related to the distance d between the point where we want to know the field and the electron trajectory in the space-frequency domain [15]. When $d \gtrsim L_f$ this accuracy can be estimated to be of order $\lambda\!\!\!^{-}/L_f$. It quickly decreases as $L_f \gg d \gg \lambda\!\!\!^{-}$ remaining, *at least*, of order of $\lambda\!\!\!^{-}/d$.

The fact that we can reconstruct the near-zone field starting from the knowledge of the far-zone field and from the propagation equation looks paradoxical. In fact, in the far zone, all information about the velocity field in the Lienard-Wiechert expressions for the field is lost. It is interesting to note, for example, what is reported in [28] concerning the velocity term: "In the case of infrared synchrotron radiation, and THz radiation in particular, this term is not small and must be included in all calculations". Here we apparently seem to have lost track of every information about the velocity term. As shown in [15], the paradox is solved by the fact that, although in the far-zone limit of Eq. (12) includes information about the Fourier Transform of the acceleration term of the Lienard-Wiechert fields only, information about the velocity term is included in the field propagation equation through the Green's function Eq. (10), which solves Maxwell's equations as the Lienard-Wiechert expressions do.

4 Sharp-edge approximation

Let us consider the system depicted in Fig. 1(a). In this case of study the trajectory and, therefore, the space integration in Eq. (13) can be split in three parts: the two bends, which will be indicated with b_1 and b_2, and the straight section AB. One may write

$$\vec{\vec{E}}(z,\vec{r}) = \vec{\vec{E}}_{b1}(z,\vec{r}) + \vec{\vec{E}}_{AB}(z,\vec{r}) + \vec{\vec{E}}_{b2}(z,\vec{r}) \,, \tag{18}$$

with obvious meaning of notation. We will denote the length of the segment AB with L. This means that points A and B are located at longitudinal

coordinates $z_A = -L/2$ and $z_B = L/2$.

Recalling the geometry in Fig. 1(a) we have $\gamma_z(z) = \gamma$ for $z_A < z' < z_B$. With the help of Eq. (13) we write the contribution from the straight line AB

$$\vec{\tilde{E}}_{AB} = \frac{i\omega e}{c^2 z} \int_{-L/2}^{L/2} dz' \vec{\theta} \exp\left\{\frac{i\omega}{c}\left[\frac{\theta^2 z}{2} + \frac{z'}{2}\left(\frac{1}{\gamma^2} + \theta^2\right)\right]\right\}, \tag{19}$$

where we assumed that $\vec{r}_0(z') = 0$, i.e. that the particle has zero offset and deflection. From Eq. (19) one obtains:

$$\vec{\tilde{E}}_{AB} = \frac{i\omega e L}{c^2 z} \exp\left[\frac{i\omega\theta^2 z}{2c}\right] \vec{\theta}\, \mathrm{sinc}\left[\frac{\omega L}{4c}\left(\theta^2 + \frac{1}{\gamma^2}\right)\right]. \tag{20}$$

Note that Eq. (20) describes a spherical wave with the center in the middle of the straight section. Moreover, it explicitly depends on L.

In the previous Section we defined the formation length as the length needed for the phase of the electric field seen by an observer on the z axis to overtake the phase of the sources of a radiant. It follows from this definition, and from the phase in Eq. (19) that the formation length L_f for the straight section AB can be written as $L_f \sim \min[\gamma^2 \lambda\!\!\!^{-}, L]$. Then, either $L_f \sim \gamma^2 \lambda\!\!\!^{-}$ or $L_f \sim L$. In both cases, with the help of the phase in the integrand in Eq. (19) we can formulate on a purely mathematical basis an upper limit to the value of the observation angle of interest for the straight line, $\theta_{x,y}^2 \lesssim \lambda\!\!\!^{-}/L_f$. Moreover, if $L_f \sim \gamma^2 \lambda\!\!\!^{-}$, the maximal angle of interest is independent of the frequency and equal to $1/\gamma$, in agreement with what has been said before.

According to the superposition principle, one should sum the contribution due to the straight section to that from the bends. However, as discussed in Section 2, when $\delta \ll 1$ one can ignore the presence of the bending magnets with good accuracy. Note that a direct confirmation of this fact can be given by analyzing explicitly the field from the half bends, e.g. $\vec{\tilde{E}}_{b2}$. An expression for the quantity $\vec{\tilde{E}}_{b2}$ can be found from first principles, applying Eq. (13) to the case of a half bend.

In the framework of the paraxial approximation we obtain for $z > L/2$:

$$s(z) \simeq z + \frac{(z - L/2)^3}{6R^2} \quad , \quad \vec{r}(s) = -R\left[1 - \cos\left(\frac{s - L/2}{R}\right)\right]\vec{e}_x \,, \tag{21}$$

$\vec{e}_x$ (or $\vec{e}_y$) being a unit vector along the x (or y) direction. Substitution in Eq.

(13) and use of Eq. (8) gives [2]:

$$\vec{\tilde{E}}_{b2}(z,\vec{\theta}) = \frac{i\omega e}{c^2 z}\exp\left[i\Phi_s\right]\exp\left[i\Phi_0\right]\int\limits_{R\theta_x}^{\infty} dz'\left(\frac{z'}{R}\vec{e}_x + \theta_y\vec{e}_y\right)$$
$$\times\exp\left\{\frac{i\omega}{c}\left[\frac{z'}{2\gamma^2}\left(1+\gamma^2\theta_y^2\right)+\frac{z'^3}{6R^2}\right]\right\}, \tag{22}$$

where

$$\Phi_s = \frac{\omega z(\theta_x^2+\theta_y^2)}{2c} \quad \text{and}$$
$$\Phi_0 = -\frac{\omega R\theta_x}{2c}\left(\frac{1}{\gamma^2}+\frac{\theta_x^2}{3}+\theta_y^2\right)+\frac{\omega L}{4c}\left(\frac{1}{\gamma^2}+\theta_x^2+\theta_y^2\right). \tag{23}$$

Analysis of the phase term in z'^3 Eq. (22) shows that the integrand starts to exhibit oscillatory behavior within distances of order of $L_{fb} = \sqrt[3]{R^2\lambda\!\!\!^{-}}$, that is the radiation formation length for the bending magnet at $\lambda\!\!\!^{-} \gg R/\gamma^3$. Similarly, we have seen from Eq. (19), and has been also shown with qualitative arguments in Section 2, the formation length for the straight section amounts to $L_f = \min[L, \gamma^2\lambda\!\!\!^{-}]$. The ratio L_{fb}/L_f is responsible for the relative weight of ER compared to bending magnet field contribution. Note that strictly speaking, when $\phi \gg 1$, L_{fb}/L_f is equal to $\delta\cdot\phi$ (and not to δ). However, $\delta\cdot\phi \ll 1$ always, to insure that $\lambda\!\!\!^{-} \gg \lambda\!\!\!^{-}_c$. As a result, in all generality, it is possible to talk about ER if and only if $\delta \ll 1$ and $\delta\cdot\phi \ll 1$ (or $\sqrt[3]{R^2\lambda\!\!\!^{-}}/L \ll 1$, $\lambda\!\!\!^{-}/\lambda\!\!\!^{-}_c \ll 1$ in terms of dimensional parameters).

When $\delta \gtrsim 1$, one cannot talk about pure ER. One must account for bending magnet contributions as well. Then, expressions presented here for the electric field from the straight section can be seen as partial contributions, to be added to bending magnet contributions calculated elsewhere.

Note that in this paper we first introduced a measure of "how sharp" the edges are through the parameter δ and, with this, we specified the region of applicability for ER theory.

[2] Usually, in textbooks, the z axis is chosen in such a way that $\theta_x = x/z = 0$, i.e. it is not fixed, but depends on the observer position. This can always be done, and simplifies calculations. However, since the wavefront is not spherical, this way of proceeding can hardly help to obtain the phase of the field distribution on a plane perpendicular to a *fixed* z axis. Calculations in our (fixed) coordinate system is more complicated and can be found in e.g. in [29]. After some algebraic manipulation and change of variables we obtain Eq. (22).

It should also be noted that bending magnets at the straight section ends act like switchers, i.e. they switch on and off radiation seen by an observer. Observers see uniform intensity from a bend along the horizontal direction. However, not all parts of the trajectory contribute to the radiation seen by a given observer, because radiation contributions from different parts of the bend is highly collimated, hence the switching function. Since we are not interested in electromagnetic sources responsible for field contributions that are not seen by the observer, we may say that bends switch on and off electromagnetic sources as well.

Finally, it should be remarked that the far-zone asymptotic in Eq. (19) is valid at observation positions $z \gg L$. This is a necessary and sufficient condition for the vector $\vec{n}$ pointing from source to observer, to be considered constant. This result is independent of the formation length. When $L \lesssim \gamma^2 \lambda\!\!\!^{-}$ we can say that an observer is the far zone if and only if it is located many formation lengths away from the origin. This is no more correct when $L \gg \gamma^2 \lambda\!\!\!^{-}$. In this case the observer can be located at a distance $z \gg \gamma^2 \lambda\!\!\!^{-}$, i.e. many formation lengths away from the origin of the reference system, but still at $z \sim L$, i.e. in the near zone. As we see here, the formation length L_f is often, but not always related to the definition of the far (or near) zone. In general, the far (or near) zone is related to the characteristic size of the system, in our case L. In its turn $L_f \lesssim L$, which includes, when $\gamma^2 \lambda\!\!\!^{-} \ll L$, the situation $L_f \ll L$.

Since in the following we will only deal with a contribution of the electric field, i.e. that from the straight section $\vec{\vec{E}}_{AB}$, from now on, for simplicity, we will omit the subscript AB.

The radiation energy density as a function of angles and frequencies ω, i.e. the angular spectral flux, can be written as

$$\frac{dW}{d\omega d\Omega} = \frac{cz^2}{4\pi^2} \left| \vec{\vec{E}} \right|^2 \ , \tag{24}$$

$d\Omega$ being the differential of the solid angle Ω. Substituting Eq. (20) in Eq. (24) it follows that [5]

$$\frac{dW}{d\omega d\Omega} = \frac{e^2 \omega^2 L^2}{4\pi^2 c^3} \theta^2 \, \mathrm{sinc}^2 \left[\frac{L\omega}{4c} \left(\theta^2 + \frac{1}{\gamma^2} \right) \right] . \tag{25}$$

It is now straightforward to introduce the same normalized quantities defined in Section 2: $\vec{\tilde{\theta}} = \sqrt{L/\lambda\!\!\!^{-}} \, \vec{\theta}$, and $\phi = L/(\gamma^2 \lambda\!\!\!^{-})$. We may write the angular spectral flux in normalized units as

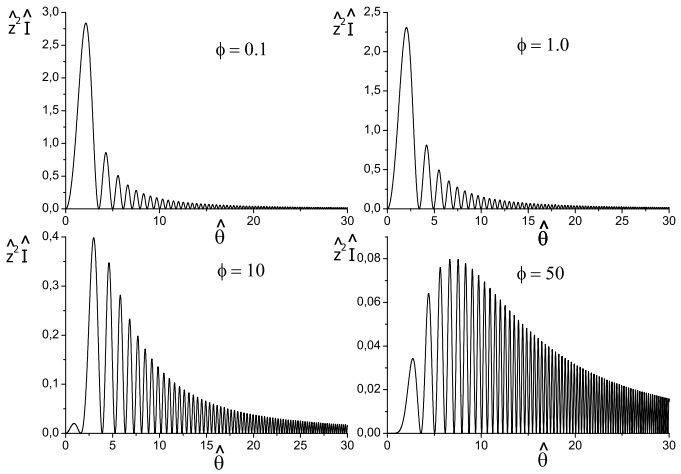

Fig. 6. Normalized angular spectral flux of the radiation from the setup in Fig. 1(a) for different values of ϕ.

$$\hat{I} \equiv \frac{c^3 L}{\omega e^2} \left| \vec{\tilde{E}} \right|^2 \ , \tag{26}$$

so that

$$\hat{z}^2 \hat{I} = \hat{\theta}^2 \, \mathrm{sinc}^2 \left[\frac{1}{4} \left(\hat{\theta}^2 + \phi \right) \right] , \tag{27}$$

where $\hat{z} = z/L$. Eq. (27) is plotted in Fig. 6 for several values of ϕ as a function of the normalized angle $\hat{\theta}$. The natural angular unit is evidently $\sqrt{\lambda/L}$.

The angular spectral flux, once integrated in angles, is divergent, as one can see from $\hat{z}^2\hat{I} \propto 1/\hat{\theta}$. This feature is related with the limit of applicability of the sharp-edge approximation. Note that within the framework of the paraxial approximation alone, the integrated angular spectral flux calculated with Eq. (13) does not have any singularity, whatever the electron trajectory is. The paraxial approximation, as discussed above, is related to the large parameter γ^2. However, our ER theory is related to another parameter, $\delta \ll 1$, which controls the accuracy of the sharp-edge approximation. It is within the framework of the sharp-edge approximation that the integrated flux is logarithmically divergent. Accounting for the presence of the bend would simply cancel this divergence.

We can now justify findings in the previous Section. From Eq. (27) we see that, in the limit for $\phi \ll 1$, the radiation profile is a universal function, and peaks at $\hat{\theta} \sim 2.2$. When, instead, $\phi \gtrsim 1$, radiation is much better collimated peaking at $\hat{\theta} \sim \sqrt{\phi}$ corresponding to $\theta \sim 1/\gamma$.

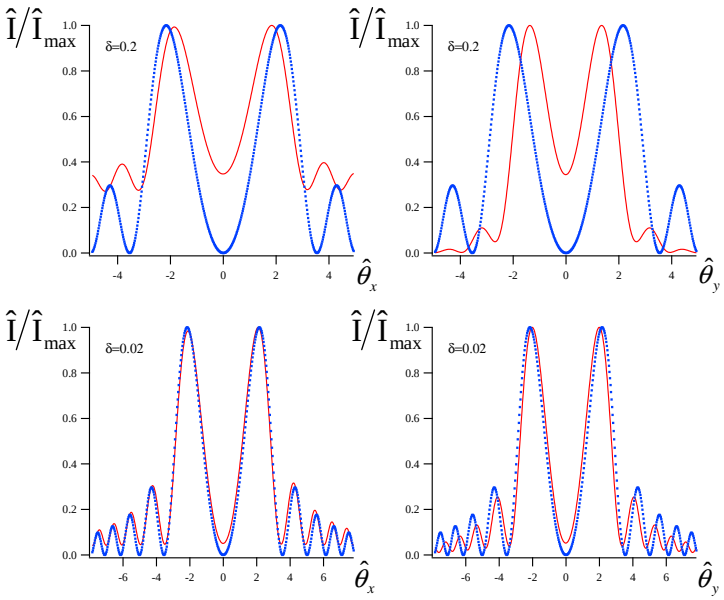

Fig. 7. Angular spectral flux as a function of the normalized angle $\hat{\theta}$ for two different edge length parameters $\delta = 0.2$ and $\delta = 0.02$. Here the straight section length parameter $\phi \simeq 0.01$. Left and right plots are obtained cutting the spectral flux profile at $\hat{\theta}_y = 0$ and $\hat{\theta}_x = 0$ respectively (i.e. electron motion is in xz plane). The dotted curves are calculated with the analytical formula Eq. (27). Solid lines are the results of numerical calculations with computer code SRW.

The behavior of the far-field emission described here is well-known in literature. Nonetheless, the accuracy of the asymptotic expression for $\delta \ll 1$, Eq. (27), has never been discussed: the parameter δ has been introduced here for the first time. Numerical calculations were never used before to scan the parameter space in δ and to provide an universal algorithm for estimating the accuracy of the ER theory. We can study such accuracy now by comparing asymptotical results with SRW outcomes at different values of δ. This comparison is illustrated in Fig. 7. It can be seen that edge radiation approximation provides good accuracy for $\delta \lesssim 0.01$.

For completeness, and within the limiting case for $\delta \ll 1$, it is interesting to study the accuracy of the asymptotic expression for $\phi \ll 1$ of Eq. (27). In this case one does not need comparisons with SRW results, because the asymptotic limit of Eq. (27) is simply

$$\hat{z}^2 \hat{I} = \hat{\theta}^2 \, \mathrm{sinc}^2 \left[\frac{\hat{\theta}^2}{4} \right] . \tag{28}$$

Results are shown in Fig. 8. It can be seen that the asymptotic expression Eq. (28) provides good accuracy for $\phi \lesssim 0.1$.

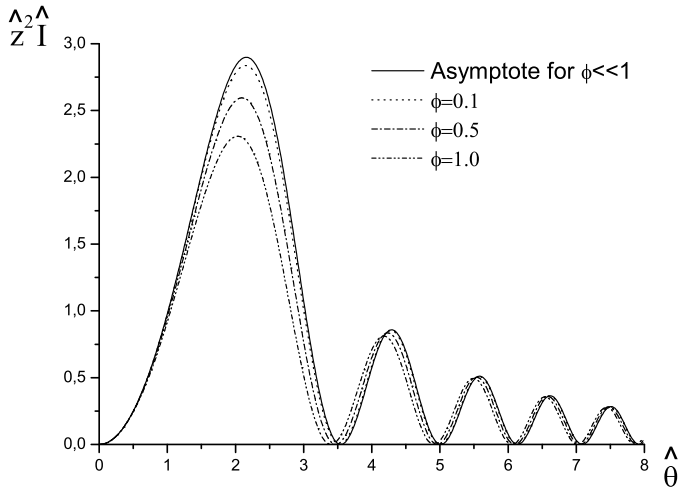

Fig. 8. Angular spectral flux as a function of the normalized angle $\hat{\theta}$ for different straight-section length parameters ϕ calculated after Eq. (27) and comparison with the asymptotic limit for $\phi \ll 1$ in Eq. (28).

From now on, we will only consider the asymptote for sharp-edges $\delta \ll 1$ in the far-zone. This is the starting point for further investigations of near-zone ER, based on the use of virtual source techniques.

5 Near field Edge Radiation theory

5.1 Edge Radiation as a field from a single virtual source

Eq. (16) and Eq. (20) allow one to characterize the virtual source through

$$\vec{\vec{E}}(0,\vec{r}) = -\frac{\omega^2 eL}{2\pi c^3}\int d\vec{\theta}\,\vec{\theta}\,\mathrm{sinc}\left[\frac{\omega L}{4c}\left(\theta^2+\frac{1}{\gamma^2}\right)\right]\exp\left[\frac{i\omega}{c}\vec{r}\cdot\vec{\theta}\right]. \qquad (29)$$

Eq. (29) is valid in any range of parameters, i.e. for any choice of ϕ. However, the Fourier transform in Eq. (29) is difficult to calculate analytically in full generality. Simple analytical results can be found in the asymptotic case for $\phi \ll 1$, i.e. for $L/(\gamma^2\lambda\!\!\!^{-}) \ll 1$. In this limit, the right hand side of Eq. (29) can be calculated with the help of polar coordinates. An analytic expression for the field amplitude at the virtual source can then be found and reads:

$$\vec{\vec{E}}(0,\vec{r}) = -i\frac{4\omega e}{c^2 L}\,\vec{r}\,\mathrm{sinc}\left(\frac{\omega r^2}{cL}\right), \tag{30}$$

where $r^2 = \left|\vec{r}\right|^2$ as usual. It is useful to remark, for future use, that similarly to the far-field emission Eq. (20), also the field in Eq. (30) explicitly depend on L.

It is interesting to comment on the meaning of the phase in Eq. (30), i.e. on the factor $-i$ in front of the right hand side. Such phase is linked with the (arbitrary) choice of phase of the harmonic of the charge density at $z = 0$. In particular, such phase was chosen to be zero at $z = 0$. Propagating Eq. (30) to the far-zone, one obtains Eq. (20). In other words, the plane wavefront transforms into a spherical wavefront centered at $z = 0$. Note that there is an imaginary unit i in front of Eq. (20), meaning that an extra minus sign, i.e. a phase shift of π, results from the propagation of Eq. (30). This extra phase shift of π represent the analogous of the Guoy phase shift in laser physics, and is in agreement with our interpretation of the virtual source in Eq. (30) as the waist of a laser-like beam. Note that, while for azimuthal-symmetric beams the Guoy phase shift is known to be $\pi/2$, this result is not valid in our case where the cartesian components of the field depend on the azimuthal angle.

We define the normalized transverse position $\vec{\hat{r}} = \vec{r}/\sqrt{\lambda L}$. Moreover, since the source is positioned at $z = 0$, we indicate the normalized spectral flux at the virtual source as $\hat{I}_s$, defined similarly as $\hat{I}$ in Eq. (26). It follows that

$$\hat{I}_s(\hat{r}) = 16\,\hat{r}^2\mathrm{sinc}^2\left(\hat{r}^2\right). \tag{31}$$

The profile in Eq. (31) can be detected (aside for scaling factors) by imaging the virtual plane with an ideal lens, and is plotted in Fig. 9.

Note that Eq. (30) describes a virtual source characterized by a plane wavefront. Application of the propagation formula, Eq. (14), to Eq. (30) allows one to reconstruct the field both in the near and in the far region. We obtain the following result:

$$\begin{aligned}\vec{\vec{E}}(z,\vec{\theta}) = &-\frac{2e}{zc}\frac{\vec{\theta}}{\theta^2}\exp\left[\frac{i\omega z\theta^2}{2c}\right]\\ &\times\left[\exp\left(-\frac{i\omega z\theta^2}{2c(1+2z/L)}\right)-\exp\left(\frac{i\omega z\theta^2}{2c(-1+2z/L)}\right)\right],\end{aligned} \tag{32}$$

where we defined $\vec{\theta} = \vec{r}/z$, *independently* of the value of z. This definition makes sense whenever $z \neq 0$, and yields usual angular distributions in the

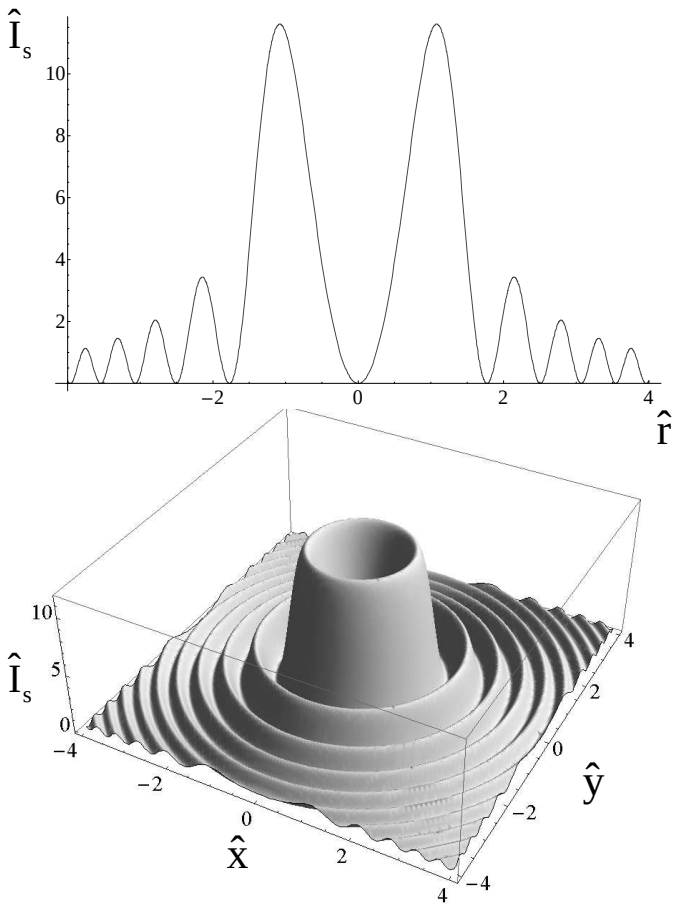

Fig. 9. Normalized spectral flux at the virtual source, $\hat{I}_s$, as a function of $\hat{r}$ (upper plot) and 3D view as a function of $\hat{x}$ and $\hat{y}$.

far zone, for $z \gg L$. Eq. (32) solves the field propagation problem for both the near and the far field in the limit for $\phi \ll 1$.

Eq. (32) is singular at $\vec{r} = 0$ (i.e. $\vec{\theta} = 0$) and $z = L/2$. Within our sharp-edge approximation, this singularity is mathematically related to the divergence of the integrated spectral flux in the far zone, which has been discussed above. If one goes beyond the applicability region of the sharp-edge approximation by specifying the nature of edges and calculating the field within the framework of the paraxial approximation alone (i.e. with Eq. (13)), one sees that the integrated angular spectral flux is not divergent anymore, and that the field reconstructed at the point $\vec{r} = 0$, $z = L/2$ using this far-field data has no singularity at all.

Note that in the limit for $z \gg L$ Eq. (32) transforms to

$$\vec{\vec{E}} = \frac{i\omega eL}{c^2 z} \exp\left[\frac{i\omega\theta^2 z}{2c}\right] \vec{\theta}\, \mathrm{sinc}\left[\frac{\omega L\theta^2}{4c}\right] \tag{33}$$

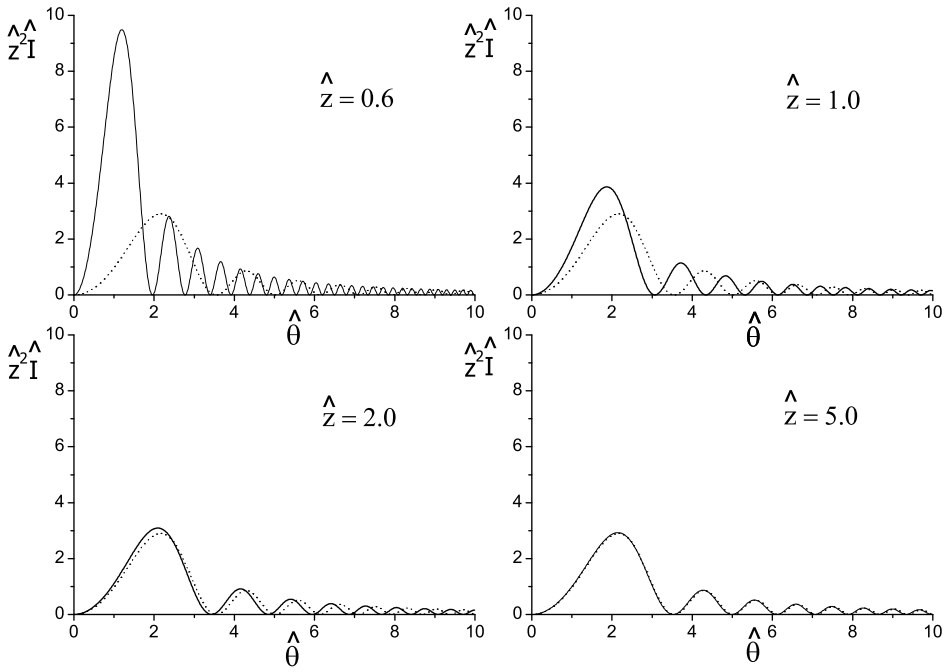

Fig. 10. Evolution of $\hat{z}^2\hat{I}$ for edge radiation in the limit for $\phi \ll 1$. These profiles, calculated with Eq. (34), are shown as a function of angles at different observation distances $\hat{z} = 0.6$, $\hat{z} = 1.0$, $\hat{z} = 2.0$ and $\hat{z} = 5.0$ (solid lines). The dashed line always refers to the far-zone asymptote, Eq. (28).

corresponding to the limit of Eq. (20) for $L \ll \gamma^2 \lambda$, i.e. $\phi \ll 1$.

The normalized angular spectral flux associated with Eq. (32) is given by

$$\hat{z}^2\hat{I}\left(\hat{z},\hat{\theta}\right) = \frac{4}{\hat{\theta}^2}\left|\left[\exp\left(-\frac{i\hat{\theta}^2\hat{z}}{2(1+2\hat{z})}\right) - \exp\left(\frac{i\hat{\theta}^2\hat{z}}{2(-1+2\hat{z})}\right)\right]\right|^2 . \tag{34}$$

This notation is particularly suited to discuss near and far zone regions. Eq. (34) reduces to Eq. (28) when $\hat{z} \gg 1$. To sum up, when $\phi \ll 1$ we have only two regions of interest with respect to $\hat{z}$:

- **Far zone.** In the limit for $\hat{z} \gg 1$ one has the far field case, and Eq. (34) simplifies to Eq. (28).
- **Near zone.** When $\hat{z} \lesssim 1$ instead, one has the near field case, and Eq. (34) must be used.

Of course, it should be stressed that in the case $\hat{z} \lesssim 1$ we still hold the assumption that the sharp-edge approximation of is satisfied. It is interesting to study the evolution of the normalized angular spectral flux for edge

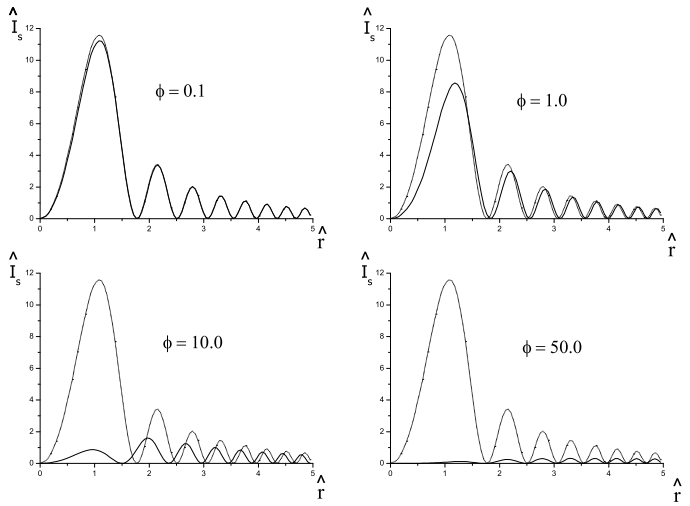

Fig. 11. Normalized spectral flux at the virtual source for the setup in Fig. 1(a). These profiles are shown for $\phi = 0.1$, $\phi = 1.0$, $\phi = 10.0$ and $\phi = 50.0$ (solid lines). Solid curves are calculated with the help of Eq. (35). The dotted lines show comparison with the asymptotic limit for $\phi \ll 1$, shown in Fig. 9 and calculated using Eq. (31).

radiation along the longitudinal axis. This gives an idea of how good the far field approximation ($\hat{z} \gg 1$) is. A comparison between $\hat{z}^2\hat{I}$ at different observation points is plotted in Fig. 10.

The case $\phi \ll 1$ studied until now corresponds to a short straight section, in the sense that $L \ll \gamma^2 \lambda\!\!\!^{-}$. When this condition is not satisfied, we find that the integral on the right hand side of Eq. (29) is difficult to calculate analytically. Thus, the single-source method used here is advantageous in the case $\phi \ll 1$ only. However, one can use numerical techniques to discuss the case for any value of ϕ. With the help of polar coordinates, the right hand side of Eq. (29) can be transformed in a one-dimensional integral, namely

$$\vec{\vec{E}}(0,\vec{r}) = -\frac{4i\omega e}{c^2}\frac{\vec{r}}{r}\int_0^\infty \frac{\theta^2}{\theta^2 + 1/\gamma^2}\sin\left[\frac{\omega L}{4c}\left(\theta^2 + \frac{1}{\gamma^2}\right)\right] J_1\left(\frac{\omega\theta r}{c}\right) d\theta \,, \tag{35}$$

yielding

$$\hat{I}_s(\hat{r}) = \left|\int_0^\infty \frac{4\hat{\theta}^2}{\hat{\theta}^2 + \phi}\sin\left[\frac{\hat{\theta}^2 + \phi}{4}\right] J_1\left(\hat{\theta}\hat{r}\right) d\hat{\theta}\right|^2 . \tag{36}$$

We calculated the spectral flux associated with the virtual source for values $\phi = 0.1$, $\phi = 1$, $\phi = 10$ and $\phi = 50$, the same values chosen for Fig. 6. We

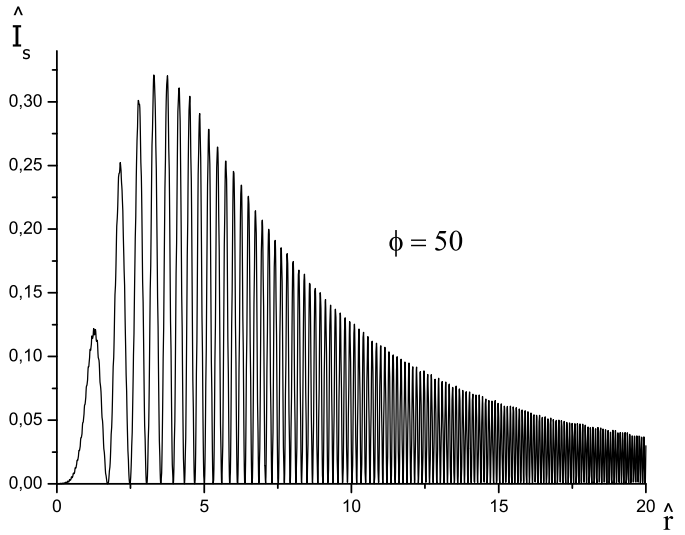

Fig. 12. Normalized spectral flux at the virtual source for the setup in Fig. 1(a) for $\phi = 50$ (enlargement of the bottom right graph in Fig. 11).

plot these distributions in Fig. 11. It is also instructive to make a separate, enlarged plot of the case $\phi = 50$, that is in the asymptotic case for $\phi \gg 1$. This is given in Fig. 12. Fine structures are now evident, and are consistent with the presence of fine structures in Fig. 6 for the far zone.

We managed to specify the field at the virtual source by means of numerical techniques, even in the case $\phi \gg 1$ (see Fig. 12). Once the field at the virtual source is specified for any value of ϕ, Fourier Optics can be used to propagate it. However, we prefer to proceed following another path. There is, in fact, an alternative way to obtain the solution to the field propagation problem valid for any value of ϕ, and capable of giving a better physical insight for large values of ϕ.

5.2 Edge Radiation as a superposition of the field from two virtual sources

Consider the far field in Eq. (20). This can also be written as

$$\vec{\vec{E}}\left(z,\vec{\theta}\right) = \vec{\vec{E}}_1\left(z,\vec{\theta}\right) + \vec{\vec{E}}_2\left(z,\vec{\theta}\right) \quad , \tag{37}$$

where

$$\vec{\vec{E}}_{1,2}\left(z,\vec{\theta}\right) = \mp\frac{2e\vec{\theta}}{cz(\theta^2+1/\gamma^2)}\exp\left[\mp\frac{i\omega L}{4c\gamma^2}\right]\exp\left[\frac{i\omega L\theta^2}{2c}\left(\frac{z}{L}\mp\frac{1}{2}\right)\right]. \tag{38}$$

When $z \gg L$, the two terms $\vec{\vec{E}}_1$ and $\vec{\vec{E}}_2$ represent two spherical waves respectively centered at $z_{s1} = -L/2$ and $z_{s2} = L/2$, that is at the edges between straight section and bends [3]. Analysis of Eq. (38) shows that both contributions to the total field are peaked at an angle of order $1/\gamma$. While the amplitude of the total field explicitly depends on L, the two expressions $\vec{\vec{E}}_1$ and $\vec{\vec{E}}_2$ exhibit dependence on L through phase factors only. This fact will have interesting consequences, as we will discuss later. The two spherical waves represented by $\vec{\vec{E}}_1$ and $\vec{\vec{E}}_2$ may be thought as originating from two separate virtual sources located at the edges between straight section and bends. One may then model the system with the help of two separate virtual sources, and interpret the field at any distance as the superposition of the contributions from two edges. It should be clear that contributions from these edges are linked with an integral of the trajectory followed by the electron. Thus the word "edge" should be considered as a synonym for "virtual source" here.

Let us specify analytically the two virtual sources at the edges of the setup. To this purpose, we take advantage of Eq. (16) with $z_s = z_{s(1,2)}$, separately substituting $\vec{\vec{E}}_1$ and $\vec{\vec{E}}_2$ and using polar coordinates. We find the following expressions for the field at the virtual source positions $z_{s1} = -L/2$ and $z_{s2} = L/2$:

$$\vec{\vec{E}}_{s1,s2}\left(\mp\frac{L}{2},\vec{r}\right) = \pm\frac{2\omega e}{c^2\gamma}\exp\left[\mp\frac{i\omega L}{4\gamma^2 c}\right]\frac{\vec{r}}{r}K_1\left(\frac{\omega r}{c\gamma}\right), \tag{39}$$

where $K_1(\cdot)$ is the modified Bessel function of the first order. Analysis of Eq. (39) shows a typical scale related to the source dimensions of order $\lambda\gamma$ in dimensional units, corresponding to $1/\sqrt{\phi}$ in normalized units. Also, the fact that the field in the far zone, Eq. (20), exhibits dependence on L only

[3] At first glance this statement looks counterintuitive. In order to find where the spherical wave is centered, one needs to know where the phase becomes zero. Now, when $z = L/2$, the phase in θ^2 for $\vec{\vec{E}}_2$ in Eq. (38) is not zero, hinting to the fact that the spherical wave $\vec{\vec{E}}_2$ is not centered at $z = L/2$. This last observation, however, is misleading. In fact, one should account for the fact that the definition $\vec{\theta} = \vec{r}/z$ is not natural for $\vec{\vec{E}}_1$ and $\vec{\vec{E}}_2$. In fact, according to it, $\vec{\theta}$ is measured from the center of the straight section, while it should be measured from $z = -L/2$ for $\vec{\vec{E}}_1$ and from $z = L/2$ for $\vec{\vec{E}}_2$. Also note that Eq. (38) is only valid in the limit $z \gg L$.

through phase factors implies that the field at the virtual sources, Eq. (39), exhibits dependence on L only through phase factors (and viceversa).

Application of the propagation formula Eq. (14) allows to calculate the field at any distance z in free-space. Of course, Eq. (39) can also be used as input to any Fourier code to calculate the field evolution in the presence of whatever optical beamline. However, here we restrict ourselves to the free-space case. In order to simplify the presentation of the electric field we take advantage of polar coordinates and we use the definition $\vec{\hat{E}} \equiv \vec{\tilde{E}} \sqrt{\lambda L}\, c/e$ (so that $\hat{I}$, introduced in Eq. (26), is given by $\hat{I} = |\vec{\hat{E}}|^2$) for the field in normalized units. We obtain:

$$\begin{aligned}
\hat{z}\vec{\hat{E}}\left(\hat{z},\vec{\hat{\theta}}\right) = &\left\{\frac{\vec{\hat{\theta}}}{\hat{\theta}}\frac{2\hat{z}\sqrt{\phi}\exp\left[i\phi/4\right]}{\hat{z}-1/2}\exp\left[\frac{i\hat{\theta}^2\hat{z}^2}{2\left(\hat{z}-1/2\right)}\right]\right. \\
&\left.\times\int_0^\infty d\hat{r}'\hat{r}'K_1\left(\sqrt{\phi}\hat{r}'\right)J_1\left(\frac{\hat{\theta}\hat{r}'\hat{z}}{\hat{z}-1/2}\right)\exp\left[\frac{i\hat{r}'^2}{2\left(\hat{z}-1/2\right)}\right]\right\} \\
&-\left\{\frac{\vec{\hat{\theta}}}{\hat{\theta}}\frac{2\hat{z}\sqrt{\phi}\exp\left[-i\phi/4\right]}{\hat{z}+1/2}\exp\left[\frac{i\hat{\theta}^2\hat{z}^2}{2\left(\hat{z}+1/2\right)}\right]\right. \\
&\left.\times\int_0^\infty d\hat{r}'\hat{r}'K_1\left(\sqrt{\phi}\hat{r}'\right)J_1\left(\frac{\hat{\theta}\hat{r}'\hat{z}}{\hat{z}+1/2}\right)\exp\left[\frac{i\hat{r}'^2}{2\left(\hat{z}+1/2\right)}\right]\right\}\ . \qquad (40)
\end{aligned}$$

In the limit for $\hat{z} \gg 1$, using Eq. (40) and recalling $\int_0^\infty d\hat{r}'\ \hat{r}'K_1(\sqrt{\phi}\hat{r}')J_1(\hat{\theta}\hat{r}') = \hat{\theta}/[\sqrt{\phi}(\hat{\theta}^2+\phi)]$ we obtain back Eq. (27). Similarly, in the limit for $\phi \ll 1$, and using the fact that $K_1(\sqrt{\phi}\hat{r}) \simeq 1/(\hat{r}\sqrt{\phi})$ one recovers Eq. (32). In general, the integrals in Eq. (40) cannot be calculated analytically, but they can be integrated numerically.

5.3 Classification of regions of observation

Qualitatively, we can deal with two limiting cases of the theory, the first for $\phi \ll 1$ and the second for $\phi \gg 1$. As for the case of a single virtual source, there are no constraints, in principle, on the value of ϕ. However, as we will see, the two-source method gives peculiar advantages in the case $\phi \gg 1$, while, has we have seen before, the case $\phi \ll 1$ is better treated in the framework of a single source.

5.3.1 *Case $\phi \ll 1$*

Let us briefly discuss the case $\phi \ll 1$ in the framework of the two-source method. In this case, one obviously obtains back Eq. (32). An alternative derivation has been shown in Section 5.1. As one can see Eq. (32) is independent of ϕ. In Fig. 10 we plotted results for the propagation according to Eq. (34). Radiation profiles are shown as a function of angles $\hat{\theta}$ at different observation distances $\hat{z} = 0.6$, $\hat{z} = 1.0$, $\hat{z} = 2.0$ and $\hat{z} = 5.0$. As discussed before, one can recognize two observation zones of interest: the near and the far zone. As it can be seen from Eq. (32), the total field is given, both in the near and in the far zone, by the interference of the virtual source contributions. The virtual sources themselves are located at the straight section edges. Eq. (40) shows that the transverse dimension of these virtual sources is given by $\gamma\lambda\!\!\!^{-}$ in dimensional units. This is the typical scale in r' after which the integrands in $d\hat{r}'$ in Eq. (40) are suppressed by the function K_1. Thus, the sources at the edges of the straight section have a dimension that is independent of L. In the center of the setup instead, the virtual source has a dimension of order $\sqrt{\lambda\!\!\!^{-} L}$ as it can be seen Eq. (31). When $\phi \ll 1$ the source in the center of the setup is much smaller than those at the edge. This looks paradoxical. The explanation is that the two contributions due to edge sources interfere in the center of the setup. In particular, when $\phi \ll 1$ they nearly compensate, as they have opposite sign. As a result of this interference, the single virtual source in the center of the setup (and its far-zone counterpart) has a dimension dependent on L (in non-normalized units) while for two virtual sources at the edges (and in their far-zone counterpart) the dependence on L is limited to phase factors only. Due to the fact that edges contributions nearly compensate for $\phi \ll 1$ one may say that the single-source picture is particularly natural in the case $\phi \ll 1$.

5.3.2 *Case $\phi \gg 1$*

Let us now discuss the case $\phi \gg 1$. In this situation the two-sources picture becomes more natural. We indicate with $d_{1,2} = z \pm L/2$ the distances of the observer from the edges. From Eq. (19) we know that when $\phi \gg 1$ the formation length is $L_f = \gamma^2\lambda\!\!\!^{-}$, much shorter than the system dimension L. As a result, one can recognize four regions of observation of interest.

In Fig. 13 we plotted, in particular, results for the propagation in case $\phi = 50$. In this case, for arbitrary $\hat{z}$, integrals in Eq. (40) cannot be calculated analytically, but they can be integrated numerically. Radiation profiles are shown as a function of angles $\hat{\theta}$ at different observation distances $\hat{z} = 0.52$, $\hat{z} = 0.6$, $\hat{z} = 1.5$ and $\hat{z} = 100.0$.

- **Two-edge radiation, far zone: $d_{1,2} \gg L$ (i.e. $z \gg L$). Eq. (20) and Eq. (25)**

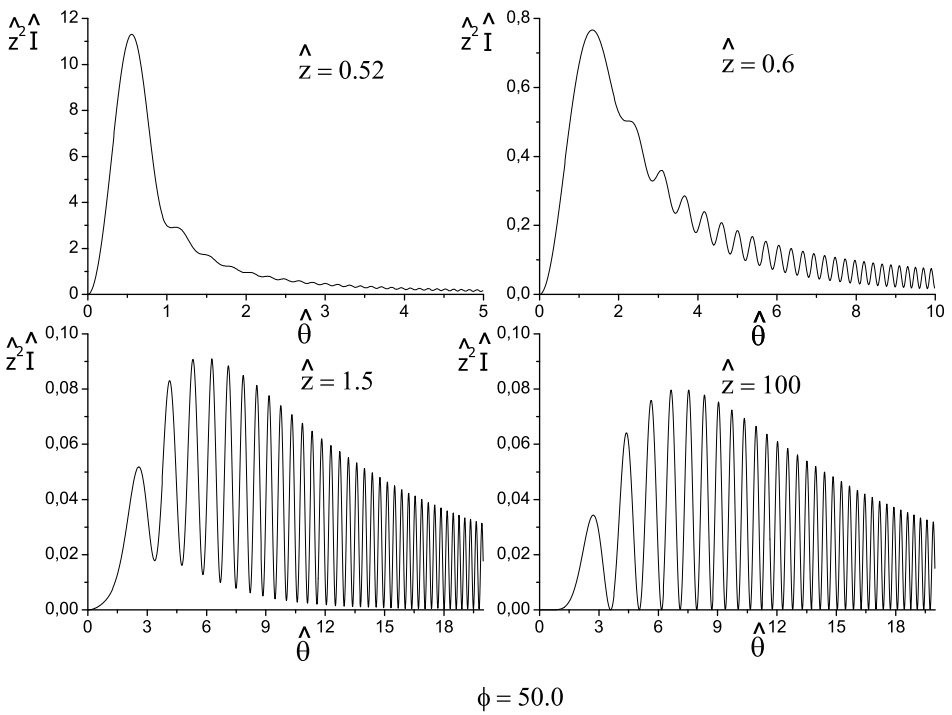

Fig. 13. $\hat{z}^2\hat{I}$ at $\phi = 50$. These profiles are shown as a function of angles at different observation distances $\hat{z} = 0.52$, $\hat{z} = 0.6$, $\hat{z} = 1.5$ and $\hat{z} = 100.0$.

should be used. When $d_{1,2} \gg L$ we are summing far field contributions from the two edge sources. This case is well represented in Fig. 13 for $\hat{z} = 100$, where interference effects between the two edges contribution are clearly visible.

- **Two-edge radiation, near zone: $d_{1,2} \sim L$. Eq. (40) should be used.** When $d_{1,2} \sim L$ the observer is located far away with respect to the formation length of the sources. Both contributions from the sources are important, but that from the nearest source begins to become the main one, as d_1 and d_2 become sensibly different. This case is well represented in Fig. 13 for $\hat{z} = 1.5$.
- **Single-edge radiation, far zone: $\gamma^2 \lambda\!\!\!^{-} \ll d_2 \ll L$ and $r \ll L/\gamma$. Eq. (41) should be used.** When $\gamma^2 \lambda\!\!\!^{-} \ll d_2 \ll L$, the contribution due to the near edge becomes more and more important. Such tendency is clearly depicted in Fig. 13 for $\hat{z} = 0.6$. Interference tends to disappear as the near edge becomes the dominant one. In this case, one finds that the electric field in Eq. (40) reduces to

$$\vec{\vec{E}}\left(z, \vec{\xi}\right) = \frac{2e\gamma^2\vec{\xi}}{c(z - L/2)(\gamma^2\xi^2 + 1)} \exp\left[\frac{i\omega L}{4c\gamma^2}\right] \exp\left[\frac{i\omega L\xi^2}{2c}\left(\frac{z}{L} - \frac{1}{2}\right)\right], \quad (41)$$

where $\xi = r/(z - L/2) = r/d_2$. Note that ξ is used here in place of θ, because by definition $\theta = r/z$, where z is calculated from the center of the straight section, whereas the definition of ξ is related to the edge position at $z = L/2$. It should be remarked that Eq. (41) constitutes the field contribution from the downstream edge of the straight section, and that the contribution from the upstream edge (at $z = -L/2$) can be found from Eq. (41) by performing everywhere in Eq. (41), i.e. also in ξ, the substitution $L/2 \longrightarrow -L/2$, and by changing an overall sign. Eq. (41) corresponds to an angular spectral flux [5]

$$\frac{dW}{d\omega d\Omega} = \frac{e^2}{c\pi^2} \frac{\gamma^4 \xi^2}{\left(\gamma^2 \xi^2 + 1\right)^2} \,. \tag{42}$$

It is important to specify the region of applicability of Eq. (41) in the transverse direction. For a single edge in the far zone, the amplitude of the field decreases as r^{-1}, as can be checked by substituting the definition of $\vec{\xi}$ in Eq. (41), and does not depend on z nor γ for angles of observation larger than $1/\gamma$. Since $d_2 \ll L$, such dependence holds for the upstream edge at $r \gtrsim L/\gamma$, and for the downstream edge at $r \sim d_2/\gamma \ll L/\gamma$. As a result, for $r \gtrsim L/\gamma$, the contributions from the two edges are comparable, and a single-edge asymptote cannot be used. It follows that Eq. (41) applies for $r \ll L/\gamma$.

- **Single-edge radiation, near zone: $\sqrt[3]{\lambda R^2} \ll d_2 \lesssim \gamma^2 \lambda$, $r \ll \gamma \lambda$. Eq. (43) should be used.** When $\sqrt[3]{\lambda R^2} \ll d_2 \lesssim \gamma^2 \lambda$ we have the contribution from a single edge in the near zone.

  As d_2 becomes smaller and smaller the maximum in the radiation profile increases (see Fig. 13). This behavior is to be expected. In fact, on the one hand the virtual source exhibits a singular behavior at $r = 0$, while on the other hand the integral in Eq. (14) must reproduce the virtual source for $z \longrightarrow z_s$. In other words, for $z \longrightarrow z_s$, the propagator must behave like a Dirac δ-distribution. However, the way such asymptote is realized is not trivial. At any finite distance d_2 from the source, Eq. (14) eliminates the singularity of the Bessel K_1 function. This means that the maximum value in $|\vec{\vec{E}}|^2$ increases as d_2 decreases, but it always remains finite. In particular, at $\theta = 0$, $|\vec{\vec{E}}|^2 = 0$. However, by conservation of energy the integral of $|\vec{\vec{E}}|^2 = 0$ over transverse coordinate must diverge at any finite distance from the source, because the field diverges at the source position.

  Note that when $r \ll \gamma \lambda$ and $d_2 \ll \gamma^2 \lambda$, the integral pertaining the near (downstream) edge (at $z_{s2} = L/2$) in Eq. (40) can be calculated analytically. In fact, the Bessel K_1 function in the integrand can be expanded for small values of the argument when $\hat{r}' \ll 1/\sqrt{\phi}$. When this is not the case ($\hat{r}' \gtrsim 1/\sqrt{\phi}$) the phase factor under the integral sign makes the integrand exhibiting oscillatory behavior (because $\hat{z} - 1/2 \ll 1/\phi$, since $d_2\theta \ll \gamma^2 \lambda$).

Contributions to the integrals are therefore negligible. As a result, in this case one can use the expansion $K_1(\sqrt{\phi}\hat{r}') \sim 1/(\sqrt{\phi}\hat{r}')$. Then, using the fact that $\int_0^\infty dx J_1(Ax)\exp[iBr^2] = 1/A\{1-\exp[-iA^2/(4B)]\}$ (for A and B positive), one obtains [8]

$$\vec{\vec{E}}\left(z,\vec{\xi}\right) = \frac{2ie\vec{\xi}}{c\xi^2(z-L/2)}\exp\left[\frac{i\omega L}{4c\gamma^2}\right]\exp\left[\frac{i\omega\xi^2(z-L/2)}{4c}\right] \times \sin\left[\frac{\omega\xi^2(z-L/2)}{4c}\right]. \tag{43}$$

Note that while the modulus of Eq. (43) is independent of ϕ, its region of applicability is related to ϕ and the asymptotic expression deviates from Eq. (40) for smaller value of $\hat{\theta}$ when ϕ is larger. In fact, Eq. (43) is valid only when $\hat{z} - 1/2 \ll 1/\phi$ and $\hat{z}\hat{\theta} \ll 1/\sqrt{\phi}$ (i.e. $r \ll \gamma\lambda$ and $d_2 \ll \gamma^2\lambda$).

It is interesting to remark here that Eq. (32), which was derived for $\phi \ll 1$, reduces to Eq. (43) when $d_2 \ll L$ and $r \ll \sqrt{\lambda L}$. It follows that the validity of Eq. (43) has a wider region of applicability than that considered here. In fact, it may be applied whenever $\sqrt[3]{\lambda R^2} \ll d_2 \ll \min(L, \gamma^2\lambda)$ and $r \ll \sqrt{\lambda\min(L,\gamma^2\lambda)}$.

If we propagate Eq. (43) to the far zone we obtain an asymptote which is valid only for angles much larger than $1/\gamma$ (i.e. Eq. (43) is an asymptote for high values of spatial frequencies). The modulus of Eq. (43) does not depend on γ (while in the non-asymptotic case radiation for any value of z must depend on γ, because the far-field radiation from a single edge depends on γ too) nor it includes information about distribution in the far zone within angles comparable with $1/\gamma$. Thus, the applicability of this high-spatial frequency asymptote depends on what practical (or theoretical) problem we try to solve. It is useful, for example, if we discuss about a sample in the very near zone. However, if we discuss about design of beam line with an acceptance angle comparable with $1/\gamma$ (which is equivalent to some spatial-frequency filter) the asymptotic expression in Eq. (43) cannot be applied anymore, and one should use exact results from the propagation integral, i.e. the near-field expression Eq. (40).

The above-given classification in zones of interest with asymptotical expressions for the electric field constitutes an important result of our paper. In fact, expressions for the electric field without explicit specification of their region of applicability are incomplete, and have no practical nor theoretical utility. From this viewpoint, it is interesting to compare our results with literature. We will limit our discussion to a comparison with recent review [28], which summarizes up-to-date understanding of ER within the SR community.

One result in [28] (Eq. (26)) corresponds to the square modulus of our Eq. (43), the single edge near-zone case. The region of applicability specified

in [28] for such result[4] is $\lambda\!\!\!^{-} \ll d_2 \lesssim \gamma^2 \lambda\!\!\!^{-}$ and $L \longrightarrow \infty$. A first problem in applying this prescription is intrinsic in the condition $L \longrightarrow \infty$, as there is no comparison of L to any other characteristic length. Secondly, this result is independent of γ and L. As a result, it cannot be valid for arbitrary transverse distance r. In fact, since the far-zone field depends on both γ and L, should we propagate Eq. (43) in the far zone, we could never obtain an outcome dependent on γ and L. It follows that, as we discussed above, Eq. (43) is valid for arbitrary L (under the sharp-edge limit $\sqrt[3]{\lambda\!\!\!^{-} R^2} \ll L$), but its region of applicability depends on L or γ: $\sqrt[3]{\lambda\!\!\!^{-} R^2} \ll d_2 \ll \min(L, \gamma^2 \lambda\!\!\!^{-})$ and $r \ll \sqrt{\lambda\!\!\!^{-} \min(L, \gamma^2 \lambda\!\!\!^{-})}$. Note that the requirement $r \ll \lambda\!\!\!^{-}\gamma$ for the applicability of Eq. (43) is present in the original paper [8], but has been omitted in some later publications, e.g. [9, 10, 13]. Because of this the dependence of near-zone single-edge radiation upon γ was unclear, and the asymptotic expression Eq. (43) started to be considered by other authors, as in [28], without proper requirements on r.

A second result in [28] for the case of a finite straight section length L (Eq. (27)) corresponds to our Eq. (34). This fact can be proved with the help of straightforward mathematical steps. The region of applicability of Eq. (27) in [28] is specified by the words "under conditions of validity of equation (26)", i.e. $\lambda\!\!\!^{-} \ll d_2 \lesssim \gamma^2 \lambda\!\!\!^{-}$. In contrast to this, we have seen that Eq. (34) is valid for arbitrary $d_2 \gg \sqrt[3]{\lambda\!\!\!^{-} R^2}$, but includes limitations on L in the form: $\sqrt[3]{\lambda\!\!\!^{-} R^2} \ll L \ll \gamma^2 \lambda\!\!\!^{-}$.

The following result in [28], Eq. (28), is the far-zone single-edge result, i.e. our Eq. (42). Eq. (28) in [28] is presented without region of applicability while, as we have seen, it is valid for $\gamma^2 \lambda\!\!\!^{-} \ll d_2 \ll L$ and $r \ll L/\gamma$. Note that in this case the denomination "far zone" is not related with the usual understanding $d_2 \longrightarrow \infty$, as is the case for the usual far-zone expression for two-edges, but it includes a limit on d_2, i.e. $d_2 \ll L$.

The final result in [28] is Eq. (29), that is our far-zone two-edge case, Eq. (25). Also Eq. (29) is presented without region of applicability while, as we have seen, $d_2 \gg L$.

It should be appreciated how our analysis of ER through the parameter δ allowed us to define "how sharp" the edges are, and to specify the region of applicability for ER theory.

As a final remark, note that in literature the single edge far-zone case is usually presented as the simplest and fundamental case, while in our view this is the most complicated and misleading case to discuss. For the sake of exemplification, consider the usual assumption made in this case, i.e.

[4] Converted to our notation.

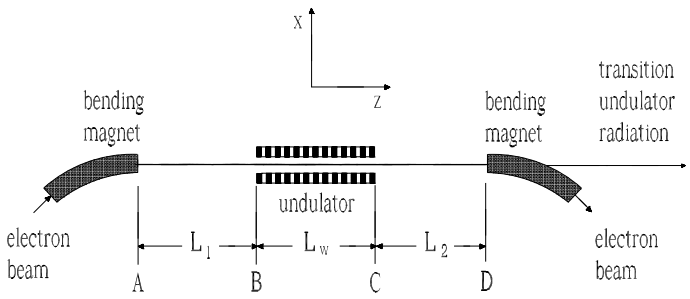

Fig. 14. Transition undulator radiation geometry.

$L \longrightarrow \infty$. In order to discuss the far-zone expression, one needs $z \longrightarrow \infty$, and comparing z to L becomes impossible. In other words, L drops out of from the problem parameters and, as in [28], it never appears in the condition for the region of applicability anymore. In contrast to this, our simplest model is the two-edge far-zone model, whose region of applicability is: $z \gg L$ (or $d_2 \gg L$). It is independent of γ and it is much easier (although an extra-limitation on angles $\theta \ll \sqrt[3]{\lambda\!\!\!^{-}/R}$ should be included, due to the sharp-edge approximation). After introduction of this model, the following natural step was to generalize it to the near zone, introducing more complicated regions of applicability discussed before.

6 Transition undulator radiation

In this Section we apply the method of virtual sources to the more complicated case of an undulator setup.

Instead of the setup in Fig. 1(a), we now consider the system depicted in Fig. 14 and we consider a single particle moving along the system. The electron enters the setup via a bending magnet, passes through a straight section (segment AB), an undulator (segment BC), and another straight section (segment CD). Finally, it leaves the setup via another bend. Radiation is collected at a distance z from the center of the reference system, located in the middle of the undulator. The passage of the electron through the setup results in collimated emission of radiation in the range $\lambda\!\!\!^{-} \gg \lambda\!\!\!^{-}_r$ and $\lambda\!\!\!^{-} \gg \lambda\!\!\!^{-}_c$, where $\lambda\!\!\!^{-}_r$ is the resonance wavelength of the fundamental harmonic of the undulator, i.e. the extra characteristic length introduced in the setup. This kind of radiation is known in literature as Transition Undulator Radiation (TUR) [16, 17, 9, 18, 20]. We will retain this name although, as we will see, what we are really discussing about is edge radiation from an undulator setup.

In our case of study the trajectory and, therefore, the space integration in Eq. (13) can be split in five parts: the two bends, which will be indicated with b_1 and b_2, the two straight sections AB and CD and the undulator BC. One may write

$$\vec{\vec{E}}(z,\vec{r}) = \vec{\vec{E}}_{b1}(z,\vec{r}) + \vec{\vec{E}}_{AB}(z,\vec{r}) + \vec{\vec{E}}_{BC}(z,\vec{r}) + \vec{\vec{E}}_{CD}(z,\vec{r}) + \vec{\vec{E}}_{b2}(z,\vec{r}) \,, \tag{44}$$

with obvious meaning of notation.

We will denote the length of the segment AD with L_{tot}, while we will indicate the length of the straight section AB with L_1, the length of the straight section CD with L_2 and the length of the undulator with L_w. It follows that $L_{\text{tot}} = L_1 + L_w + L_2$. This means that point A is located at longitudinal coordinate $z_A = -L_1 - L_w/2$, while B, C and D are located respectively at $z_B = -L_w/2$, $z_C = L_w/2$ and $z_D = L_w/2 + L_2$.

We will describe the field from our TUR setup as a superposition of three laser-like beam from straight sections and undulator. As before, with the help of Eq. (13) we will first derive an expression for the field in the far zone. Then we will calculate the field distribution at the virtual source with the help of Eq. (16). Finally, Eq. (17) will allow us to find an expression for the field both in the near and in the far zone.

6.1 Far field from the undulator setup

Let us describe the far field from the undulator setup in Fig. 14 by separately characterizing different field contributions and finally adding them together.

6.1.1 Field contribution calculated along the undulator

We first consider the contribution $\vec{\vec{E}}_{BC}$ from the undulator. Assuming a planar undulator with N_w periods we write the following expression for the transverse velocity of an electron:

$$\vec{v}_\perp(z) = -\frac{cK}{\gamma} \sin(k_w z)\vec{x} \,. \tag{45}$$

Here $K = (\lambda_w e H_w)/(2\pi m_e c^2)$ is the undulator parameter, m_e being the electron mass and H_w being the maximum of the magnetic field produced by the undulator on the z axis. Moreover, $k_w = 2\pi/\lambda_w$, where λ_w is the undulator

period, so that the undulator length is $L_w = N_w \lambda_w$. The transverse position of the electron is

$$\vec{r}_0(z) = \frac{K}{\gamma k_w} \cos(k_w z)\vec{x}\,. \tag{46}$$

We can now substitute Eq. (46) and Eq. (45) in Eq. (13). Such substitution leads to an expression valid in the far zone. We obtain

$$\vec{\tilde{E}}_{BC}(z, \vec{r}, \omega) = \frac{i\omega e}{c^2 z} \int_{z_B}^{z_C} dz' \exp\left[i\Phi_{BC}\right] \left\{ \left[\frac{K}{\gamma} \sin(k_w z') + \theta_x \right] \vec{x} + \theta_y \vec{y} \right\}\,. \tag{47}$$

Here

$$\Phi_{BC} = \frac{\omega}{c} \left\{ \frac{\theta^2}{2} z + \frac{z'}{2} \left(\frac{1}{\bar{\gamma}_z^2} + \theta^2 \right) - \frac{K\theta_x}{\gamma k_w} \cos(k_w z') - \frac{K^2}{8\gamma^2 k_w} \sin(2k_w z') \right\}\,, \tag{48}$$

where the average longitudinal Lorentz factor $\bar{\gamma}_z$ in Eq. (48) turns out to be $\bar{\gamma}_z = \gamma/\sqrt{1 + K^2/2}$, and is always smaller than γ because the average longitudinal velocity of the electron inside the undulator is smaller than that along the straight sections.

In this paper we will be interested up to frequencies much lower than the resonance frequency, i.e. $\lambda\!\!\!^{-} \gg \lambda\!\!\!^{-}_r$, with $\lambda\!\!\!^{-}_r = 1/(2\bar{\gamma}_z^2 k_w)$.

We can show that this condition is analogous, for TUR radiation, to condition $\phi \cdot \delta \ll 1$ for the simple edge radiation setup in Fig. 1(a). In order to do so, we first need to discuss the formation length associated with the undulator, i.e. with Eq. (47). The definition of formation length was introduced before as the value of $z_2 - z_1$ for which the right hand side of Eq. (8) is of order unity. However, the physical meaning of formation length is related with the integration range in z' such that the integrand in Eq. (47) exhibits an oscillatory behavior. In our case, not only the phase in Eq. (48), but also the $\sin(\cdot)$ term in Eq. (47) have an oscillatory character, and must be taken into account when calculating the formation length. As a result, in the long-wavelength asymptotic ($\lambda\!\!\!^{-} \gg \lambda\!\!\!^{-}_r$), we deal with a situation where the $\sin(\cdot)$ and the $\vec{\theta}$ terms in Eq. (47) have different formation lengths. From the $\sin(\cdot)$ term in Eq. (47) and from Eq. (48) follows a formation length $L_f = \lambda\!\!\!^{-}_w$, and a characteristic angle $\theta \sim \sqrt{\lambda\!\!\!^{-}/\lambda\!\!\!^{-}_w}$. However, the TUR contribution is given by the terms in θ_x and θ_y in Eq. (47). For these terms, from Eq. (48) follows a formation length $L_f \sim \min(\bar{\gamma}_z^2 \lambda\!\!\!^{-}, N_w \lambda\!\!\!^{-}_w)$, in the limit for $\lambda\!\!\!^{-} \gg \lambda\!\!\!^{-}_r$. In this limit, the TUR contribution is collimated to angles $\theta^2 \ll \lambda\!\!\!^{-}/\lambda\!\!\!^{-}_w$. Only within these conditions one can properly talk about TUR. Note that $L_f \gg \lambda\!\!\!^{-}_w$ always,

because $\bar{\gamma}_z^2 \lambda\!\!\!^{-} \sim \lambda\!\!\!^{-}_w \lambda\!\!\!^{-}/\lambda\!\!\!^{-}_r \gg \lambda\!\!\!^{-}_w$ and we assume $N_w \gg 1$. The expression for the formation length L_f above is analogous to that for edge radiation, which is given by $\min(\gamma^2 \lambda\!\!\!^{-}, L)$. The analogous of the ϕ parameter is now given by $\phi_w = \lambda\!\!\!^{-}_w N_w/(\bar{\gamma}_z^2 \lambda\!\!\!^{-})$, while the analogous of the δ parameter is $\delta_w = \lambda\!\!\!^{-}_w/(\lambda\!\!\!^{-}_w N_w) = 1/N_w \ll 1$, as $N_w \gg 1$. It follows that $\phi_w \cdot \delta_w = \lambda\!\!\!^{-}_w/(\bar{\gamma}_z^2 \lambda\!\!\!^{-}) \sim \lambda\!\!\!^{-}_r/\lambda\!\!\!^{-} \ll 1$.

For $\phi_w \cdot \delta_w \ll 1$ and $\delta_w \ll 1$ the contribution due to the term in $\sin(k_w z')$ in Eq. (47) can always be neglected when compared with the maximal field magnitude of the terms in $\theta_{x,y}$. Similarly, in Eq. (48), phase terms in $\cos(k_w z')$ and $\sin(2k_w z')$ can also be neglected. As a result, Eq. (47) can be simplified as

$$\vec{\vec{E}}_{BC}(z, \vec{r}, \omega) = \frac{i\omega e}{c^2 z} \int_{z_B}^{z_C} dz' \exp\left[i\Phi_{BC}\right] \left(\theta_x \vec{x} + \theta_y \vec{y}\right) \tag{49}$$

where

$$\Phi_{BC} = \frac{\omega}{c} \left[\frac{\theta^2}{2} z + \frac{z'}{2} \left(\frac{1}{\bar{\gamma}_z^2} + \theta^2 \right) \right] . \tag{50}$$

6.1.2 Field contribution calculated along the straight sections

With the help of Eq. (13) we write the contribution from the straight line AB as

$$\vec{\vec{E}}_{AB} = \frac{i\omega e}{c^2 z} \int_{z_A}^{z_B} dz' \exp\left[i\Phi_{AB}\right] \left(\theta_x \vec{x} + \theta_y \vec{y}\right) \tag{51}$$

where Φ_{AB} in Eq. (51) is given by

$$\Phi_{AB} = \frac{\omega}{c} \left[\frac{\theta^2}{2} z + \frac{z'}{2} \left(\frac{1}{\gamma^2} + \theta^2 \right) - \frac{L_w}{4\bar{\gamma}_z^2} + \frac{L_w}{4\gamma^2} \right] , \tag{52}$$

The contribution from the straight section CD is similar to that from the straight section AB and reads

$$\vec{\vec{E}}_{CD} = \frac{i\omega e}{c^2 z} \int_{z_C}^{z_D} dz' \exp\left[i\Phi_{CD}\right] \left(\theta_x \vec{x} + \theta_y \vec{y}\right) \tag{53}$$

where Φ_{CD} in Eq. (53) is given by

$$\Phi_{CD} = \frac{\omega}{c}\left[\frac{\theta^2}{2}z + \frac{z'}{2}\left(\frac{1}{\gamma^2} + \theta^2\right) + \frac{L_w}{4\bar{\gamma}_z^2} - \frac{L_w}{4\gamma^2}\right]. \tag{54}$$

In general, the phases Φ_{CD} and Φ_{AB} start exhibiting oscillatory behavior when $z'/(2\gamma^2\lambda\!\!\!^{-}) \sim 1$, which gives a maximal integration range in the longitudinal direction. Similarly as before, in general one has that the formation lengths L_{fs1} and L_{fs2} for the straight sections AB and CD can be written as $L_{\mathrm{fs}(1,2)} \sim \min\left[\lambda\!\!\!^{-}\gamma^2, L_{(1,2)}\right]$.

6.1.3 *Total field and energy spectrum of radiation*

The contributions for segment AB and segment CD are given by Eq. (51) and Eq. (53). One obtains

$$\begin{aligned}\vec{\tilde{E}}_{AB} = {} & \frac{i\omega e L_1}{c^2 z}\exp\left[\frac{i\omega\theta^2 z}{2c}\right]\vec{\theta}\,\mathrm{sinc}\left[\frac{\omega L_1}{4c}\left(\frac{1}{\gamma^2} + \theta^2\right)\right] \\ & \times\exp\left[-\frac{i\omega L_w}{4c}\left(\frac{1}{\bar{\gamma}_z^2} + \theta^2\right)\right]\exp\left[-\frac{i\omega L_1}{4c}\left(\frac{1}{\gamma^2} + \theta^2\right)\right]\end{aligned} \tag{55}$$

Similarly,

$$\begin{aligned}\vec{\tilde{E}}_{CD} = {} & \frac{i\omega e L_2}{c^2 z}\exp\left[\frac{i\omega\theta^2 z}{2c}\right]\vec{\theta}\,\mathrm{sinc}\left[\frac{\omega L_2}{4c}\left(\frac{1}{\gamma^2} + \theta^2\right)\right] \\ & \times\exp\left[\frac{i\omega L_w}{4c}\left(\frac{1}{\bar{\gamma}_z^2} + \theta^2\right)\right]\exp\left[\frac{i\omega L_2}{4c}\left(\frac{1}{\gamma^2} + \theta^2\right)\right]\end{aligned} \tag{56}$$

Finally, the contribution for the segment BC is obtained from Eq. (49). Calculations yield:

$$\vec{\tilde{E}}_{BC} = \frac{i\omega e L_w}{c^2 z}\exp\left[\frac{i\omega\theta^2 z}{2c}\right]\vec{\theta}\,\mathrm{sinc}\left[\frac{\omega L_w}{4c}\left(\frac{1}{\bar{\gamma}_z^2} + \theta^2\right)\right] \tag{57}$$

The total field produced by the setup is obtained by summing up Eq. (55), Eq. (56) and Eq. (57). By this, we are neglecting bending magnet contributions. A sufficient condition (in addition to the already accepted ones, $N_w \gg 1$ and $\lambda\!\!\!^{-}/\lambda\!\!\!^{-}_r \gg 1$) is $\lambda\!\!\!^{-} \gg R/\bar{\gamma}_z^3$. In fact, we may neglect bending magnet contributions for $\delta_{1,2} \ll 1$, but in this setup $L_{1,2}$ may be set to zero, in which

case we should also impose that the formation length of the bend be much shorter than $\bar{\gamma}_z^2 \lambda\!\!\!^{-}$, which reduces to $\lambda\!\!\!^{-} \gg R/\bar{\gamma}_z^3$.

As before, the observation angle is measured starting from the center of the undulator, located at $z = 0$, i.e. $\vec{\theta} = \vec{r}/z$. The angular spectral flux can be written substituting the resultant total field in Eq. (24). We obtain

$$\begin{aligned}
\frac{dW}{d\omega d\Omega} = \frac{e^2}{\pi^2 c}\frac{\gamma^4\theta^2}{\left(1+\gamma^2\theta^2\right)^2}\Bigg| &- \exp\left[-i\frac{\omega L_w}{4c\gamma^2}\left(1+\frac{K^2}{2}+\gamma^2\theta^2\right)\right] \\
&+ \exp\left[-i\frac{\omega L_1}{2c\gamma^2}\left(1+\gamma^2\theta^2\right) - i\frac{\omega L_w}{4c\gamma^2}\left(1+\frac{K^2}{2}+\gamma^2\theta^2\right)\right] \\
&+ \frac{1/\gamma^2+\theta^2}{1/\bar{\gamma}_z^2+\theta^2}\left\{-\exp\left[\frac{i\omega L_w}{4c\gamma^2}\left(1+\frac{K^2}{2}+\gamma^2\theta^2\right)\right]\right. \\
&\left.+\exp\left[-\frac{i\omega L_w}{4c\gamma^2}\left(1+\frac{K^2}{2}+\gamma^2\theta^2\right)\right]\right\} + \exp\left[i\frac{\omega L_w}{4c\gamma^2}\left(1+\frac{K^2}{2}+\gamma^2\theta^2\right)\right] \\
&- \exp\left[i\frac{\omega L_2}{2c\gamma^2}\left(1+\gamma^2\theta^2\right) + \frac{i\omega L_w}{4c\gamma^2}\left(1+\frac{K^2}{2}+\gamma^2\theta^2\right)\right]\Bigg|^2 ,
\end{aligned} \tag{58}$$

that is equivalent to the analogous expression in [9].

Note that L_1, L_2 and L_w can assume different values. γ and $\bar{\gamma}_z$ are also different. It may therefore seem convenient to introduce different normalized quantities, referring to the undulator and the straight lines. However, in the end we are interested in summing up all contributions from different sources, so that it is important to keep a common definition of vertical displacement (or observation angle). Therefore we prescribe the same normalization for all quantities:

$$\hat{\vec{\theta}} = \sqrt{\frac{L_{\text{tot}}}{\lambda\!\!\!^{-}}}\vec{\theta}\,, \phi_t = \frac{L_{\text{tot}}}{\gamma^2\lambda\!\!\!^{-}} \quad \text{and} \quad \hat{\vec{r}} = \frac{\vec{r}}{\sqrt{L_{\text{tot}}\lambda\!\!\!^{-}}}\,. \tag{59}$$

Then, we introduce parameters $\hat{L}_1 = L_1/L_{\text{tot}}$, $\hat{L}_2 = L_2/L_{\text{tot}}$, $\hat{L}_w = L_w/L_{\text{tot}}$, $\phi_{1,2} = L_{1,2}/(\gamma^2\lambda\!\!\!^{-}) = \hat{L}_{1,2}\phi_t$ and $\phi_w = L_w/(\bar{\gamma}_z^2\lambda\!\!\!^{-})$, as seen above. Here it should be clear that ϕ_t has been introduced only for notational convenience, while real parameters related to the physics of the problem are $\phi_{1,2}$. Finally, we define $\hat{z}_s = z_s/L_{\text{tot}}$. From Eq. (58) follows

$$\begin{aligned}
\hat{z}^2\hat{I} = \frac{4\hat{\theta}^2}{(\phi_t+\hat{\theta}^2)^2}\Bigg| &\exp\left[-\frac{i\hat{L}_1}{2}\left(\phi_t+\hat{\theta}^2\right) - \frac{i}{4}\left(\phi_w+\hat{L}_w\hat{\theta}^2\right)\right] - \exp\left[-\frac{i}{4}\left(\phi_w+\hat{L}_w\hat{\theta}^2\right)\right] \\
&+ \frac{\phi_t+\hat{\theta}^2}{\phi_w/\hat{L}_w+\hat{\theta}^2}\left\{-\exp\left[\frac{i}{4}\left(\phi_w+\hat{L}_w\hat{\theta}^2\right)\right] + \exp\left[-\frac{i}{4}\left(\phi_w+\hat{L}_w\hat{\theta}^2\right)\right]\right\}
\end{aligned}$$

$$- \exp\left[\frac{i\hat{L}_2}{2}\left(\phi_t + \hat{\theta}^2\right) + \frac{i}{4}\left(\phi_w + \hat{L}_w\hat{\theta}^2\right)\right] + \exp\left[\frac{i}{4}\left(\phi_w + \hat{L}_w\hat{\theta}^2\right)\right]\Bigg|^2 , \qquad (60)$$

where $\hat{I} = \left|\vec{\hat{E}}\right|^2$ and $\vec{\hat{E}} \equiv \vec{\bar{E}}\sqrt{\lambda L_{\text{tot}}}\, c/e$. Note that outside the undulator the longitudinal velocity is nearer to c than inside ($\bar{\gamma}_z^2 < \gamma^2$). It follows that the contribution of the undulator is suppressed compared with that of the straight sections, and in the case of comparable lengths and $K^2 \gg 1$, the straight section contribution becomes dominant.

In the special case for $\hat{L}_1 = \hat{L}_2 = \hat{L}_w \equiv \hat{L}/3$, $\phi_{1,2} = \phi_t/3$, and Eq. (60) simplifies to

$$\hat{z}^2\hat{I} = \frac{4\hat{\theta}^2}{(\phi_t + \hat{\theta}^2)^2}\Bigg| - 4i\cos\left[\frac{\hat{L}}{12}\left(2\hat{\theta}^2 + \phi_t\right) + \frac{\phi_w}{4}\right]\sin\left[\frac{\hat{L}}{12}\left(\hat{\theta}^2 + \phi_t\right)\right]$$
$$-2i\frac{\phi_t + \hat{\theta}^2}{3\phi_w/\hat{L} + \hat{\theta}^2}\sin\left[\frac{1}{12}\left(3\phi_w + \hat{L}\hat{\theta}^2\right)\right]\Bigg|^2 . \qquad (61)$$

Eq. (61) can be readily evaluated. As an example, we can calculate the intensity distribution of TUR emitted by the SASE 1 European XFEL setup at a wavelength $\lambda = 400$ nm. We assume that the XFEL operates at 17.5 GeV. Setup parameters are $L_1 = L_w = L_2 = 200$ m, $R = 400$ m, $K = 3.3$ and $\lambda_w = 3.56$ cm [21]. In this case $\delta \sim 10^{-3}$ and $\delta_w \sim 1/N_w \sim 10^{-4}$, while $\phi_t \simeq 8.0$ and $\phi_w \simeq 52$. Results are plotted in Fig. 15. In that figure, we also propose a comparison with outcomes from SRW at $z = 6000$ m (vertical and horizontal cuts).

In the far zone, well-accepted expressions for the TUR emission are reported in literature [16, 17, 18, 20], that are equivalent to the following equation for the radiation energy density as a function of angle and frequency:

$$\frac{dW}{d\omega d\Omega} = \frac{e^2}{\pi^2 c}\left[\frac{2\gamma^2\theta K^2}{(1 + K^2/2 + \gamma^2\theta^2)(1 + \gamma^2\theta^2)}\right]^2 \sin^2\left[\frac{\pi L_w}{2\gamma^2\lambda}\left(1 + \frac{K^2}{2} + \gamma^2\theta^2\right)\right]. \qquad (62)$$

We will show that Eq. (62) cannot be applied for TUR calculations. In our understanding, there cannot be any range of parameters in the setup in Fig. 14 where Eq. (62) is valid.

In order to prove this it is sufficient to compare Eq. (62) with Eq. (58). Eq. (62) does not depend on the straight section lengths L_1 or L_2, and can be applied when $L_1,\ L_2 \longrightarrow 0$.

However, in that limit, Eq. (58) reduces to:

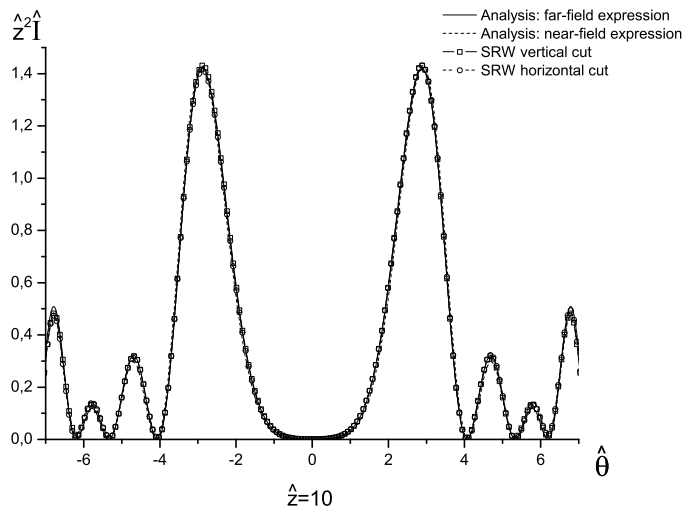

Fig. 15. Cross-check of Eq. (61) with the help of SRW. Here $L_1 = L_w = L_2 = 200$ m, $E = 17.5$ GeV, $\lambda = 400$ nm, $R = 400$ m, and $K = 3.3$. Here $\lambda_w = 3.56$ cm. The observer is located at $z = 6000$ m. Circles represent horizontal and vertical cuts of the intensity profiles calculated numerically with SRW. The solid curve is calculated with Eq. (61). The dashed curve is obtained with the near-zone expressions Eqs. (69)-(72).

$$\frac{dW}{d\omega d\Omega} = \frac{e^2}{\pi^2 c}\left[\frac{2\gamma^2\theta}{1+K^2/2+\gamma^2\theta^2}\right]^2 \sin^2\left[\frac{\pi L_w}{2\gamma^2\lambda}\left(1+\frac{K^2}{2}+\gamma^2\theta^2\right)\right], \tag{63}$$

that is obviously different from Eq. (62). Also note that in the limit for $K \longrightarrow 0$ Eq. (62) tends to zero, whereas Eq. (63) gives back Eq. (25) as it must be.

6.2 Virtual source characterization and field propagation

There is a general need, in the FEL community, to extend the current theory of TUR to cover the near zone. For instance, a possible use of coherent TUR to produce visible light synchronized with X-rays from an X-ray free-electron laser is discussed in [24]. As we have seen, TUR can be discussed as a more complicated edge-radiation setup. Within the sharp-edge approximation we have contributions from three parts, two straight lines and the undulator. The undulator contribution is similar to a straight line contribution, the only difference being a different average longitudinal velocity of the electron. Then, the far-zone region can be identified by distances $z \gg L_{tot}$.

Expressions in Eq. (55), Eq. (56) and Eq. (57) can be interpreted as far field radiation from separate virtual sources. For each far field contribution we use a picture with two virtual sources, located at the ends of the straight

sections and of the undulator. This makes a total of six sources. However, since the virtual source at the downstream [upstream] edge of the first [second] straight section has the same longitudinal position of the virtual source at the upstream [downstream] edge of the undulator, i.e. $z = -L_w/2$ [$z = L_w/2$], we combine them together, summing them up by superposition principle. As a result, we are left with only four sources, located at

$$z_{s1} = -\frac{L_w}{2} - L_1 \,, \quad z_{s2} = -\frac{L_w}{2} \,, \quad z_{s3} = \frac{L_w}{2} \,, \quad \text{and} \quad z_{s4} = \frac{L_w}{2} + L_2 \,. \tag{64}$$

We obtain an explicit expression for these sources with the help of Eq. (55), Eq. (56) and Eq. (57), proceeding analogously as in Section 5.2:

$$\vec{\vec{E}}_{s1}\left(-\frac{L_w}{2} - L_1, \vec{r}\right) = \frac{2\omega e}{c^2\gamma} \exp\left[-\frac{i\omega L_1}{2c\gamma^2}\right] \exp\left[-\frac{i\omega L_w}{4c\gamma_z^2}\right] \frac{\vec{r}}{r} K_1\left(\frac{\omega r}{c\gamma}\right) \,, \tag{65}$$

$$\begin{aligned} \vec{\vec{E}}_{s2}\left(-\frac{L_w}{2}, \vec{r}\right) = &-\frac{2\omega e}{c^2\gamma} \exp\left[-\frac{i\omega L_w}{4c\gamma_z^2}\right] \frac{\vec{r}}{r} K_1\left(\frac{\omega r}{c\gamma}\right) \\ &+\frac{2\omega e}{c^2\gamma_z} \exp\left[-\frac{i\omega L_w}{4c\gamma_z^2}\right] \frac{\vec{r}}{r} K_1\left(\frac{\omega r}{c\gamma_z}\right) \,, \end{aligned} \tag{66}$$

$$\begin{aligned} \vec{\vec{E}}_{s3}\left(\frac{L_w}{2}, \vec{r}\right) = &-\frac{2\omega e}{c^2\gamma_z} \exp\left[\frac{i\omega L_w}{4c\gamma_z^2}\right] \frac{\vec{r}}{r} K_1\left(\frac{\omega r}{c\gamma_z}\right) \\ &+\frac{2\omega e}{c^2\gamma} \exp\left[\frac{i\omega L_w}{4c\gamma_z^2}\right] \frac{\vec{r}}{r} K_1\left(\frac{\omega r}{c\gamma}\right) \,, \end{aligned} \tag{67}$$

$$\vec{\vec{E}}_{s4}\left(\frac{L_w}{2} + L_2, \vec{r}\right) = -\frac{2\omega e}{c^2\gamma} \exp\left[\frac{i\omega L_2}{2c\gamma^2}\right] \exp\left[\frac{i\omega L_w}{4c\gamma_z^2}\right] \frac{\vec{r}}{r} K_1\left(\frac{\omega r}{c\gamma}\right) \,. \tag{68}$$

In order to calculate the field at any distance z we proceed in analogy with Eq. (40), applying the propagation formula Eq. (14). As before, the above given equations for the sources can also be used as input to any Fourier code to calculate the field evolution in the presence of whatever optical beamline. However, here we restrict ourselves to the free-space case. In order to simplify the presentation of the electric field we take advantage of polar coordinates and we use the definition $\vec{\hat{E}} \equiv \vec{\vec{E}} \sqrt{\lambda L_{\text{tot}}}\, c/e$ (so that $\hat{I}$, introduced in Eq. (26), is given by $\hat{I} = |\vec{\hat{E}}|^2$) for the field in normalized units.

Note that here $\hat{z} = z/L_{\rm tot}$. We obtain four field contributions, one for each source:

$$\hat{z}\vec{\hat{E}}_1\left(\hat{z},\vec{\hat{\theta}}\right) = -\left\{\frac{\vec{\hat{\theta}}}{\hat{\theta}}\frac{2\hat{z}\sqrt{\phi_t}\exp[-i\hat{L}_1\phi_t/2]\exp\left[-i\phi_w/4\right]}{\hat{z}+\hat{L}_w/2+\hat{L}_1}\right.$$
$$\times\int_0^\infty d\hat{r}'\hat{r}'K_1\left(\sqrt{\phi_t}\hat{r}'\right)J_1\left(\frac{\hat{\theta}\hat{r}'\hat{z}}{\hat{z}+\hat{L}_w/2+\hat{L}_1}\right)$$
$$\left.\times\exp\left[\frac{i\hat{r}'^2}{2\left(\hat{z}+\hat{L}_w/2+\hat{L}_1\right)}\right]\exp\left[\frac{i\hat{\theta}^2\hat{z}^2}{2\left(\hat{z}+\hat{L}_w/2+\hat{L}_1\right)}\right]\right\}\ . \qquad (69)$$

$$\hat{z}\vec{\hat{E}}_2\left(\hat{z},\vec{\hat{\theta}}\right) = \left\{\frac{\vec{\hat{\theta}}}{\hat{\theta}}\frac{2\hat{z}\sqrt{\phi_t}\exp\left[-i\phi_w/4\right]}{\hat{z}+\hat{L}_w/2}\exp\left[\frac{i\hat{\theta}^2\hat{z}^2}{2\left(\hat{z}+\hat{L}_w/2\right)}\right]\right.$$
$$\left.\times\int_0^\infty d\hat{r}'\hat{r}'K_1\left(\sqrt{\phi_t}\hat{r}'\right)J_1\left(\frac{\hat{\theta}\hat{r}'\hat{z}}{\hat{z}+\hat{L}_w/2}\right)\exp\left[\frac{i\hat{r}'^2}{2\left(\hat{z}+\hat{L}_w/2\right)}\right]\right\}$$
$$-\left\{\frac{\vec{\hat{\theta}}}{\hat{\theta}}\frac{2\hat{z}\sqrt{\phi_w/\hat{L}_w}\exp\left[-i\phi_w/4\right]}{\hat{z}+\hat{L}_w/2}\exp\left[\frac{i\hat{\theta}^2\hat{z}^2}{2\left(\hat{z}+\hat{L}_w/2\right)}\right]\right.$$
$$\left.\times\int_0^\infty d\hat{r}'\hat{r}'K_1\left(\sqrt{\phi_w/\hat{L}_w}\hat{r}'\right)J_1\left(\frac{\hat{\theta}\hat{r}'\hat{z}}{\hat{z}+\hat{L}_w/2}\right)\exp\left[\frac{i\hat{r}'^2}{2\left(\hat{z}+\hat{L}_w/2\right)}\right]\right\} \qquad (70)$$

$$\hat{z}\vec{\hat{E}}_3\left(\hat{z},\vec{\hat{\theta}}\right) = -\left\{\frac{\vec{\hat{\theta}}}{\hat{\theta}}\frac{2\hat{z}\sqrt{\phi_t}\exp\left[i\phi_w/4\right]}{\hat{z}-\hat{L}_w/2}\exp\left[\frac{i\hat{\theta}^2\hat{z}^2}{2\left(\hat{z}-\hat{L}_w/2\right)}\right]\right.$$
$$\left.\times\int_0^\infty d\hat{r}'\hat{r}'K_1\left(\sqrt{\phi_t}\hat{r}'\right)J_1\left(\frac{\hat{\theta}\hat{r}'\hat{z}}{\hat{z}-\hat{L}_w/2}\right)\exp\left[\frac{i\hat{r}'^2}{2\left(\hat{z}-\hat{L}_w/2\right)}\right]\right\}$$
$$+\left\{\frac{\vec{\hat{\theta}}}{\hat{\theta}}\frac{2\hat{z}\sqrt{\phi_w/\hat{L}_w}\exp\left[i\phi_w/4\right]}{\hat{z}-\hat{L}_w/2}\exp\left[\frac{i\hat{\theta}^2\hat{z}^2}{2\left(\hat{z}-\hat{L}_w/2\right)}\right]\right.$$
$$\left.\times\int_0^\infty d\hat{r}'\hat{r}'K_1\left(\sqrt{\phi_w/\hat{L}_w}\hat{r}'\right)J_1\left(\frac{\hat{\theta}\hat{r}'\hat{z}}{\hat{z}-\hat{L}_w/2}\right)\exp\left[\frac{i\hat{r}'^2}{2\left(\hat{z}-\hat{L}_w/2\right)}\right]\right\} \qquad (71)$$

$$\hat{z}\vec{\hat{E}}_4\left(\hat{z},\vec{\hat{\theta}}\right)=\left\{\frac{\vec{\hat{\theta}}}{\hat{\theta}}\frac{2\hat{z}\sqrt{\phi_t}\exp\left[i\hat{L}_2\phi_t/2\right]\exp\left[i\phi_w/4\right]}{\hat{z}-\hat{L}_w/2-\hat{L}_2}\right.$$
$$\times\int_0^\infty d\hat{r}'\hat{r}'K_1\left(\sqrt{\phi_t}\hat{r}'\right)J_1\left(\frac{\hat{\theta}\hat{r}'\hat{z}}{\hat{z}-\hat{L}_w/2-\hat{L}_2}\right)$$
$$\left.\times\exp\left[\frac{i\hat{r}'^2}{2\left(\hat{z}-\hat{L}_w/2-\hat{L}_2\right)}\right]\exp\left[\frac{i\hat{\theta}^2\hat{z}^2}{2\left(\hat{z}-\hat{L}_w/2-\hat{L}_2\right)}\right]\right\}. \qquad (72)$$

Eqs. (69) to (72) can be used to calculate the field, and hence the intensity, at any position of interest in the far and in the near zone. Obviously, in the far zone, for $\hat{z}\gg 1$, the square modulus of their sum reduces to Eq. (61). As before, It is interesting to cross-check Eqs. (69) to (72) with the computer code SRW. We used the same numerical parameters as before: $L_1 = L_w = L_2 = 200$ m, $E = 17.5$ GeV, $\lambda = 400$ nm and $R = 400$ m, with an undulator parameter $K = 3.3$. Additionally, we chose different values $z = 360$m, $z = 600$m, $z = 1200$m (see Figs. 16 ÷ 18), and $z = 6000$m (see Fig. 15), corresponding to $\hat{z} = 0.6$, $\hat{z} = 1.0$, $\hat{z} = 1.5$, $\hat{z} = 2.0$ and $\hat{z} = 10$ (which is the far-zone case treated before). Here the bending plane is the horizontal plane. As the observation point becomes nearer to the edge of the magnet, the influence of the bending magnet becomes more and more important, an effect which is evident in the figures from the horizontal cuts of SRW two-dimensional intensity profiles. From Figs. 15÷18 we can see that the analytical result for the vertical cut is valid with good accuracy up to $\hat{z} = 0.6$.

7 Edge radiation in a waveguide

In the previous Sections we considered edge radiation propagating in unbounded space. In this Section we extend previous considerations to account for the presence of metallic surroundings (like e.g. the electron vacuum chamber), which effectively act like a waveguide.

The need to account for guiding structures in edge radiation setups arises when one wants to operate in the sub-millimeter wavelength range. Emission of edge radiation in the presence of metallic boundaries has been a much less-treated subject in literature, compared to the unbounded space case. To the best of our knowledge, there is only one article reporting on edge radiation from electrons in a planar overmoded metallic waveguide [14]. The analysis in [14] is based on Lienard-Wiechert fields, modified by the presence of finite metallic boundary. To account for perfectly conducting plates, the author of [14] uses a generalization of the method of images, well-

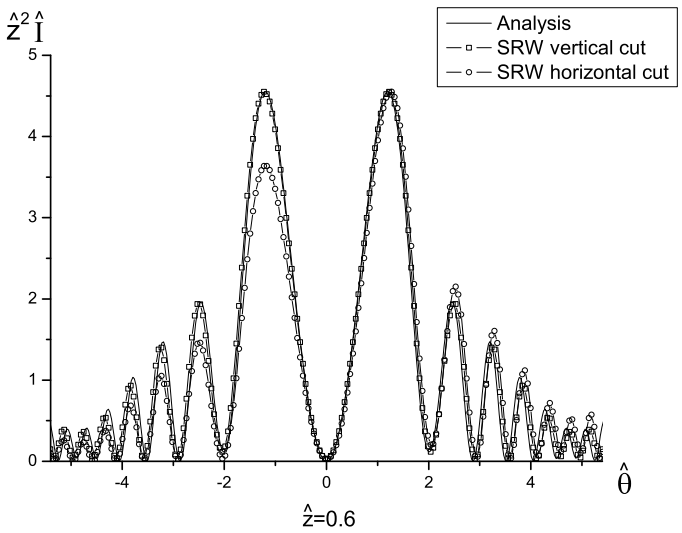

Fig. 16. Cross-check of analytical results with SRW. Here $L_1 = L_w = L_2 = 200$ m, $E = 17.5$ GeV, $\lambda = 400$ nm, $R = 400$ m, and $K = 3.3$. The observer is located at $z = 360$ m. Here $\lambda_w = 3.56$ cm. Horizontal and vertical cuts of the intensity profiles are compared with results obtained with the help of Eqs. (69) to (72).

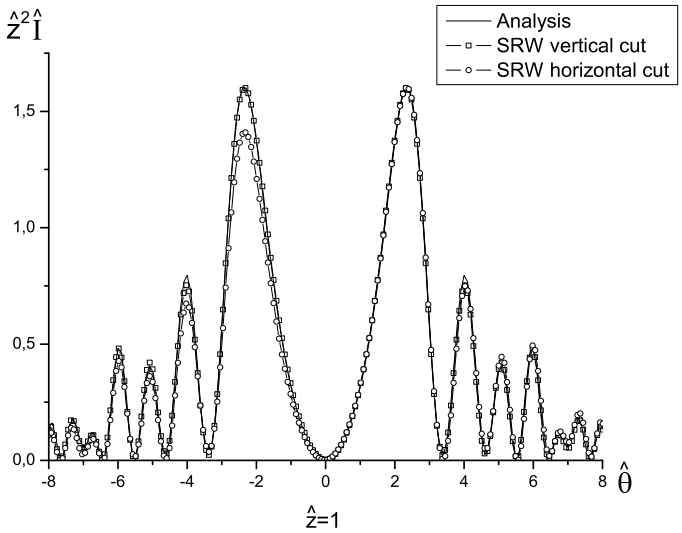

Fig. 17. Cross-check of analytical results with SRW. Here $L_1 = L_w = L_2 = 200$ m, $E = 17.5$ GeV, $\lambda = 400$ nm, $R = 400$ m, and $K = 3.3$. Here $\lambda_w = 3.56$ cm. The observer is located at $z = 600$ m. Horizontal and vertical cuts of the intensity profiles are compared with results obtained with the help of Eqs. (69) to (72).

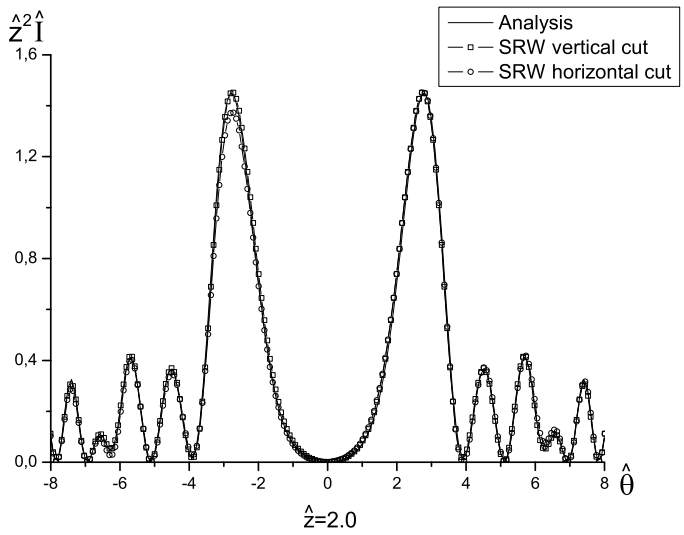

Fig. 18. Cross-check of analytical results with SRW. Here $L_1 = L_w = L_2 = 200$ m, $E = 17.5$ GeV, $\lambda = 400$ nm, $R = 400$ m, and $K = 3.3$. Here $\lambda_w = 3.56$ cm. The observer is located at $z = 1200$ m. Horizontal and vertical cuts of the intensity profiles are compared with results obtained with the help of Eqs. (69) to (72).

known from electrostatics [31]. Instead of this approach, here we prefer to use a mode-expansion technique. We characterize radiation from particles in guiding structures with the help of the proper tensor Green's function, automatically accounting for boundary conditions. The Green's function itself and the field are then conveniently expressed in terms of the natural modes of the guiding structure. This approach is shown to provide a convenient and methodical way to deal with the vectorial character of our problem. We apply our method to the case of a homogeneous waveguide with circular cross-section. This configuration approximates the vacuum chamber to be used at XFEL and Energy Recovery Linac (ERL) facilities. Our approach, however, is very general and may be applied to other geometries, e.g. to rectangular waveguides, which approximate vacuum chambers used at SR facilities.

7.1 Definition of setup and position of the problem

To fix ideas we focus our attention on the setup in Fig. 19. Electrons travel through the usual edge radiation setup, similarly as in Fig. 1(a). The difference is that now we account for the presence of a waveguide with typical cross-section dimension ρ along the straight section. Since electrons are bent away, one may assume that the vacuum chamber ends at the downstream bend position $z = L/2$. Our goal in this Section is to calculate the field dis-

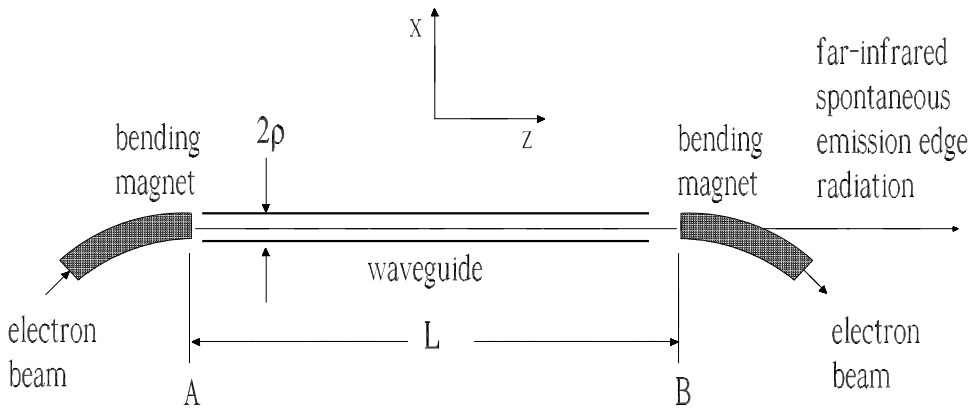

Fig. 19. Setup for edge radiation emission includes the presence of a waveguide with circular cross-section of radius ρ along the straight section.

tribution at that position, which should be subsequently propagated up to the experimental station.

Under the assumption $\delta \ll 1$, which is always considered valid, one can then extend the ER theory from unbounded space to the case when a waveguide is present. In unbounded space, the assumption $\delta \ll 1$ allowed us to apply the ER theory with given constraints on the angular region of observation: in fact, at large angles the SR contributions from bends is dominant compared to the ER contribution to the field. In other words, as we have seen, ER is a more collimated form of radiation, compared to bending magnet radiation. The presence of a waveguide seems at first glance to radically modify this viewpoint, because both SR from bends and ER is collected and guided into the vacuum chamber. However, we will see that this situation still carries a strong analogy with the unbounded space case: while in unbounded space ER theory can be applied within a given angular region dependent on δ, in the waveguide case ER theory can be applied within a given wave-number range dependent on δ. As said above, after the field distribution is calculated at $z = L/2$, it has to be propagated up to the experimental station. Radiation will be collected within a finite acceptance angle. This finite acceptance can be seen as a low-pass filter for spatial frequencies. If the acceptance angle is small enough (and this depends on the value of δ) only spatial frequencies where ER is dominant will be accepted. Thus, one can conclude that both in the case of unbounded space and vacuum chamber, ER theory can be applied with given constraints on the acceptance angle of the setup.

Despite the fact that equations for the edge radiation source are significantly complicated by the presence of a waveguide, we find that these complications result in the appearance of a single dimensionless extra-parameter,

namely the waveguide diffraction parameter $\Omega = \rho^2/(\lambda\!\!\!^{-} L)$. When $\phi \ll 1$ and $\delta \ll 1$, Ω is the only parameter of the problem and has a simple interpretation as the ratio between the waveguide cross-section area and the square of the radiation diffraction size of the ER virtual source located in the middle of the straight section in unbounded space.

The general theoretical framework of our extended ER theory relies on the solution of Maxwell's equations with modified boundary conditions, and follows closely the approach proposed in [32]. We wish to describe, in the space-frequency domain, radiation from an ultrarelativistic electron moving on a given trajectory inside a metallic vacuum chamber of arbitrary cross-section, homogeneous along the z-axis. An example is depicted in Fig. 20, where $\vec{n}$ is a vector field defined on the boundary surface S, such that $|\vec{n}| = 1$. At any point, $\vec{n}$ is orthogonal to S and points outwards and at this stage the waveguide cross-section is still considered arbitrary.

Since the electron is ultrarelativistic, the Lorentz factor γ obeys $1/\gamma^2 \ll 1$, and paraxial Maxwell's equations can be used in unbounded space. The presence of a waveguide introduces the extra-limitation $\lambda\!\!\!^{-} \ll \rho$. Paraxial approximation can be used under these two constraints. Then, the field equations read

$$\begin{cases} \left(\nabla_\perp{}^2 \vec{\vec{E}} + \frac{2i\omega}{c}\partial_z \vec{\vec{E}}\right) = \frac{4\pi e}{c} \exp\left[i\int_0^z d\bar{z} \frac{\omega}{2\gamma_z^2(\bar{z})c}\right]\left[\frac{i\omega}{c^2}\vec{v}_\perp(z) - \vec{\nabla}_\perp\right]\delta\left(\vec{r} - \vec{r}_0(z)\right) \\ \left(\vec{n}\times\vec{\vec{E}}\right)\Big|_S = 0 \\ \left(\vec{\nabla}_\perp \cdot \vec{\vec{E}}\right)\Big|_S = 0\,, \end{cases} \tag{73}$$

where the second and the third equation define boundary conditions at the waveguide surface S.

As has been demonstrated in [33, 34, 32] the field $\vec{\vec{E}}$ can be written in terms of cartesian components as (compare with Eq. (11))

$$\widetilde{E}^\alpha = \frac{4\pi e}{c}\int_{-\infty}^{z} dz' \left\{\frac{i\omega}{c^2} v_\perp^\beta(z') G_\beta^\alpha\left(\vec{r}, \vec{r}_0(z'), z - z'\right) + \left[\partial'_\beta G_\beta^\alpha\left(\vec{r}, \vec{r}', z - z'\right)\right]_{\vec{r}'=\vec{r}_0(z')}\right\} \times \exp\left[\frac{i\omega}{2c}\int_0^{z'} \frac{d\bar{z}}{\gamma_z^2(\bar{z})}\right], \tag{74}$$

where derivatives ∂'_β are taken with respect to $\vec{r}'$, and $-\infty$ has to be taken as the point where the source harmonics begin to exist (in our case, at

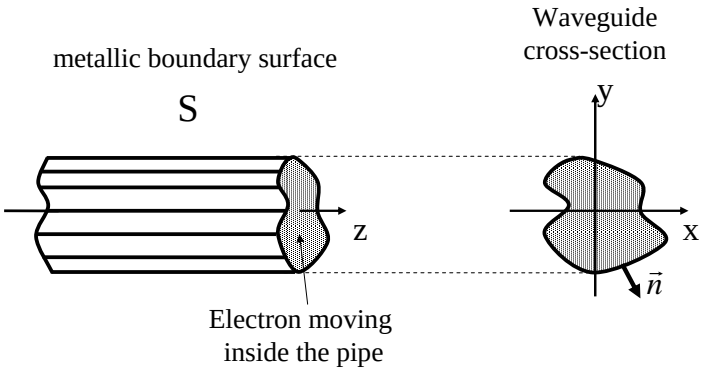

Fig. 20. Geometry of the problem. The electron is moving inside the vacuum chamber.

$z = -L/2$). Eq. (74) is the solution of the inhomogeneous field equation, describing the field from a single electron. As before, $\vec{r}_0(z')$ and $\vec{v}_\perp(z')$ fix transverse position and velocity of the electron as a function of z', and $\gamma_z(\bar{z}) = [1 - v_z(\bar{z})^2/c^2]^{-1/2}$, v_z indicating the longitudinal velocity of the electron. Finally, G^α_β are the cartesian components of a suitable tensorial Green's function for a homogeneous waveguide (along the z-axis):

$$
\begin{aligned}
G\left(\vec{r},\vec{r'},z,z'\right) = \frac{c}{2i\omega}\sum_j \Bigg\{ \exp\left[-\frac{ic\lambda_j^{\mathrm{TE}}}{2\omega}(z-z')\right]\left[\vec{e}_x\,\partial_y\,\psi_j^{\mathrm{TE}}(\vec{r}) - \vec{e}_y\,\partial_x\psi_j^{\mathrm{TE}}(\vec{r})\right] \\
\otimes\left[\vec{e}_x\,\partial_{y'}\psi_j^{\mathrm{TE}}\left(\vec{r'}\right) - \vec{e}_y\,\partial_{x'}\psi_j^{\mathrm{TE}}\left(\vec{r'}\right)\right]\Bigg\} \\
+\frac{c}{2i\omega}\sum_j \Bigg\{ \exp\left[-\frac{ic\lambda_j^{\mathrm{TM}}}{2\omega}(z-z')\right]\left[\vec{e}_x\,\partial_x\psi_j^{\mathrm{TM}}(\vec{r}) + \vec{e}_y\,\partial_y\,\psi_j^{\mathrm{TM}}(\vec{r})\right] \\
\otimes\left[\vec{e}_x\,\partial_{x'}\psi_j^{\mathrm{TM}}\left(\vec{r'}\right) + \vec{e}_y\,\partial_{y'}\psi_j^{\mathrm{TM}}\left(\vec{r'}\right)\right]\Bigg\}, \qquad (75)
\end{aligned}
$$

where notation $\otimes$ indicates the tensor product. Here, $\vec{e}_x$ and $\vec{e}_y$ are unit vectors along cartesian axes x and y, while $\psi_j^{\mathrm{TE,TM}}$ and $\lambda_j^{\mathrm{TE,TM}}$ are eigenfunctions and eigenvalues referring to the scalar problem:

$$
\begin{cases}
\nabla^2_\perp\psi_j^{\mathrm{TE,TM}}(\vec{r}) + \lambda_j^{\mathrm{TE,TM}}\,\psi_j^{\mathrm{TE,TM}}(\vec{r}) = 0 \\
\vec{n}\cdot\left(\vec{\nabla}_\perp\psi_j^{\mathrm{TE}}\right)\Big|_s = 0 \\
\left(\psi_j^{\mathrm{TM}}\right)\Big|_s = 0\,,
\end{cases} \qquad (76)
$$

TE and TM respectively standing for Transverse Electric and Transverse

Magnetic, with normalization condition

$$\int_s d\vec{r} \left| \vec{\nabla} \psi_j^{\mathrm{TE,TM}} \right|^2 = 1 \, . \tag{77}$$

Note that here we derived the Green's function Eq. (75) directly in paraxial approximation starting from Eq. (73) for the transverse components of the field.

Simplifications to Eq. (74) apply remembering that in our case $\vec{v}_\perp(z') = 0$ and $\vec{r}_0(z') = 0$. Setting $z = L/2$ one obtains:

$$\widetilde{E}^\alpha = \frac{4\pi e}{c} \int_{-L/2}^{L/2} dz' \left[\partial'_\beta G_\beta^\alpha \left(\vec{r}, \vec{r'}, z - z' \right) \right]_{\vec{r'}=0} \exp\left[\frac{i\omega z'}{2c\gamma^2} \right] \, . \tag{78}$$

In a waveguide that is homogenous along the z-axis, only TM modes turn out to be driven by the uniform motion of the space-charge distribution. As a result, we can focus on TM modes only. This may be directly seen by calculating $\partial'_\beta G_\beta^\alpha$. A compact mathematical way proving this fact without cumbersome calculations is to note that TE modes appear in the expression for the tensorial Green's function, Eq. (75), through the combination $\vec{\nabla} \times (\psi_j^{\mathrm{TE}} \vec{e}_z) = \vec{e}_x \, \partial_y \, \psi_j^{\mathrm{TE}} - \vec{e}_y \, \partial_x \psi_j^{\mathrm{TE}}$. Then, TE modes contribute in $\partial'_\beta \, G_\beta^\alpha$ for $\vec{\nabla} \cdot [\vec{\nabla} \times (\psi_j^{\mathrm{TE}} \vec{e}_z)]$, which is the divergence of a curl and yields back zero. From a physical viewpoint this is a sound result. In fact, radiation is related with energy change of the particle, which happens through the scalar product $\vec{\widetilde{E}} \cdot \vec{v}$. Since $\vec{v}_\perp(z') = 0$, TE modes cannot lead to any energy change of the electron. As a result, they are not excited. Note that $\vec{v}_\perp(z') = 0$ means that $\vec{r}_0(z')$ = constant. Since the electron beam trajectory should be centered, one recovers $\vec{r}_0(z') = 0$, leading to extra-simplifications in Eq. (78).

7.2 Theory of Edge Radiation in a circular waveguide

We now want to apply Eq. (78) to study the case of the setup in Fig. 19 in the presence of a circular waveguide with radius ρ. Therefore, we fix $z = L/2$ in Eq. (78). This allows us to calculate a field distribution at the end of the straight section, which acts as a source to be used for further propagation in unbounded space or through the beamline optics.

In order to explicitly compute the tensor Green's function in Eq. (75) we need to solve the problem in (76) with this particular choice of geometry.

Because of the particular symmetry in the case of a circular waveguide, it is convenient to use transverse polar coordinates so that $\vec{r}$ is identified by radial distance $r = \sqrt{x^2 + y^2}$ and angle $\varphi = \arctan(y/x)$.

Solutions of the equation set in (76) are

$$\psi^{\mathrm{TM}}_{mk1} = A^{\mathrm{TM}}_{mk} J_m(\nu_{mk} r)\sin(m\phi)\,, \qquad \psi^{\mathrm{TM}}_{mk2} = A^{\mathrm{TM}}_{mk} J_m(\nu_{mk} r)\cos(m\phi)\,, \tag{79}$$

where ν_{mk} are defined as the roots of $J_m(\nu_{mk}) = 0$, and the normalization coefficients for TM modes, A^{TM}_{mk}, are given by

$$A^{\mathrm{TM}}_{mk} = \sqrt{\frac{a_m}{\pi}} \frac{1}{\nu_{mk}\, J_{m-1}(\nu_{mk})}\,, \tag{80}$$

where $a_0 = 1$ and $a_m = 2$ for $m \geq 1$.

This leads to the following final result for the tensor Green's function components in cartesian coordinates:

$$\begin{aligned}
G\left(\vec{r},\vec{r'},z-z'\right) = {} & \frac{c}{2i\omega}\sum_{m=0}^{\infty}\sum_{k=1}^{\infty}\left(A^{TM}_{mk}\right)^2\left(\frac{\nu_{mk}}{2\rho}\right)^2 \exp\left[-\frac{ic(z-z')}{2\omega\rho^2}\nu^2_{mk}\right] \\
& \times\left\{\begin{pmatrix} J_{m-1}(\nu_{mk}r/\rho)\sin[(m-1)\varphi] - J_{m+1}(\nu_{mk}r/\rho)\sin[(m+1)\varphi] \\ J_{m-1}(\nu_{mk}r/\rho)\cos[(m-1)\varphi] + J_{m+1}(\nu_{mk}r/\rho)\cos[(m+1)\varphi] \end{pmatrix}\right. \\
& \otimes\begin{pmatrix} J_{m-1}(\nu_{mk}r'/\rho)\sin[(m-1)\varphi'] - J_{m+1}(\nu_{mk}r'/\rho)\sin[(m+1)\varphi'] \\ J_{m-1}(\nu_{mk}r'/\rho)\cos[(m-1)\varphi'] + J_{m+1}(\nu_{mk}r'/\rho)\cos[(m+1)\varphi'] \end{pmatrix} \\
& + \begin{pmatrix} J_{m-1}(\nu_{mk}r/\rho)\cos[(m-1)\varphi] - J_{m+1}(\nu_{mk}r/\rho)\cos[(m+1)\varphi] \\ -J_{m-1}(\nu_{mk}r/\rho)\sin[(m-1)\varphi] - J_{m+1}(\nu_{mk}r/\rho)\sin[(m+1)\varphi] \end{pmatrix} \\
& \left.\otimes\begin{pmatrix} J_{m-1}(\nu_{mk}r'/\rho)\cos[(m-1)\varphi'] - J_{m+1}(\nu_{mk}r'/\rho)\cos[(m+1)\varphi'] \\ -J_{m-1}(\nu_{mk}r'/\rho)\sin[(m-1)\varphi'] - J_{m+1}(\nu_{mk}r'/\rho)\sin[(m+1)\varphi'] \end{pmatrix}\right\}\,,
\end{aligned} \tag{81}$$

where we already dropped TE modes. Eq. (81) is valid in the case of a circular waveguide. These facts are demonstrated in [32]. As a result we have

$$\begin{aligned}
\partial'_\beta\, G^1_\beta = {} & -\frac{c}{4i\omega}\sum_{m=0}^{\infty}\sum_{k=1}^{\infty}\left(A^{TM}_{mk}\right)^2\left(\frac{\nu_{mk}}{\rho}\right)^3 \exp\left[-\frac{ic(z-z')}{2\omega\rho^2}\nu^2_{mk}\right] J_m\left(\frac{\nu_{mk}r'}{\rho}\right) \\
& \times\left\{\left[J_{m-1}\left(\frac{\nu_{mk}r}{\rho}\right)\sin[(m-1)\varphi] - J_{m+1}\left(\frac{\nu_{mk}r}{\rho}\right)\sin[(m+1)\varphi]\right]\sin(m\varphi')\right.
\end{aligned}$$

$$+\left[J_{m-1}\left(\frac{\nu_{mk}r}{\rho}\right)\cos[(m-1)\varphi]-J_{m+1}\left(\frac{\nu_{mk}r}{\rho}\right)\cos[(m+1)\varphi]\right]\cos(m\varphi')\Bigg\} \tag{82}$$

along $\vec{e}_x$ and

$$\partial'_\beta\, G^2_\beta = -\frac{c}{4i\omega}\sum_{m=0}^{\infty}\sum_{k=1}^{\infty}\left(A^{TM}_{mk}\right)^2\left(\frac{\nu_{mk}}{\rho}\right)^3\exp\left[-\frac{ic(z-z')}{2\omega\rho^2}\nu^2_{mk}\right]J_m\left(\frac{\nu_{mk}r'}{\rho}\right)$$
$$\times\Bigg\{\left[J_{m-1}\left(\frac{\nu_{mk}r}{\rho}\right)\cos[(m-1)\varphi]+J_{m+1}\left(\frac{\nu_{mk}r}{\rho}\right)\cos[(m+1)\varphi]\right]\sin(m\varphi')$$
$$-\left[J_{m-1}\left(\frac{\nu_{mk}r}{\rho}\right)\sin[(m-1)\varphi]+J_{m+1}\left(\frac{\nu_{mk}r}{\rho}\right)\sin[(m+1)\varphi]\right]\cos(m\varphi')\Bigg\} \tag{83}$$

along $\vec{e}_y$. A major simplification arises since $\vec{r}_0(z') = 0$. Because of this, the only non-zero contribution to Eq. (82) and Eq. (83) is for $m = 0$, otherwise $J_m(\nu_{mk}r'/\rho)$ yields zero.

Substitution in Eq. (78) yields, therefore, the following result for the field at $z = L/2$:

$$\vec{\vec{E}} = -2ie\sqrt{\frac{\omega}{Lc^3}}\sum_{k=1}^{\infty}\mathcal{A}^{\nu}_k\left(\frac{L}{2}\right)J_1\left(\frac{\nu_{0k}r}{\rho}\right)\vec{e}_r \tag{84}$$

where

$$\mathcal{A}^{\nu}_k(L/2) = \sqrt{\left(\frac{Lc}{\omega}\right)^3}\frac{\nu_{0k}\exp\left[-iC^{\nu}_kL/2\right]}{\rho^3J^2_1(\nu_{0k})}\mathrm{sinc}\left[\frac{L}{2}C^{\nu}_k+\frac{\phi}{4}\right]. \tag{85}$$

Here we defined $C^{\nu}_k = \nu^2_{0k}c/(2\omega\rho^2)$ and $\vec{e}_r = \sin(\varphi)\vec{e}_x + \cos(\varphi)\vec{e}_y$. Eq. (84) and Eq. (85) solve the problem of characterization of ER in the setup of Fig. 19 for $\delta \ll 1$.

It is interesting to show that the treatment of edge radiation in terms of virtual sources has a straightforward generalization for the case of a waveguide.

It is convenient to introduce the subject by first noting that Eq. (73), the non-homogenous Maxwell's equation with boundary conditions at the waveguide walls, admits a self-reproducing solution. Because of the circular cross section of the waveguide, there is no preferential direction on the transverse plane. As a result, the transverse electric field must be radially polarized, and axially symmetric. We make the ansatz (i) $\vec{\vec{E}} = E_r(r)E_z(z)\vec{e}_r$, and (ii)

$E_z(z) = \exp[iz/(2\gamma^2 \lambda\!\!\!^{-})]$. Note that (i) is already equivalent to postulating a self-reproducing field, meaning that the transverse shape of the field is independent of the longitudinal coordinate z down the waveguide. Substituting (i) and (ii) in Eq. (73) and shifting to polar coordinates we obtain the following problem for $E_r(\tilde{r})$:

$$\begin{aligned} &\tilde{r}\frac{d^2E_r}{d\tilde{r}^2} + \frac{dE_r}{d\tilde{r}} - \left(\tilde{r} + \frac{1}{\tilde{r}}\right)E_r = \frac{4\omega e}{c^2\gamma}\tilde{r}\frac{d}{d\tilde{r}}\left[\frac{\delta(\tilde{r})}{\tilde{r}}\right] , \\ &\frac{d}{d\tilde{r}}\left(\tilde{r}E_r\right)_{|_{\tilde{r}=\tilde{\rho}}} = 0 , \end{aligned} \tag{86}$$

where we introduced $\tilde{r} = r/(\gamma\lambda\!\!\!^{-})$ and $\tilde{\rho} = \rho/(\gamma\lambda\!\!\!^{-})$ ad hoc to simplify notations in Eq. (86). Solution of Eq. (86) yields the final result

$$\vec{\tilde{E}}_{\text{s-rep}} = -\frac{2\omega e}{c^2\gamma}\exp\left[\frac{i\omega z}{2c\gamma^2}\right]\vec{e}_r\left[K_1\left(\frac{\omega r}{c\gamma}\right) + \frac{K_0\left(\frac{\omega\rho}{c\gamma}\right)}{I_0\left(\frac{\omega\rho}{c\gamma}\right)}I_1\left(\frac{\omega r}{c\gamma}\right)\right] . \tag{87}$$

Eq. (87) is well-known (see, e.g. [35]), and explicitly describes the self-reproducing nature of the field, because the transverse structure of the radiation field is fixed at any value z.

At each longitudinal coordinate z_i, the radiation field can be expanded in a series of modes of the passive (empty) waveguide. Although we have not calculated explicitly the coefficients in this expansion, these are independent of z, as $z = z_i$ has been fixed. This leads to a paradox. In fact, one can propagate each waveguide mode till another coordinate z_f. However, each mode of the passive waveguide has its own phase velocity. Therefore, one will not recover Eq. (87) at position z_f, because relative phases of modes have changed, at that position. The paradox is solved noting that the field in Eq. (87) represents a result for an active (loaded) waveguide. In other words, to obtain back Eq. (87), one should add to the propagated field, the additional field radiated by the electron beam between the points z_i and z_f, which is nothing but the edge radiation contribution from the setup in Fig. (19) with $A = z_i$ and $B = z_f$. In other words, in order to recover the self-reproducing field structure, we should add to the right hand side of the propagation equation

$$\widetilde{E}^{\alpha}(z_f, \vec{r}_f) = -\frac{2i\omega}{c}\int d\vec{r'}\widetilde{E}^{\alpha}(z_i, \vec{r'})G^{\alpha}_{\beta}(\vec{r}_f, \vec{r'}, z_f - z_i) , \tag{88}$$

where G is given in Eq. (81). Note that Eq. (88) generalizes Eq. (14). It follows that

$$\widetilde{E}^{\alpha}_{\mathrm{s-rep}}(z_f,\vec{r}_f) = -\frac{2i\omega}{c}\int d\vec{r'}\widetilde{E}^{\alpha}_{\mathrm{s-rep}}(z_i,\vec{r'})G^{\alpha}_{\beta}(\vec{r}_f,\vec{r'},z_f-z_i)$$
$$+\frac{4\pi e}{c}\int_{z_i}^{z_f} dz'\left[\partial'_{\beta}G^{\alpha}_{\beta}(\vec{r}_f,\vec{r'},z_f-z')\right]_{\vec{r'}=0}\exp\left[\frac{i\omega z'}{2c\gamma^2}\right]. \qquad (89)$$

Note that the second term on the right hand side of Eq. (89) is nothing but the edge radiation contribution from z_i to z_f (for $z_i = -L/2$ and $z_f = L/2$ one may compare with Eq. (78)). Eq. (89) can be rewritten as

$$\vec{\widetilde{E}}_{\mathrm{ER}}(L/2,\vec{r}) = \frac{4\pi e}{c}\int_{z_i}^{z_f} dz'\left[\partial'_{\beta}G^{\alpha}_{\beta}(\vec{r}_f,\vec{r'},z_f-z')\right]_{\vec{r'}=0}\exp\left[\frac{i\omega z'}{2c\gamma^2}\right]$$
$$= \widetilde{E}^{\alpha}_{s2,\vec{r}}(L/2) - \frac{2i\omega}{c}\int d\vec{r'}\widetilde{E}^{\alpha}_{s1}(-L/2,\vec{r'})G^{\alpha}_{\beta}(\vec{r},\vec{r'},L)\,, \qquad (90)$$

where we defined $\vec{\widetilde{E}}_{s1}(-L/2) = -\vec{\widetilde{E}}_{\mathrm{s-rep}}(-L/2)$ and $\vec{\widetilde{E}}_{s2}(L/2) = \vec{\widetilde{E}}_{\mathrm{s-rep}}(L/2)$. Having introduced this notation we are in the position to see that the treatment of edge radiation in terms of virtual sources has a straightforward generalization for the case of a waveguide. In fact, Eq. (90) means that the edge radiation field can be interpreted as the sum of a given field distribution $\widetilde{E}^{\alpha}_{s2,\vec{r}}(L/2)$ at $z = L/2$ plus the field obtained propagating another field distribution, $\widetilde{E}^{\alpha}_{s1}(-L/2,\vec{r'})$, from $z = -L/2$ up to $z = L/2$ according to Eq. (88). We thus straightforwardly interpret $\vec{\widetilde{E}}_{s1,s2}$ as the generalized virtual sources at $z = -L/2$ and $z = L/2$ respectively. Note that in the limit for $\rho \longrightarrow \infty$, the self-reproducing field solution in Eq. (87) is related to the virtual source fields in Eq. (39) consistently with what has just been stated.

Also note that Eq. (90) and Eq. (84) present the same field, and must coincide. This hints to the fact that the sum in Eq. (84) can be calculated analytically. Since the use of virtual sources provides conceptual insight and should facilitate the design of ER setups, it is instructive to explicitly demonstrate the equivalence of Eq. (90) and Eq. (84). This is demonstrated in Appendix A.

7.3 Analysis of results (exemplifications)

We now analyze our main results, Eq. (84) and Eq. (85). To this purpose, it is convenient to re-write these equations in normalized units, so that:

$$\vec{\hat{E}} = -2i \sum_{k=1}^{\infty} \mathcal{A}_k^{\nu}(\hat{z}) J_1\left(\frac{\nu_{0k}\hat{r}}{\sqrt{\Omega}}\right)\vec{e}_r \tag{91}$$

with

$$\mathcal{A}_k^{\nu}(\hat{z}) = \frac{\nu_{0k}\exp[-i\hat{C}_k^{\nu}\hat{z}]}{\Omega^{3/2}J_1^2(\nu_{0k})}\mathrm{sinc}\left[\frac{1}{2}\hat{C}_k^{\nu} + \frac{\phi}{4}\right], \tag{92}$$

where we defined $\hat{C}_k^{\nu} = C_k^{\nu}L = \nu_{0k}^2/(2\Omega)$, we reminded $\Omega = \rho^2/(\lambda\!\!\!^{-}L)$, and normalized quantities $\vec{\hat{E}}$, $\hat{r}$ and $\hat{z}$ are defined as in unbounded space.

Note that, with reference to Fig. 19, we are assuming $\hat{z} < 1/2$, because for $\hat{z} > 1/2$ we are already in unbounded space. Using the Green's function G_{β}^{α} we can formally propagate the field at $\hat{z} = 1/2$, i.e. Eq. (84), up to positions $\hat{z} < 1/2$. Note that, since Eq. (84) is presented as a sum of empty-waveguide modes, this propagation just modifies the exponential (phase) factor, so that instead of $\exp[-i\hat{C}_k^{\nu}/2]$ we find $\exp[-i\hat{C}_k^{\nu}\hat{z}]$ in Eq. (91). Then, Eq. (91) assumes the meaning of a virtual field distribution in analogy with the unbounded-space case.

Also note that the sinc(·) function in the expression for $\mathcal{A}_k^{\nu}$ is a direct consequence of our model of the setup of sharp-edges at positions $\hat{z} = -1/2$ and $\hat{z} = 1/2$ respectively. In fact, the sinc(·) function is the Fourier transform of a rectangular function with respect to $\hat{C}_k^{\nu} + \phi/2$, modelling the sharp switch on and switch off of the bunch harmonics. The presence of high frequency components in the rectangular function implies the presence of contributions with high values of k. In its turn, each contribution with large value of k in Eq. (91) can be interpreted as a superposition of plane waves propagating at angles $\nu_{0k}/\sqrt{\Omega}$ in units of the diffraction angle $\sqrt{\lambda\!\!\!^{-}/L}$. Thus, higher values of k correspond to the introduction of high spatial frequency components in the field.

However, we should account for the fact that our theory applies with a finite accuracy related to the value of the parameter δ. When using this approximation we neglect contributions to the field with an accuracy related with δ. This means that, in the analysis of our results, it does not make sense to consider high spatial frequency contributions due to abrupt switching of the bending magnet fields on a scale shorter than $\sqrt[3]{R^2\lambda\!\!\!^{-}}$, because these are outside of the accuracy of the sharp-edge approximation. We may then introduce a spatial frequency filter in our expression for the field by replacing Eq. (78) with

$$\widetilde{E}^{\alpha} = \frac{4\pi e}{c} \int_{-\infty}^{z} dz' S(z') \left[\partial'_{\beta} G^{\alpha}_{\beta}(\vec{r}, \vec{r'}, z - z') \right]_{\vec{r'}=0} \exp\left[\frac{i\omega z'}{2c\gamma^2} \right] , \tag{93}$$

where the function $S(z')$ introduces some smoothing of the rectangular profile on a scale $\sqrt[3]{R^2 \lambda}$. In normalized units Eq. (93) reads

$$\hat{E}^{\alpha} = 4\pi \int_{-\infty}^{\hat{z}} d\hat{z}' S(\hat{z}') \left[\partial'_{\beta} \hat{G}^{\alpha}_{\beta} \left(\vec{\hat{r}}, \vec{\hat{r}'}, \hat{z} - \hat{z}' \right) \right]_{|_{\vec{\hat{r}'}=0}} \exp\left[\frac{i\phi \hat{z}'}{2} \right] , \tag{94}$$

where derivatives are now calculated with respect to normalized quantities.

We model $S(\hat{z}')$ as a constant function along the straight section length with exponentially decaying edges [5] on a typical (normalized) distance Δ:

$$S(\hat{z}') = \begin{cases} \exp\left[-(\hat{z}' + 1/2)^2 / (2\Delta^2) \right] & \text{for } \hat{z}' < -1/2 \\ 1 & \text{for } -1/2 < \hat{z}' < 1/2 \\ \exp\left[-(\hat{z}' - 1/2)^2 / (2\Delta^2) \right] & \text{for } \hat{z}' > 1/2 \end{cases} . \tag{95}$$

It follows that Eq. (92) should be replaced by

$$\mathcal{A}^{\nu}_{k}(\hat{z}) = \frac{\nu_{0k} \exp[-i\hat{C}^{\nu}_{k}\hat{z}]}{\Omega^{3/2} J_1^2(\nu_{0k})} \mathcal{F}\left\{ S(\hat{z}'), \left(\hat{C}^{\nu}_{k} + \phi/2 \right) \right\} , \tag{96}$$

where $\mathcal{F}\{S(\hat{z}'), (\hat{C}^{\mu,\nu}_{k} + \phi/2)\}$ is the Fourier transform of the function S with respect to $(\hat{C}^{\mu,\nu}_{k} + \phi/2)$. The introduction of the function $S(\hat{z}')$ introduces a suppression of higher frequency components of $\mathcal{F}\{S\}$, and corresponds to a suppression of higher spatial frequencies in the field distribution, i.e. to a smoother field distribution. For a fixed value of Ω and $\hat{z}$ we qualitatively expect finite and smooth field distribution for finite values of Δ. On the contrary, in the sharp-edge limit for $\Delta \longrightarrow 0$, the field must diverge for some value of $\hat{r}$, as a result of the already discussed divergence of the integrated flux and of the fact that the radius of the vacuum chamber is finite. Note that the level of high spatial frequencies depends in a complicated way on Ω, because the perfectly metallic waveguide effectively acts as a mirror. The

[5] Formally, such model is in contrast with the previous statement that for $\hat{z} > 1/2$ we are in unbounded space. However, we introduce Δ to account for a finite accuracy of the sharp-edge approximation. Thus, it does not make sense to specify where the unbounded space begins within a distance Δ.

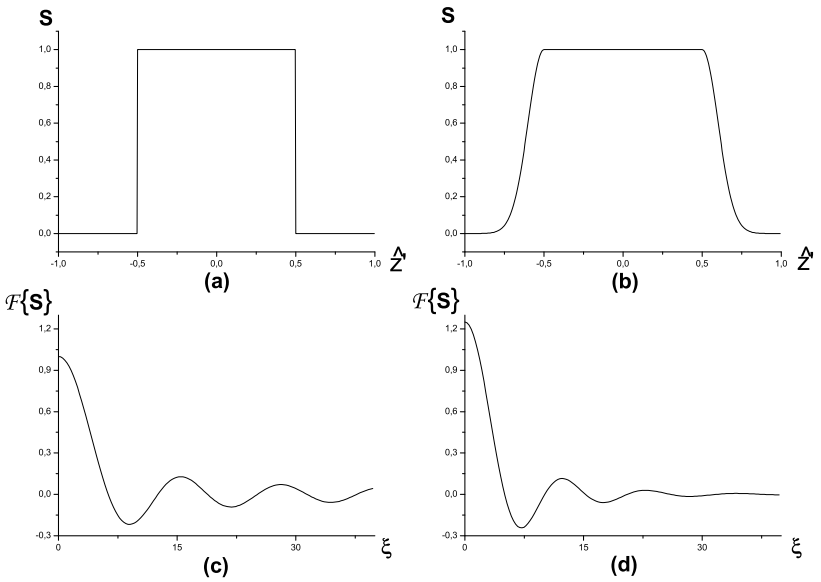

Fig. 21. Comparison between hard-edge case and high-frequency filtering. Function $S(\hat{z}')$ in the hard-edge case with $\Delta = 0$ (a) and in the case when filtering is applied with $\Delta = 0.1$ (b). Their Fourier transforms $\mathcal{F}\{S\}$ with respect to $\xi = \hat{C}_k^{\mu,\nu} + \hat{C} > 0$ are plotted in (c) for the hard edge case and in (d) when filtering is present.

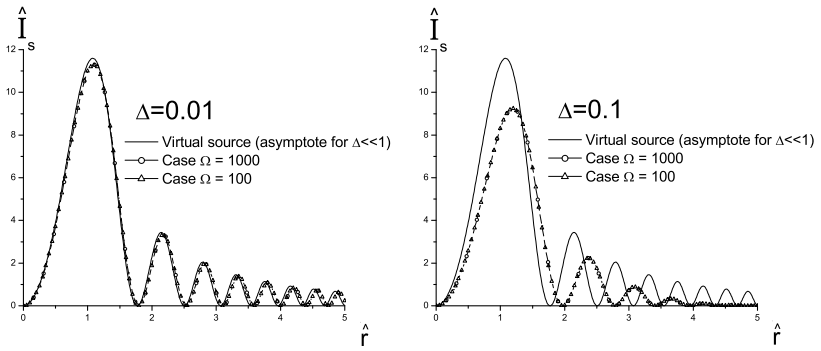

Fig. 22. Intensity profiles of the virtual source ($\hat{z} = 0$) at large values of $\Omega = R^2/(\lambda L_w)$ for different values of Δ in the limit for $\hat{\phi} \ll 1$. These plots are obtained from Eq. (91) and Eq. (96), while the asymptotic limit for $\Delta \ll 1$ is found with the help of Eq. (31).

value of Δ should be actually chosen to cut off high spatial frequencies that are outside the region of applicability of the sharp-edge approximation, i.e. $\Delta \sim \delta$. Thus, the correct value of Δ depends, case by case, on the type of setup considered. The Fourier transform of the function $S(\hat{z}')$ in Eq. (95) to be inserted into Eq. (96) reads

$$\mathcal{F}\left\{S(\hat{z}'),\left(\hat{C}_k^{\nu,\mu}+\frac{\phi}{2}\right)\right\}=\operatorname{sinc}\left[\frac{\hat{C}_k^{\nu,\mu}}{2}+\frac{\phi}{4}\right]+\sqrt{2\pi}\,\Delta\exp\left[-\frac{\Delta^2}{2}\left(\hat{C}_k^{\nu,\mu}+\frac{\phi}{2}\right)^2\right]$$
$$\times\left\{\cos\left[\frac{\hat{C}_k^{\nu,\mu}}{2}+\frac{\phi}{4}\right]-\sin\left[\frac{\hat{C}_k^{\nu,\mu}}{2}+\frac{\phi}{4}\right]\operatorname{erfi}\left[\frac{\Delta}{\sqrt{2}}\left(\hat{C}_k^{\nu,\mu}+\frac{\phi}{2}\right)\right]\right\}\,, \tag{97}$$

where the imaginary error function erfi(·) is defined as

$$\operatorname{erfi}(z)=\frac{1}{i}\operatorname{erf}(iz)=\frac{2}{i\sqrt{\pi}}\int_0^{iz}\exp\left[-t^2\right]dt\,. \tag{98}$$

Fig. 21 presents a comparison between functions S and $\mathcal{F}\{S\}$ for $\Delta = 0.1$ and $\Delta = 0$. A filtering effect can be clearly seen, suppressing higher frequency components of $\mathcal{F}\{S\}$.

Eq. (91) and Eq. (92) completely describe ER in the presence of a circular waveguide. Position $\hat{z} = 0$ corresponds to the single virtual source description discussed before. In fact, as we have seen, the concept of laser-like radiation beam can be naturally extended to the case a waveguide is present. As said before one must carefully select the number of modes used for computation, according to $k \gg \sqrt{\Omega}$.

We further consider, as an example, the limit for $\phi \ll 1$. In Fig. 22 we show a comparison between the analytic expression for the intensity distribution $\hat{I}$ at the virtual source position, and numerical expressions obtained through Eq. (91) for different values of Δ at $\Omega = 1000$ and $\Omega = 100$. Differences between results for $\Delta = 0.1$ and Eq. (31) should be taken as exemplification of the filtering process. A three-dimensional view of the intensity profile of the virtual source for $\Omega = 5$ and $\Delta = 0.1$ is shown in Fig. 23, to be compared with Fig. 9 for the unbounded-space limit. The number of modes used in all plots are in all cases much larger than $\sqrt{\Omega}$. Furthermore, we verified that results do not change by changing the number of modes used in the computation, provided that condition $k_{\max} \gg \sqrt{\Omega}$ is fulfilled. We also checked that the same results obtained with the help of Eq. (91) can also be recovered by introducing apodization directly in Eq. (19). This confirms that numerical evaluation of Eq. (91) is sound.

The behavior of the intensity profile at the virtual source when waveguide effects are important is shown in Fig. 24 for different values of Ω at $\Delta = 0.01$ $\Delta = 0.1$. Further on, in Fig. 25 we plot the intensity distribution $\hat{I} = |\hat{E}|^2$ as a function of the reduced radius $\hat{r}$ for the same values of Δ and Ω at $\hat{z} = 1/2$. All plots are evaluated with the help of Eq. (91). It should be remarked that

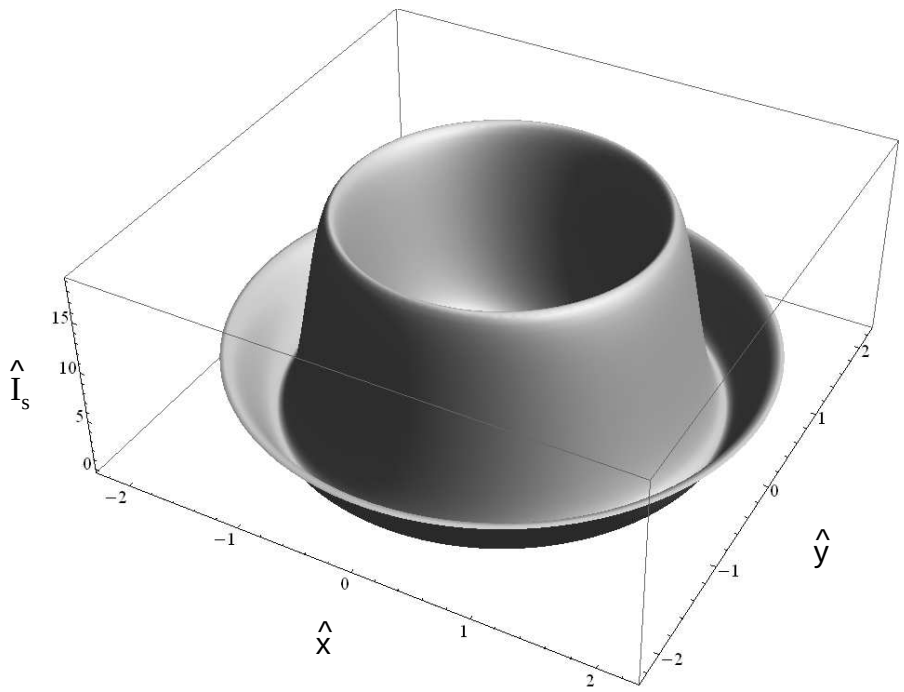

Fig. 23. Three-dimensional plot of the intensity profile of the virtual source ($\hat{z} = 0$) at $\Omega = R^2/(\lambda L_w) = 5$ for $\Delta = 0.1$ in the limit for $\hat{\phi} \ll 1$.

the wavefront at $\hat{z} = 1/2$ is not plane (as at $\hat{z} = 0$) and the phase distribution carries important information when one needs to propagate the field from $\hat{z} = 1/2$ to any other point. The derived analytical algorithm in Eq. (91) enables one to calculate all these informations.

Comparison of the cases for $\Delta = 0.01$ and $\Delta = 0.1$ clearly shows the effect of different edge dimensions, corresponding to filtering of high spatial frequencies. It should be reminded that when $\Delta = 0$ the angle-integrated spectral flux of ER is divergent in the unbounded space, as well as in a waveguide. Such divergency was motivated as an effect of the sharp-edge approximation, and depends logarithmically on Δ.

To sum up, knowledge of the field at $\hat{z} = 1/2$ fulfill our goal for this Section. Expression for the field at $\hat{z} = 1/2$ can be interpreted as a virtual-field distribution. From this viewpoint, the presence of a finite parameter Δ corresponds to the presence of an angular filter, related to the violation of ER expression for angles comparable with the bending magnet radiation angle. The virtual-field distribution at $\hat{z} = 1/2$ should be further propagated either in the unbounded space or through any other kind of vacuum chamber up to the experimental station. In other words, the knowledge of the field at the straight section exit constitutes the starting point for further propagation. Typically, a user-beamline vacuum chamber will be connected with the electron vacuum chamber (that follows the bending magnet after position

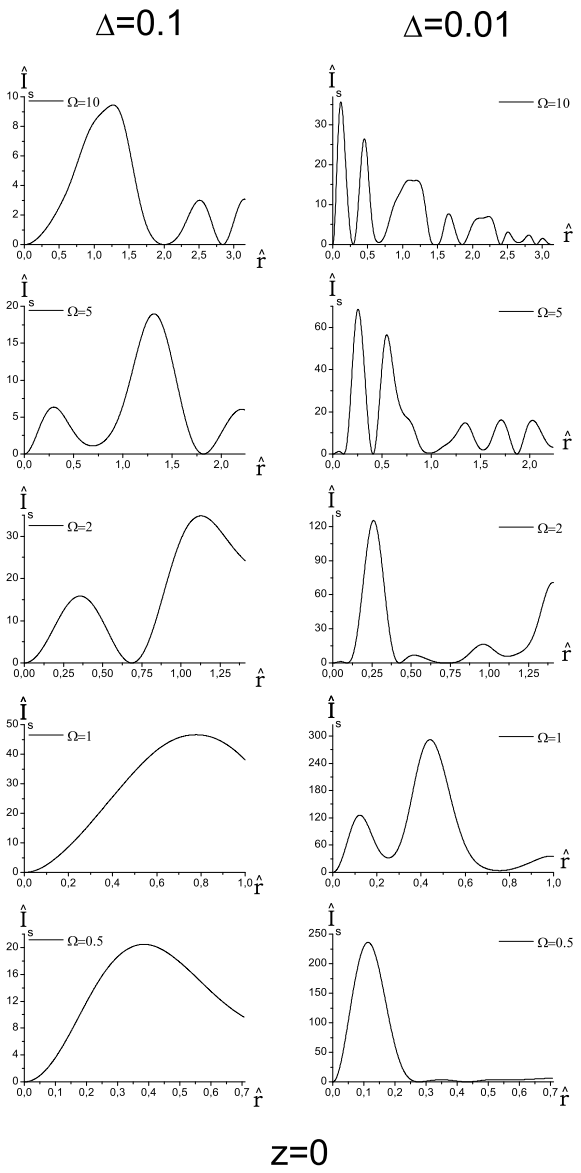

Fig. 24. Intensity profiles of the virtual source ($\hat{z} = 0$) at different values of $\Omega = R^2/(\lambda L_w)$ for $\hat{\phi} \ll 1$ at two values $\Delta = 0.1$ and $\Delta = 0.01$.

$\hat{z} = 1/2$). The user-beamline vacuum chamber has a typical characteristic size which is larger than the electron vacuum chamber. It follows that, after position $\hat{z} = 1/2$, the field can usually be propagated as in unbounded space.

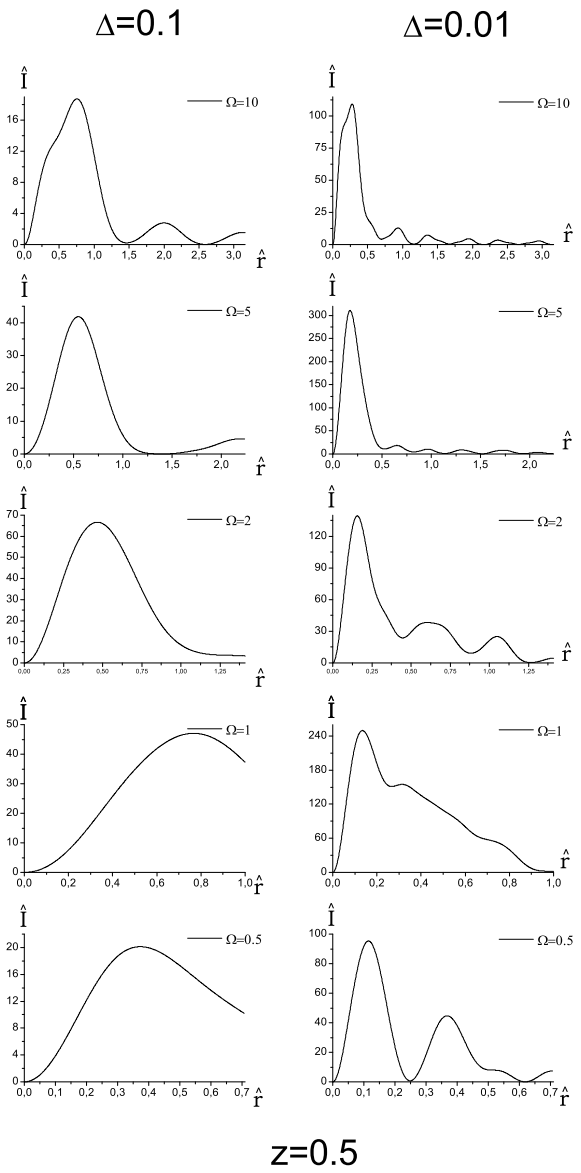

Fig. 25. Intensity profiles at $\hat{z} = 1/2$ at different values of $\Omega = R^2/(\lambda\!\!\!^{-} L_w)$ for $\hat{\phi} \ll 1$ at two values $\Delta = 0.1$ and $\Delta = 0.01$.

8 Coherent edge radiation

The physics of radiation processes from electron beams critically depends on the ratio of the bunch length to the wavelength of the emitted radiation. We can thus define two opposite asymptotes for the electron bunch length,

corresponding to very different characteristics of radiation.

In the first limit, when the electron bunch is long compared to the radiation wavelength, one deals with the conventional case of spontaneous radiation. In this regime the electron phases are not correlated, i.e. distances between electrons are randomly distributed on a characteristic scale much longer than the radiation wavelength. Incoherent superposition of each electron contribution to the radiation field yields low-power emission, proportional to the charge in the bunch, with the usual incoherent phase-noise statistics.

In the second limit, when the electron bunch is short compared to the radiation wavelength, one deals with the case of coherent radiation. Electron phases are correlated, in the sense that random variations of distances between electrons are distributed on a characteristic scale shorter than the radiation wavelength. The bunch essentially behaves as a single point-charge, which coherently emits high-power radiation. In this case, the radiation power scales quadratically with the total electric charge in the bunch, rather than linearly as in the other limit. It is because of this quadratic effect that the radiation power can be greatly enhanced, because the bunch population is usually of order 10^{10} particles.

Coherent radiation is usually not emitted in electron storage rings, because the bunch length is of order of a centimeter. However, in linear accelerators, much shorter electron bunches of the order of 100μm can be produced in magnetic bunch compressors. In this Section we will discuss the physics of coherent ER distinguishing two cases, when coherent emission is due to an overall temporal bunch profile shorter than the wavelength or to short structures (microbunches of order of the radiation wavelength) superimposed to the temporal profile of the bunch.

When it comes to the use of ER as a diagnostic tool, the availability of a much larger number of photons constitutes an important advantage of coherent ER compared to the incoherent case. By detecting coherent ER, characteristics of the electron bunch such as their three-dimensional distribution and divergence can be measured. Moreover, coherent radiation presents the unique feature that electron-beam microbunching can be investigated too.

8.1 Review of known methods

There are two equivalent approaches to describe coherent SR in general: a Lagrangian approach and a Eulerian approach.

In the Lagrangian approach particles are labelled with a given index, and the motion of individual charges is followed through space. One follows the

evolution of each particle as a function of energy deviation, angular direction, position and arrival time at a given reference (longitudinal) position. Knowing the evolution of each particle, individual contributions to the field are separately calculated and summed up.

In the Eulerian approach instead, one begins defining charge density $\rho(\vec{r}, z, t)$ and current density $\vec{j}(\vec{r}, z, t)$, i.e. particular field quantities, as a function of coordinates and time. One is no more interested in knowing the evolution of each single particle but only to observe charges passing through a given longitudinal position, in order to obtain information about ρ and $\vec{j}$. Once these two fields are determined, one can solve Maxwell's equations for the electric field, with ρ and $\vec{j}$ as macroscopic electromagnetic sources.

8.1.1 Lagrangian approach

We consider an electron bunch moving along the setup specified in Fig. 1(a).

Given a reference point, e.g. $z = 0$, along the trajectory one may specify the phase-space coordinates of a given electron with the help of six data: position of the electron, $\vec{l}$, angular deflection $\vec{\eta}$, energy $\delta\gamma$, and arrival time, τ, all relative to the position of a reference electron with position $\vec{r}_0(0)$, transverse velocity $\vec{v}_{\perp 0}(0)$, nominal energy $\mathcal{E}_0$ and arrival time $t = 0$, all given at position $z = 0$. Using the index k to identify a certain particle one finds the temporal Fourier transform of the radiation pulse at a given frequency ω as a sum of many independent contributions:

$$\vec{\tilde{E}}(\vec{r}, z, \omega) = \sum_{k=1}^{N_e} \vec{\tilde{E}}_{(1)}\left(\vec{l}_k, \vec{\eta}_k, \delta\gamma_k, \tau_k; \vec{r}, z, \omega\right) , \tag{99}$$

where N_e is the total number of particles in the bunch, and $\vec{\tilde{E}}_{(1)}$ is the single particle field contribution from a given particle identified by variables $\vec{l}_k, \vec{\eta}_k, \delta\gamma_k, \tau_k$. Note that we separated these variables from the space-frequency coordinates where the field is calculated with a semicolon.

Eq. (99) forms the basis for calculating the angular spectral flux of radiation. This is essentially done by taking the square modulus of the field in Eq. (99) and averaging over an ensemble of bunches:

$$\frac{dW}{d\omega d\Omega} = \frac{cz^2}{4\pi^2}\left\langle\left|\vec{\tilde{E}}\right|^2\right\rangle = \frac{cz^2}{4\pi^2}\left\langle\left|\sum_{k=1}^{N_e} \vec{\tilde{E}}_{(1)}\left(\vec{l}_k, \vec{\eta}_k, \delta\gamma_k, \tau_k; \vec{r}, z, \omega\right)\right|^2\right\rangle . \tag{100}$$

Let us show that in the particular case when no focusing elements are present, $\vec{\vec{E}}_{(1)}$ in the far zone depends on $\vec{l}_k$ through a phase only. To this purpose, it is sufficient to perform the substitution $\vec{r}_0(z') \longrightarrow \vec{r}_0(z') + \vec{l}$ in Eq. (13), which leads straightforwardly to the phase $-\omega\vec{\theta}\cdot\vec{l}/c$. Thus, in the particular case when there are no focusing elements and electrons have random arrival times (phases) and random offsets, but no energy spread, nor deflections, Eq. (100) yields

$$\begin{aligned}
\frac{dW}{d\omega d\Omega} &= \frac{cz^2}{4\pi^2}\left\langle \sum_{m,n=1}^{N_e} \left|\vec{\vec{E}}_{(1)}\left(\vec{r},z,\omega\right)\right|^2 \exp\left[i\omega(\tau_m-\tau_n)\right]\exp\left[-\frac{i\omega}{cz}\vec{r}\cdot\left(\vec{l}_m-\vec{l}_n\right)\right]\right\rangle \\
&= \frac{cz^2}{4\pi^2}\left|\vec{\vec{E}}_{(1)}\left(\vec{r},z,\omega\right)\right|^2 \left\{N_e + \sum_{m\neq n}\left\langle\exp\left[i\omega(\tau_m-\tau_n)\right]\right\rangle\left\langle\exp\left[-\frac{i\omega}{cz}\vec{r}\cdot\left(\vec{l}_m-\vec{l}_n\right)\right]\right\rangle\right\} \\
&= \frac{cz^2}{4\pi^2}\left|\vec{\vec{E}}_{(1)}\left(\vec{r},z,\omega\right)\right|^2 \cdot N_e\left[1+\left(N_e-1\right)\left|\bar{f}_t(\omega)\right|^2\left|\bar{f}_l\left(\frac{\omega\vec{r}}{cz}\right)\right|^2\right], \qquad (101)
\end{aligned}$$

having recognized that if f_t is the longitudinal bunch profile and f_l the offset distribution at the reference position $z = 0$, one has:

$$\left\langle\exp(i\omega\tau_k)\right\rangle = \int_{-\infty}^{\infty} d\tau_k\, f_t(\tau_k)\exp(i\omega\tau_k) \equiv \bar{f}_t(\omega) \qquad (102)$$

and

$$\left\langle\exp\left(-\frac{i\omega}{cz}\vec{r}\cdot\vec{l}_k\right)\right\rangle = \int_{-\infty}^{\infty} d\vec{l}_k\, f_l\left(\vec{l}_k\right)\exp\left(-\frac{i\omega}{cz}\vec{r}\cdot\vec{l}_k\right) \equiv \bar{f}_l\left(-\frac{\omega\vec{r}}{cz}\right). \qquad (103)$$

In the rest of this Section we will mainly concentrate on the second term in Eq. (101), scaling as $\sim N_e(N_e-1)$, i.e. the coherent term. Although Eq. (101) is known (see e.g. [36, 37, 38]), we choose to shortly report it, because it is still the object of revisions in recently published articles [39, 40, 41], where the angular spectral flux of spontaneous Transition Radiation is found to obey a modified angular distribution depending on the transverse distribution of electrons (see e.g. Eq. (25) of [41], dealing with the case of an infinitely large mirror). In the next Section we will demonstrate that setups in Fig. 1(a) and Fig. 1(c) can be treated with the help of the same mathematical machinery, i.e. a Transition Radiation setup can be formally dealt with as if it were an edge radiation setup. While an exponential cutoff is to be expected in the coherent angular spectral flux, results in [39, 40, 41] indicating a dependence of the

incoherent angular spectral flux on the transverse distribution of electrons is counterintuitive. In fact, as we have seen, the spectrum is calculated by first summing single electron contributions to the field and, second, by averaging the square modulus of the field over an ensemble of bunches. As we have discussed above, a given offset modifies the far-field contribution from a single electron by a phase factor only. Our conclusion, in contrast with [39, 40, 41], is that the final incoherent spectrum cannot depend on the transverse distribution of electrons. The incorrectness of [39, 40, 41] is due to a calculus mistake, which can be found e.g. in Eq. (19) of [41]: the average of the square modulus of a quantity, in fact, is not equal to the square modulus of the average.

Let us go back to the most general situation described in Eq. (99). One can represent the sum in Eq. (99) in terms of an integral over a continuous phase-space distribution of electrons specified at a given position z. Let us assume for simplicity that this reference position is $z = 0$, i.e. in the middle of the straight section. We will indicate the phase-space distribution at $z = 0$ with $f(\vec{l}, \vec{\eta}, \delta\gamma, \tau; 0)$. Eq. (99) can then be substituted with an average of the single particle field over f, yielding

$$\vec{\tilde{E}}(\vec{r}, z, \omega) = N_e \int d\vec{l} d\vec{\eta} d(\delta\gamma) d\tau \; f\left(\vec{l}, \vec{\eta}, \delta\gamma, \tau\right) \vec{\tilde{E}}_{(1)}\left(\vec{l}, \vec{\eta}, \delta\gamma, \tau; \vec{r}, z, \omega\right). \tag{104}$$

Note that substitution of Eq. (99) with Eq. (104) rules out the possibility of recovering the incoherent term in Eq. (101). In fact, the continuous phase-space distribution f already includes an average over an ensemble of bunches. In other words, Eq. (104) has the meaning of a mean field, whose square modulus is essentially the second term in Eq. (101), i.e. the coherent term.

8.1.2 Eulerian approach

Up to now we have been using a microscopic approach, where the single-electron field is averaged over the six-dimensional phase-space distribution of electrons. It is possible to obtain the same results using a macroscopic viewpoint, where solution of Maxwell's equations is found with given macroscopic charge density $\rho(\vec{r}, z, t)$ and current density $\vec{j}(\vec{r}, z, t)$. In this case, one can integrate Maxwell's equations with the help of the usual Green's function.

We begin by writing a general expression for the temporal Fourier transform of charge and current density in terms of the phase-space distribution at a given position down the beamline z. Such phase space-distribution,

$f(\vec{r},\vec{v}_\perp/c,\delta\gamma,t,z)$ can always be written as $f(\vec{l}+\vec{r}_0(z),\vec{\eta}+\vec{v}_{\perp 0}(z)/c,\delta\gamma,\tau+s(z)/v,z)$ where, as we have seen before, the subscript "0" referring to the constrained motion of an electron with $\vec{r}=0$, $\vec{v}_\perp=0$, $\delta\gamma=0$ and $t=0$ at $z=0$. The meaning of this writing is that here we consider the evolution of f along z as the result of two combined effects. On the one hand we have a z-dependent shift of the f-distribution as a whole due to the reference motion $\vec{r}_0(z)$, $\vec{v}_{\perp 0}(z)$ and $s(z)$, while on the other hand we have a more generic evolution in z due to self-interactions and external fields. The distribution f is obviously of the form $f(\vec{l},\vec{\eta},\delta\gamma,\tau,z)$. It follows that the Fourier transform of f, $\bar{f}$, can be written as

$$\begin{aligned}\bar{f}(\vec{l},\vec{\eta},\delta\gamma,\omega,z) &= \int_{-\infty}^{\infty} dt\,\exp[i\omega t] f(\vec{l},\vec{\eta},\delta\gamma,\tau,z)\\ &= \exp\left[\frac{i\omega s(z)}{v}\right]\int_{-\infty}^{\infty} d\tau\,\exp[i\omega\tau] f(\vec{l},\vec{\eta},\delta\gamma,\tau,z)\\ &\equiv \exp\left[\frac{i\omega s(z)}{v}\right]\widetilde{f}(\vec{l},\vec{\eta},\delta\gamma,\omega,z)\,, \end{aligned} \tag{105}$$

where the usefulness in the definition of $\widetilde{f}$ is that $\widetilde{f}$ is a slowly function of z on the scale of $\lambda\!\!\!^{-}$. One has therefore

$$\begin{aligned}\bar{\rho}(\vec{r},z,\omega) &= \frac{(-e)N_e}{c}\int d\vec{l}d\vec{\eta}d(\delta\gamma)\bar{f}(\vec{l},\vec{\eta},\delta\gamma,\omega,z)\delta(\vec{l}+\vec{r}_0(z)-\vec{r})\\ &= \frac{(-e)N_e}{c}\int d\vec{\eta}d(\delta\gamma)\widetilde{f}(\vec{r}-\vec{r}_0(z),\vec{\eta},\delta\gamma,\omega,z)\exp\left[\frac{i\omega s(z)}{v}\right]\\ &\equiv \widetilde{\rho}(\vec{r}-\vec{r}_0(z),z,\omega)\exp\left[\frac{i\omega s(z)}{v}\right]\end{aligned} \tag{106}$$

and

$$\begin{aligned}\vec{\bar{j}}(\vec{r},z,\omega) &= \frac{(-e)N_e}{c}\int d\vec{l}d\vec{\eta}d(\delta\gamma)\,(c\vec{\eta}+\vec{v}_\perp(z))\,\bar{f}(\vec{l},\vec{\eta},\delta\gamma,\omega,z)\delta(\vec{l}+\vec{r}_0(z)-\vec{r})\\ &= \frac{(-e)N_e}{c}\int d\vec{\eta}d(\delta\gamma)\,(c\vec{\eta}+\vec{v}_\perp(z))\,\widetilde{f}(\vec{r}-\vec{r}_0(z),\vec{\eta},\delta\gamma,\omega,z)\exp\left[\frac{i\omega s(z)}{v}\right]\\ &\equiv \vec{\widetilde{j}}(\vec{r}-\vec{r}_0(z),z,\omega)\exp\left[\frac{i\omega s(z)}{v}\right]\,,\end{aligned} \tag{107}$$

where we introduced, together with $\widetilde{f}$ and with the usual field envelope $\vec{\widetilde{E}}=\vec{\bar{E}}\exp[-i\omega z/c]$, also quantities $\widetilde{\rho}=\bar{\rho}\exp[-i\omega s(z)/v]$ and $\vec{\widetilde{j}}=\vec{\bar{j}}\exp[-i\omega s(z)/v]$.

Note that $\widetilde{\rho} = \widetilde{\rho}(\vec{r} - \vec{r}_0(z), z, \omega)$ (the same applies to $\vec{\vec{j}}$). One writes the paraxial equation for the field as

$$\left(\nabla_\perp{}^2 + \frac{2i\omega}{c}\frac{\partial}{\partial z}\right)\vec{\vec{E}} = 4\pi \exp\left\{i\omega\left(\frac{s(z)}{v} - \frac{z}{c}\right)\right\} \times\left[\frac{i\omega}{c^2}\vec{\vec{j}}(\vec{r} - \vec{r}_0(z), z, \omega) - \vec{\nabla}_\perp\widetilde{\rho}(\vec{r} - \vec{r}_0(z), z, \omega)\right] \qquad (108)$$

in analogy with Eq. (9) for a single particle. We solve Eq. (108) with the help of the Green's function in Eq. (10), similarly as in Eq. (11), but with the important difference that, now, we cannot carry out the integration over transverse coordinates. We therefore obtain

$$\vec{\vec{E}} = 4\pi\int_{-\infty}^{z} dz' \int d\vec{r'}\left\{\frac{i\omega}{c^2}\vec{\vec{j}}(\vec{r'} - \vec{r}_0(z'), z', \omega)G\left(\vec{r} - \vec{r'}, z - z'\right) + \widetilde{\rho}(\vec{r'} - \vec{r}_0(z'), z', \omega)\vec{\nabla'}_\perp G\left(\vec{r} - \vec{r'}, z - z'\right)\right\}\exp\left\{i\omega\left(\frac{s(z)}{v} - \frac{z}{c}\right)\right\}, \qquad (109)$$

Explicit substitution of Eq. (10) in Eq. (109) finally yields

$$\vec{\vec{E}}(z, \vec{r}) = -\frac{i\omega}{c}\int_{-\infty}^{z} dz' \int d\vec{r'}\frac{1}{z - z'}\exp\left\{i\omega\left[\frac{|\vec{r} - \vec{r'}|^2}{2c(z - z')} + \int_0^{z'}\frac{d\bar{z}}{2\gamma_z^2(\bar{z})c}\right]\right\} \times\left[\frac{\vec{\vec{j}}(\vec{r'} - \vec{r}_0(z'), z', \omega)}{c} - \frac{\vec{r} - \vec{r'}}{z - z'}\widetilde{\rho}(\vec{r'} - \vec{r}_0(z'), z', \omega)\right]. \qquad (110)$$

Lagrangian and Eulerian approaches are equivalent. In simple cases, e.g. when trajectories of electrons are a simple function like a straight motion and Eq. (13) can be calculated analytically, the Lagrangian method looks more transparent. However, in the most general case, one needs to account for the presence of focusing elements and self-interactions. The evolution of the six-dimensional phase space becomes complicated and numerical methods should be used. Naturally, the Lagrangian approach can be applied when the evolution of the six-dimensional phase-space is known via simulations. Then, Eq. (13) has to be calculated numerically for each (macro)particle. The Eulerian approach can be more advantageous. Computer codes can calculate charge and current density distribution as a function of z accounting for focusing elements and self-interactions, and the macroscopic method may be more practical, because one integrates Eq. (110) once and for all. One does not need to have any explicit knowledge of the angle distribution, or of the

energy spread distribution to calculate the field. Once charge and current density are known, one only needs to (numerically) integrate Maxwell's equations. This is because we are dealing with a macroscopic system, where only macroscopic current and charge density are important. In other words, the behavior of Maxwell's equations is influenced by projections of the 6D phase-space on the real space (ρ and $\vec{j}$), but not by the 6D phase-space itself.

8.2 Near Field Coherent Edge Radiation

Let us consider the usual setup in Fig. 1(a) and assume, till the end of the Section, that there are no focusing elements nor self-interactions along the straight section. By this, we assume that electrons move along the straight line between two bending magnets. We will adopt the Lagrangian approach to characterize coherent ER emission due to overall temporal bunch profile, without considering, for now, microbunching.

An algorithm for describing radiation emission is straightforward. One begins with the expression for the field generated in the far zone by a single electron occupying a certain position in phase-space at a fixed reference longitudinal position z. Then, one integrates the single-particle expression over the phase-space distribution, thus getting the equivalent of Eq. (104) in the far zone. Finally, when the far-zone field (averaged over a given electron distribution) is known, the field in the near-zone can be calculated as has been done before, by back-propagating the far-zone expression.

In the case of edge radiation, the far-zone expression for the field of a single-particle having phase-space coordinates $(\vec{l}, \vec{\eta}, \delta\gamma, \tau)$ at $z = 0$ is given by:

$$\vec{\tilde{E}}_{(1)}\left(\vec{l}, \vec{\eta}, \delta\gamma, \tau; \vec{\theta}, z, \omega\right) = \frac{i\omega eL}{c^2 z} \exp\left[i\omega\tau\right] \exp\left[\frac{i\omega\theta^2 z}{2c}\right] \exp\left[-\frac{i\omega\vec{\theta}\cdot\vec{l}}{c}\right] \times \left(\vec{\theta} - \vec{\eta}\right) \operatorname{sinc}\left\{\frac{\omega L}{4c}\left[\left|\vec{\theta} - \vec{\eta}\right|^2 + \frac{1}{\gamma^2} - \frac{2\delta\gamma}{\gamma^3}\right]\right\} . \quad (111)$$

Note that Eq. (111) is a straightforward generalization of Eq. (20), obtained by performing a rigid rotation of the reference system and a translation of the observation point *without* changing the observation plane of interest, which remains perpendicular to the z axis of the initial reference system. This explains why the combination $\vec{\theta} - \vec{\eta}$ does not enter the phase in Eq. (111). This solves the problem for the field in the case when trajectories are straight lines between two bending magnets without focusing elements, and self-interactions are negligible.

The field in the far zone should be subsequently averaged over f. This is accomplished by substituting Eq. (111) into Eq. (104). Simplifications arise when the phase-space distribution can be separated in product of different factors depending only on offset, deflection, energy spread and arrival time for some choice of the reference position z. Such separability is not always granted. However, the choice of some particular reference point may help simplifying calculations. For example, the distribution of offsets and deflections factorizes when the reference position in z is fixed at the minimal value of the betatron function. In the following we will consider two different study cases of interest.

I. Case $f = f_l(\vec{l})\delta(\vec{\eta})\delta(\delta\gamma/\gamma)f_\tau(\tau)$**.** This is one of the simplest situations, when both angular distribution and energy distribution can be neglected, typical of well-collimated, monochromatic high-quality beams produced in conventional accelerators. Simpler subcases for $f_l = \delta(\vec{l})$ or $f_\tau = \delta(\tau)$ (or both) can be easily inferred from this more general model.

As we discussed before, the presence of an offset modifies the single-particle field by a phase factor only. In case of ER, Eq. (104) simplifies to

$$\begin{aligned}\vec{\tilde{E}}(z,\vec{\theta},\omega) &= N_e F\left(\omega,\vec{\theta}\right)\widetilde{E}_{(1)} \\ &= \frac{i\omega e N_e F(\omega,\vec{\theta})L}{c^2 z}\exp\left[\frac{i\omega\theta^2 z}{2c}\right]\vec{\theta}\,\mathrm{sinc}\left\{\frac{\omega L}{4c}\left[\frac{1}{\gamma^2}+\theta^2\right]\right\}\,,\end{aligned} \tag{112}$$

where

$$F\left(\omega,\vec{\theta}\right) = \int dt f_\tau(\tau)\exp\left[i\omega\tau\right]\int d\vec{l} f_l(\vec{l})\exp\left[-\frac{i\omega}{c}\vec{\theta}\cdot\vec{l}\right]\,. \tag{113}$$

Thus, in this case, we obtain a simple result amounting to a multiplication of the structure factor F defined in Eq. (113) by the single-particle field. The structure factor F is the product of the Fourier transform of f_τ (the bunch longitudinal profile), $\bar{f}_\tau$, and the Fourier transform of the bunch transverse profile.

To sum up, if one knows results for a single electron, like those calculated above for ER, TUR, or any other kind of radiation, and one needs to calculate radiation from an electron bunch, all is needed to do is to multiply the result for a single electron by F; results in the near zone are obtained remembering that $\vec{\theta} = \vec{r}/z$. Note that in the case of a single electron with zero offset and

arrival time $\tau_k = 0$, $\bar{f_\tau} = 1$ and $f_l(\vec{l}) = \delta(\vec{l})$, so that $F = 1$ and one recovers Eq. (13).

In the present case I, the form factor F does not change during the motion of electrons along the z axis. This is in agreement with our previous assumption about energy spread and angular distribution of the bunch. In fact, as said before, we assume that $f_\tau(\tau)$ remains unchanged during the motion along the beamline. Concerning the transverse structure, we are assuming that the transverse size and shape of the bunch do not vary either.

With the help of Eq. (24) and Eq. (112) we obtain the angular spectral flux

$$\frac{dW}{d\omega d\Omega} = \frac{cN_e^2 z^2}{4\pi^2}\left|\vec{\vec{E}}\right|^2 = |F(\omega,\theta)|^2\,\frac{cN_e^2 z^2}{4\pi^2}\left|\vec{\vec{E}}_{(1)}\right|^2 . \tag{114}$$

Note that Eq. (114) is just the second (coherent) term in Eq. (101). We should stress that the near-zone problem for coherent ER can be solved, similarly as in the single particle case, starting from the far-zone data. Therefore, it can be solved using Eq. (112).

Consider first the case $\phi \ll 1$. The problem of calculation of the virtual source distribution in the middle of the straight section can be basically reduced to a Fourier transform of the far-field distribution. Therefore, the specification of virtual sources also simplifies to a convolution between the single particle virtual source and a spatial Fourier Transform of the form factor F. Remembering Eq. (16), and with the help of Eq. (20), Eq. (30) and Eq. (112) one explicitly obtains

$$\begin{aligned}\vec{\vec{E}}(0,\vec{r}) &= N_e \bar{f_\tau}(\omega)\vec{\vec{E}}_{(1)}(0,\vec{r}) * f_l(\vec{r}) \\ &= N_e \bar{f_\tau}(\omega)\int d\vec{l}\left[-\frac{4i\omega e}{c^2 L}\left(\vec{r}-\vec{l}\right)\mathrm{sinc}\left(\frac{\omega\left|\vec{r}-\vec{l}\right|^2}{cL}\right)\right] f_l(\vec{l}) ,\end{aligned} \tag{115}$$

where $\vec{\vec{E}}_{(1)}(0,\vec{r})$ indicates the single-particle field distribution at the virtual source in Eq. (30), and the symbol " $*$ " denotes the convolution product as defined in the second line of Eq. (115). Note that the virtual source in Eq. (115) can be imaged by a lens when the object plane corresponds to position $z = 0$.

Similar remarks hold for the case of a generic value of ϕ. In fact, as is well-known from Eq. (37), the expression for the single-particle field in the far-zone can be split in the sum of two spherical-wave contributions,

and both terms are subsequently multiplied by the same form factor. Thus, analogously to Eq. (115), one obtains

$$\vec{\vec{E}}\,(\pm L/2,\vec{r}) = N_e \bar{f_\tau}(\omega)\vec{\vec{E}}_{(1)}(\pm L/2,\vec{r}) * f_l(\vec{r})\ , \tag{116}$$

where now $\vec{\vec{E}}_{(1)}(\pm L/2,\vec{r})$ indicate the single-particle field distribution at the virtual source positions $\pm L/2$ in Eq. (39).

II. Case $f = f_{l,\eta}(\vec{l},\vec{\eta})\delta(\delta\gamma/\gamma)f_\tau(\tau)$**.** In this situation we still neglect the energy-spread distribution, but we account for a given distribution in angles in addition to the case treated in I. In other words, the bunch has a finite emittance. Factorization of f_l and f_η at the reference point ($z = 0$) indicates that the betatron functions are minimal at that position. In practice, angular distribution is important for the case depicted in Fig. 1(d), i.e. for a laser-plasma accelerator device. In this case, it is more natural to assume that the minimal betatron function is located at $z = -L/2$, rather than at $z = 0$. Then, the product $f_l(\vec{l})f_\eta(\vec{\eta})$ must be consistently substituted by a non-factorized distribution $f_{l,\eta}(\vec{l},\vec{\eta})$. We will consider a Gaussian electron bunch with rms size σ_l. Additionally, we introduce a Gaussian angular distribution with rms σ_η and assume, for simplicity, that these rms quantities apply both in the horizontal and in the vertical plane at $z = -L/2$. As a result, one has the following distribution at $z = 0$ (which may be alternatively rewritten in terms of Twiss parameters):

$$f_{l,\eta}\,(l,\eta) = \frac{1}{4\pi^2\sigma_l^2\sigma_\eta^2}\exp\left[-\frac{(l-L\eta/2)^2}{\sigma_l^2} - \frac{\eta^2}{\sigma_\eta^2}\right]. \tag{117}$$

With this in mind, Eq. (104) simplifies to

$$\begin{aligned}\vec{\vec{E}}\left(z,\vec{\theta},\omega\right) = \frac{i\omega e N_e L \bar{f_\tau}(\omega)}{c^2 z}\int d\vec{l}d\vec{\eta}\, f_{l,\eta}\,(l,\eta)\exp\left[\frac{i\omega\theta^2 z}{2c}\right] \\ \times\exp\left[-\frac{i\omega\vec{\theta}\cdot\vec{l}}{c}\right]\left(\vec{\theta}-\vec{\eta}\right)\mathrm{sinc}\left\{\frac{\omega L}{4c}\left[\left|\vec{\theta}-\vec{\eta}\right|^2+\frac{1}{\gamma^2}\right]\right\}\ ,\end{aligned} \tag{118}$$

Generalization of this study case to the situation with a finite energy spread, still relevant e.g. for laser-plasma accelerator devices can be performed straightforwardly.

We will now study the particular case of an electron bunch modulated in density at a given wavelength. In this case, coherent emission is not due to the overall bunch profile, but to the presence of a modulation superimposed to such profile.

In some cases modulation of the bunch can be set up on purpose, while in others it can be a detrimental effect.

Typical examples of parasitic microbunching mechanisms at FEL facilities are driven by Coherent Synchrotron Radiation (CSR) in the bending magnet of a bunch compressor chicane [42, 43, 44] or Longitudinal Space Charge force (LSC) [45]. Initial shot-noise density modulation at a given frequency induces energy modulation at the same frequency due to CSR or LSC impedances. Such energy modulation is subsequently transformed back into density modulation through a dispersive section, eventually leading to a beam instability. The dispersive section is typically the magnetic compression chicane itself. In this case, microbunching is usually an unwanted phenomenon, which tends to spoil the high-quality electron beam needed for the FEL process.

However, in other cases, a modulation at optical wavelengths can be printed on purpose onto the electron bunch with the help of a (quantum) laser and a modulator undulator followed by a dispersive section. Optically modulated electron bunches can be used for diagnostic purposes and in pump-probe techniques as well [46, 24].

If the bunch is modulated at a given wavelength $\lambda\!\!\!^{-}_m$, one has $f_\tau(\tau) = f_{\tau 0}(\tau)[1 + a_0 \cos(c\tau/\lambda\!\!\!^{-}_m)]$, where $f_{\tau 0}$ is a given longitudinal profile and a_0 is the modulation level.

Let us consider a typical Gaussian model for the beam, specified by

$$f_l\left(\vec{l}\right) = \frac{1}{2\pi\sigma_l^2} \exp\left[-\frac{l^2}{2\sigma_l^2}\right], \tag{119}$$

σ_l being the *rms* beam transverse dimension and by

$$f_{\tau 0}(\tau) = \frac{1}{\sqrt{2\pi}\sigma_T} \exp\left[-\frac{\tau^2}{2\sigma_T^2}\right]. \tag{120}$$

Here we are assuming that the wavefront of the density distribution of the modulation is perpendicular to the velocity of electrons, and is uniform in

the transverse direction as a_0 is not a function of $\vec{r}$. The latter assumption is close to reality, because the waist of the seed laser is much larger than the size of the electron bunch in the modulator undulator, due to the extreme high-quality of the electron bunch in XFELs.

Near the modulation frequency $\omega_m = c/\lambda\!\!\!^{-}_m$, a bunch with modulated Gaussian temporal profile and rms duration σ_T yields

$$\bar{f_\tau}(\omega) = \frac{a_0}{2}\left\{\exp\left[-\frac{\sigma_T^2}{2}(\omega-\omega_m)^2\right] + \exp\left[-\frac{\sigma_T^2}{2}(\omega+\omega_m)^2\right]\right\}\,, \tag{121}$$

where $\bar{f_\tau}(\omega)$ is, as before, the Fourier transform of the temporal profile of the bunch. In deriving Eq. (121) we used an adiabatic approximation that can be taken advantage of in practical situations involving XFELs, where the optical modulation wavelength is much shorter than the bunch length, i.e. $c\sigma_T/\lambda\!\!\!^{-}_m \gg 1$. In this case we have another large parameter in the problem, which considerably simplifies the treatment. In fact, since we are interested in coherent emission around optical wavelengths, in calculating Eq. (121) we neglected the Fourier transform of the first term of $f_\tau(\tau)$, i.e. $f_{\tau 0}(\tau)$. Obviously, this would not be possible for frequencies in the range $1/\sigma_T$. From Eq. (121) follows that radiation is exponentially suppressed for frequencies outside the bandwidth $1/\sigma_T$ centered at the modulation frequency ω_m.

The exponential suppression in Eq. (121) has its analogous in the transverse direction too. With the help of Eq. (119) one finds

$$F\left(\omega,\vec{\theta}\right) = \bar{f_\tau}(\omega)\exp\left[-\frac{\omega^2\theta^2\sigma_l^2}{2c^2}\right]\,. \tag{122}$$

Note that θ is usually normalized to a characteristic angle that depends on the system considered. In our ER case, such angle is $\sqrt{\lambda\!\!\!^{-}/L_f}$, with $L_f = \min[L, \gamma^2\lambda\!\!\!^{-}]$. With this in mind, the exponential suppression in Eq. (122) can be written in normalized units as

$$F\left(\omega,\vec{\hat{\theta}}\right) = \bar{f_\tau}(\omega)\exp\left[-\frac{\hat{\theta}^2 N}{2}\right]\,, \tag{123}$$

where we defined

$$N = \frac{\sigma_l^2}{\lambda\!\!\!^{-} L_f}\,. \tag{124}$$

The parameter N is analogous to a Fresnel number in diffraction theory, and is the only (dimensionless) transverse parameter related to the radiation emission in the model defined by Eq. (119) and Eq. (120). When $N \ll 1$ the exponential factor in Eq. (123) returns unity, and one gets back the single-electron radiation profile, whereas the flux is possibly modified by the presence of $\bar{f}_\tau$. When $N \gtrsim 1$ the intensity profile as a function of angles is exponentially suppressed.

Integration of Eq. (114) in $d\omega$ and in $d\Omega$ gives the total energy radiated. Since we are dealing with an electron bunch modulated at optical wavelengths we are interested in narrow-bandwidth emission.

Within the above-mentioned adiabatic approximation we can consider the wavelength in $\vec{\bar{E}}_{(1)}$ appearing in Eq. (114) fixed, i.e. $\lambda\!\!\!^{-} = \lambda\!\!\!^{-}_m$. Then, integration in $d\omega$ can be easily performed using the fact that $\int_0^\infty d\omega \left|\bar{f}_\tau(\omega)\right|^2 = \sqrt{\pi} a_0^2/(4\sigma_T)$, leading to

$$\frac{dW}{d\Omega} = \frac{\sqrt{\pi} c z^2 N_e^2 a_0^2}{16\pi^2 \sigma_T} \exp\left[-\frac{\omega_m^2 \theta^2 \sigma_l^2}{c^2}\right] \left|\vec{\bar{E}}_{(1)}\right|^2 \ . \tag{125}$$

Integration over angles can be performed analytically in particular limiting cases.

In the following we will discuss the setup in Fig. 1(a). However, our result can be easily extended to the case of Fig. 1(b) and Fig. 1(c). Let us first consider the case $\phi \ll 1$. One has

$$W = \frac{2N_e^2 e^2 a_0^2}{\sqrt{\pi}\sigma_T c} \int_0^\infty \frac{d\theta}{\theta} \sin^2\left[\frac{\omega_m L \theta^2}{4c}\right] \exp\left[-\frac{\omega_m^2 \theta^2 \sigma_l^2}{c^2}\right] . \tag{126}$$

Introducing dimensionless units allows one to write the total number of photons emitted at ω_m as

$$N_{ph} = \frac{2N_e^2 \alpha a_0^2}{N_m \sqrt{\pi}} \int_0^\infty \frac{d\hat{\theta}}{\hat{\theta}} \sin^2\left[\frac{\hat{\theta}^2}{4}\right] \exp\left[-N\hat{\theta}^2\right] = \frac{N_e^2 \alpha a_0^2}{4N_m \sqrt{\pi}} \ln\left[1 + \frac{1}{4N^2}\right] , \tag{127}$$

where $\alpha \equiv e^2/(\hbar c) = 1/137$ is the fine structure constant and $N_m = \sigma_T \omega_m$ is the number of modulation wavelengths included in the bunch. It should be noted that Eq. (127) is logarithmically divergent for $N \longrightarrow 0$. It is therefore interesting to discuss the region of applicability of Eq. (127) in the limit

for small values of N. Such asymptote can usually be exploited when dealing with XFEL setups, because of the extremely high-quality of the electron bunch (small emittance). The expression used for $\vec{\vec{E}}_{(1)}$ assumes that the sharp-edge approximation holds, i.e. $\delta \ll 1$. In this case, the formation length of the bending magnet at the end of the straight section L_{fb} is much smaller than the straight section length L. The transverse spot-size of the radiation associated with bending magnet emission, and is of order $\lambda\!\!\!^{-} L_{fb}$ is then the smallest characteristic transverse size of the problem. If the electron bunch size becomes of order $\lambda\!\!\!^{-} L_{fb}$, our electrodynamic description cannot distinguish anymore between a bunch with finite transverse size and a point. In this case one should substitute σ_l with $\lambda\!\!\!^{-} L_{fb}$. This amounts to the substitution $N \longrightarrow \delta$. Thus in the limit $N \ll \delta$ we prescribe the substitution of N with δ for estimations.

Finally, since $c\sigma_T/\lambda\!\!\!^{-}_m \gg 1$, it makes sense to introduce an expression for the instantaneous power as a function of the instantaneous (peak) current $I(\tau)$ and modulation $a_0(\tau)$, if the seed laser duration is not too long compared to the bunch duration. To this purpose, we consider a stepped-profile model for the bunch $f_{\tau 0}(\tau) = 1/T$ for $-T/2 < \tau < T/2$ and zero elsewhere. It follows that

$$\bar{f_\tau}(\omega) = \frac{a_0 c}{\omega\omega_m}\left\{\frac{\omega-\omega_m}{c}\sin\left[\frac{T\omega\omega_m}{2(\omega-\omega_m)}\right] + \frac{\omega+\omega_m}{c}\sin\left[\frac{T\omega\omega_m}{2(\omega+\omega_m)}\right]\right\} . \tag{128}$$

Then, in the limit for $T \gg \lambda\!\!\!^{-}_m/c$ one has $\int_0^\infty d\omega \left|\bar{f_\tau}(\omega)\right|^2 \simeq a_0^2 \pi T$, and

$$\frac{dP}{d\Omega} = \frac{1}{T}\frac{dW}{d\Omega} = \frac{c a_0^2 I_0^2 \pi z^2}{4\pi^2 e^2}\exp\left[-\frac{\omega_m^2\theta^2\sigma_l^2}{c^2}\right]\left|\vec{\vec{E}}_{(1)}\right|^2 , \tag{129}$$

where $dP/d\Omega$ is the angular distribution of power. If now the current $I = I(\tau)$ and the modulation level $a = a(\tau)$ are slowly varying functions of time on the scale $\lambda\!\!\!^{-}_m/c$, one obtains for $\phi \ll 1$

$$\frac{dP}{d\Omega} = \frac{\omega_m^2 L^2 a(\tau)^2 I(\tau)^2}{4\pi c^3}\exp\left[-\frac{\omega_m^2\theta^2\sigma_l^2}{c^2}\right]\theta^2 \mathrm{sinc}\left[\frac{\omega_m L\theta^2}{4c}\right] . \tag{130}$$

Eq. (130) can be used in order to study the general case of an electron bunch with arbitrary gradient profile and amplitude of modulation.

Let us now turn to the case when $\phi \gg 1$ for the single-edge radiation ($\gamma^2\lambda\!\!\!^{-} \ll d_2 \ll L$ and $r \ll L/\gamma$). Introducing apodization of the detector on a

characteristic angular scale σ_a and using Eq. (42) we obtain [6]

$$W = \frac{N_e^2 e^2 a_0^2}{2\sqrt{\pi}\sigma_T c} \int_0^\infty d\xi \frac{\gamma^4 \xi^3}{(\gamma^2\xi^2+1)^2} \exp\left[-\frac{\omega_m^2 \xi^2 \sigma_l^2}{c^2} - \frac{\xi^2}{2\sigma_a^2}\right] . \tag{131}$$

Note that apodization (through σ_a) and transverse bunch length (through $\lambda\!\!\!^{-}_m/\sigma_l$) play the same role from a mathematical viewpoint. Also note that, in order to use Eq. (42), we must require that we are within its limits of applicability, i.e. $d_2 \cdot \min(\sigma_a, \lambda\!\!\!^{-}_m/\sigma_l) \ll L/\gamma$ (always with $\gamma^2 \lambda\!\!\!^{-}_m \ll d_2 \ll L$).

Taking advantage of dimensionless units one can write the total number of photons emitted at ω_m as

$$\begin{aligned} N_{ph} &= \frac{N_e^2 \alpha a_0^2}{2N_m\sqrt{\pi}} \int_0^\infty d\hat{\xi} \frac{\hat{\xi}^3}{(\hat{\xi}^2+\phi)^2} \exp\left[-(N+A)\hat{\xi}^2\right] \\ &= \frac{N_e^2 \alpha a_0^2}{4N_m\sqrt{\pi}} \left\{-1 + \left[1+(A+N)\phi\right]\Gamma[0,(A+N)\phi]\exp[(A+N)\phi]\right\} , \end{aligned} \tag{132}$$

where $A \equiv \lambda\!\!\!^{-}/(2L\sigma_a^2)$ is analogous to the N parameter in Eq. (124) and accounts for apodization effects, and $\Gamma(a,z) = \int_z^\infty t^{a-1}\exp(-t)dt$ is the incomplete gamma function. Discussion of asymptotic cases for different values of N and A is possible on the basis of Eq. (132).

9 Extraction of edge radiation by a mirror

9.1 Backward Transition and Diffraction radiation

A setup where edge radiation from an upstream bending magnet is extracted by a mirror is shown in Fig. 1(c). In the particular case depicted in that figure, radiation is reflected by a hole mirror and sent to a far-infrared spectrometer. This example refers to a method [47] where coherent radiation is used to monitor the bunch length at XFEL setup, but similar setups can also be used to collect incoherent radiation in the optical range. The size and shape of the mirror may vary. A hole may be present in the mirror or not,

[6] In particular, Eq. (131) applies to the case when coherent TR due to microbunching is outcoupled by a mirror and postmirror optics can be modelled with a Gaussian pupil profile. In this case, $z - L/2$ indicates the distance from the mirror.

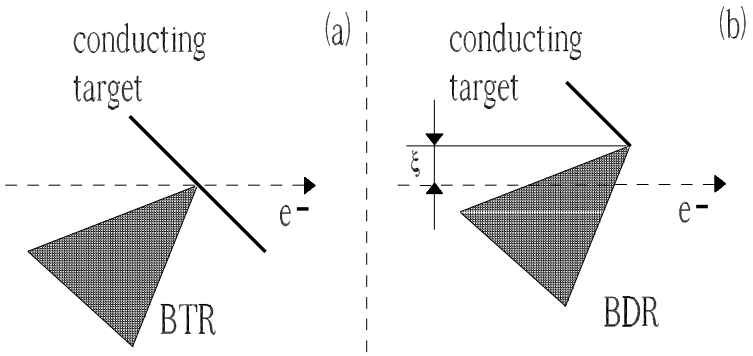

Fig. 26. Geometry of backward transition radiation (BTR) (a), backward diffraction radiation (BDR) (b).

and the geometry of the experimental arrangement depends on the particular setup considered. Anyway, in its basic lines, a standard edge-radiation diagnostic setup consists, similarly as in Fig. 1(c), of a mirror positioned at some distance after a bend and rotated by an angle $\pi/4$ in the direction of the electron bunch to allow extraction of radiation through a vacuum window. Such setup can be used for longitudinal bunch-length measurements in the mm and sub-mm range as well as for transverse electron bunch diagnostics in the optical wavelength range [47, 48, 49].

Consider the straight section after the bend. If this is long enough so that $\phi \gg 1$ (and $\delta \cdot \phi \ll 1$, i.e. $\lambda\!\!\!^{-} \gg \lambda\!\!\!^{-}_c$), radiation collected by the mirror is the usual Transition Radiation (TR) first noted by Ginzburg and Frank [50] and considered in a number of publications written during the last half century. In recent years there has been a good deal of interest in TR, because this form of radiation has found useful applications, e.g. in diagnostic for ultrarelativistic beams [51, 52, 53, 54, 55]. These papers describe an electron crossing an interface between two media with different dielectric constants and they refer, in particular, to the case of the boundary between vacuum and an ideal conductor. As a consequence of the crossing, time-varying currents are induced at the boundary. These currents are responsible for TR (see Fig. 26 left). The metallic mirror, that is treated as the source of TR, is usually modelled with the help of a Physical Optics approach. This is a well-known high-frequency approximation technique, often used in the analysis of electromagnetic waves scattered from large metallic objects. Surface current entering as the source term in the propagation equations of the scattered field are calculated by assuming that the magnetic field induced on the surface of the object can be characterized using Geometrical Optics, i.e. assuming that the surface is locally replaced, at each point, by its tangent plane.

As mentioned before, one typically assumes that the Ginzburg-Frank formula can be used, i.e. the field distribution is proportional to $K_1[\omega r/(\gamma c)]$. In

terms of parameters introduced in this paper, this approximation has sense only when $\phi \gg 1$. However, even for this case, one should always specify the transverse region of applicability of the usual TR formulas, which is typically neglected (as we will see, this region is for $r \ll \phi \lambda\!\!\!^{-}\gamma = L/\gamma$, with $\phi \gg 1$). Moreover, mainly due to an increased electron energy, today setups often meet, in practice, condition $\phi \lesssim 1$ even in the optical wavelength range. In this case one should account for the whole setup when discussing the reflected radiation, and not only for the metallic mirror. In other words, as we will see, the problem of extraction of edge radiation reduces to the well-studied TR problem only asymptotically, i.e. for $\phi \gg 1$. In this paper we will still keep on talking about TR or, with some abuse of language, even when usual TR formulas do not apply anymore ($\phi \lesssim 1$, or $r \gtrsim L/\gamma$).

When dealing with the above-discussed setup, one usually talks about Backward Transition Radiation (BTR). BTR is widely used for different purposes, because it allows for low background radiation levels. We will consider a whole range of setups for BTR, without treating their geometry in detail, and we will give an algorithm to deal with these systems in all generality. In fact, in all cases, the main problem is in the specification of the electric field distribution at some position where a mirror is present (the hole mirror in the example of Fig. 1(c)). The only element to be accounted for, aside for the mirror itself, is an upstream dipole magnet. Note that the mirror is tilted as in Fig. 1(c), i.e. it is not perpendicular with respect to the optical axis. In principle, one may account for this tilting, but in practice the projection of the mirror on the optical axis is negligible compared with the distance to the dipole, and one may consider the screen as not tilted.

Note that Diffraction Radiation (DR) appears when charged particles move in the vicinity of a medium (e.g. a conductive mirror) at some given impact parameter ξ, and has been recently suggested as a possible tool for non-invasive bunch diagnostics. DR is obviously related to TR and, in particular, it can be treated starting from the knowledge of the electric field distribution at the mirror, and subsequently applying physical optics techniques. BDR in the optical wavelength range has been measured and applied for transverse electron beam diagnostics (see e.g. [48, 49]). A schematic comparison between a BDR and a BTR emission is shown in Fig. 26.

It should be stressed that specification of the field at the target position must be considered as the first step to the solution of a more complicated problem, i.e. the characterization of the field at a detector position. Such first step is considered separately, because the field at the target plane is independent of the type of target and detector. Once the field at the target position is known, the full problem can be solved with the help of Physical Optics techniques, where one should account for diffraction effects due to the particular shape of the mirror.

In the following we will focus on the problem of field characterization at the target position. A virtual source method can be applied. Our algorithm consists of the following steps: (i) propagate the field from the upstream virtual source to the mirror, (ii) add the field from the downstream virtual source.

Note that, in contrast to the study case of a straight section between two bends considered before, numerical methods involving direct integration of Maxwell's equations (e.g. with the help of SRW) down the optical axis up to the mirror will fail, because electromagnetic sources must be propagated up to the observation plane, and integration of the Green's function up to that position yields a singularity (independently of the value of δ). In our virtual source approach we also deal with a singularity, but this is isolated in a single term, and expressed by means of an analytical function (the Bessel K_1 function in Eq. (39)), allowing straightforward presentation of results. The same approach has been proposed in [56] to discuss the setup in Fig. 1(c).

Let us focus in detail on our generic BTR setup. Following the algorithm described above, we model the system with the help of two virtual sources at $z = \pm L/2$, i.e. at the end of the bend and at the mirror. As said before, Eq. (39) can be used to describe the virtual sources. Application of the propagation formula Eq. (14) allows to calculate the field at any distance z in free-space for the source located at $z = -L/2$. In order to simplify the presentation of the electric field we take advantage of polar coordinates. We propagate the upstream virtual source (located at $z = -L/2$) up to the mirror position at $z = L/2$, and we add the field distribution for the downstream source at $z = L/2$.

At $z = L/2$ (i.e. at the mirror position) we obtain

$$\vec{\tilde{E}}\left(\frac{L}{2},\vec{r}\right) = -\frac{2\omega e}{c^2\gamma}\exp\left[\frac{i\omega L}{4c\gamma^2}\right]\frac{\vec{r}}{r}K_1\left(\frac{\omega r}{c\gamma}\right) - \frac{2\omega e}{c^2\gamma}\frac{\vec{r}}{r}\exp\left[-\frac{i\omega L}{4c\gamma^2}\right] \times \exp\left[\frac{i\omega r^2}{2cL}\right]\frac{\omega}{cL}\int_0^\infty dr' r' K_1\left(\frac{\omega r'}{c\gamma}\right) J_1\left(\frac{\omega r r'}{cL}\right)\exp\left[\frac{i\omega r'^2}{2cL}\right], \quad (133)$$

which is valid for any value of ϕ. Exactly as in the case treated in Section 5, one may deal with two asymptotes of the theory for $\phi \gg 1$ and $\phi \ll 1$.

In the case $\phi \gg 1$ the contribution from the upstream source in Eq. (133) can be calculated analytically. In fact, the K_1 function under the integral sign is responsible for an exponential suppression of the integrand in the limit for $r' \gg \gamma\lambda$. As a result, we can integrate up to values $r' \lesssim \gamma\lambda$ without changing the integration result. This means that the phase factor in the integrand will be at most of order $1/\phi \ll 1$, and can be neglected. The result

of the integration then corresponds to the expression for a single edge in the far-zone, Eq. (41), the only difference being that the single-edge source is located at $z = -L/2$. Altogether, for $\phi \gg 1$, Eq. (133) simplifies to:

$$\vec{\vec{E}}\left(\frac{L}{2},\vec{r}\right) = -\frac{2\omega e}{c^2\gamma}\exp\left[\frac{i\omega L}{4c\gamma^2}\right]\frac{\vec{r}}{r}K_1\left(\frac{\omega r}{c\gamma}\right) - \frac{2e}{c}\frac{\gamma^2\vec{r}}{(\gamma^2 r^2 + L^2)}\exp\left[-\frac{i\omega L}{4c\gamma^2}\right]\exp\left[\frac{i\omega r^2}{2cL}\right] . \tag{134}$$

Eq. (134) is valid for $r \ll L\sqrt[3]{\lambda\!\!\!^{-}/R}$, i.e. for angles (measured from the upstream edge at $z = -L/2$) smaller than the angle of SR from the bend. When $r \ll \gamma\lambda\!\!\!^{-}$, the K_1 term is obviously dominant with respect to the second (polynomial) term in r. When $r \gtrsim \gamma\lambda\!\!\!^{-}$, the K_1 term drops exponentially, while the second term is zero at $r = 0$, grows polynomially and reaches its maximum at $r \sim L/\gamma$. Since the polynomial growth is slower than the exponential decrease of the K_1 term, one will have a region $\gamma\lambda\!\!\!^{-} \lesssim r \ll L/\gamma$ where the field is strongly suppressed with respect to the maximum at $r \sim L/\gamma$. In this region, the K_1 term is still a good approximation to the total field. As a result, the first term in Eq. (134) can be taken as a good approximation for the total field when $r \ll L/\gamma$ (always assuming $\phi \gg 1$). In this asymptotic case, results from our analysis coincide with usual results from TR theory. Note that the question about how many photons will be collected strongly depends on the acceptance of the optical system. The first term in Eq. (134) is singular at $r = 0$, so that the larger the acceptance, the nearest to the singularity we collect photons, and the largest the number of photons is.

The opposite asymptote for $\phi \ll 1$ can be described by applying the propagation formula, Eq. (14), to Eq. (30), like it was done for Eq. (32). When z is fixed at the mirror position, i.e. at $z = L/2$ one obtains [57]

$$\vec{\vec{E}}\left(\frac{L}{2},\vec{r}\right) = -\frac{2e}{c}\frac{\vec{r}}{r^2}\exp\left[\frac{i\omega r^2}{2cL}\right] . \tag{135}$$

The quadratic phase factor in Eq. (135) describes a spherical wavefront centered on the optical axis at the upstream edge (the initial bend). Note that this contribution scales as $1/r$ and is singular on-axis. The screen positioned at the downstream end of the setup will detect electric field given by the spherical wavefront in Eq. (135) at any value $\sqrt[3]{\lambda\!\!\!^{-}R^2} \ll L \ll \gamma^2\lambda\!\!\!^{-}$ from the upstream magnet and $r \ll L\sqrt[3]{\lambda\!\!\!^{-}/R}$.

Following the specification of the field (in amplitude and phase) at the target position, one faces the problem of propagation of BTR in free-space and through optical elements, which has been extensively discussed in

[51, 52, 53, 54, 55]. As mentioned above, this reduces to a standard Physical Optics problem, which is interesting within the field of Optical Engineering, i.e. from the viewpoint of the design of post-mirror collector optics. In these references, discussions are based on the assumption that a field distribution $K_1[\omega r/(\gamma c)]$, i.e. the Ginzburg-Frank formula, can be used. In this case, we deal with a laser-like beam, whose waist is located on the target (i.e. the target exhibits a plane wavefront). The transverse size of the waist is of order $\gamma\lambda\!\!\!^{-} \gg \lambda\!\!\!^{-}$, so that Fourier Optics can be applied to solve the propagation problem. The Rayleigh length of this laser-like beam is about $R_L \simeq \gamma^2\lambda\!\!\!^{-}$, and the Fresnel diffraction-zone is located at distances from the mirror of order R_L. When the distance from the mirror becomes much larger than R_L one has the Fraunhoffer diffraction-zone. If some linear optical element is located at a given position after the mirror, one can use available wavefront propagation/physical optics codes (e.g. SRW [25], ZEMAX [58], GLAD [59], PHASE [60]) for calculations. In other words, the propagation problem is well-defined, and does not include any novel aspect from a scientific viewpoint. Only, one needs to put attention to special terminology and notations used in literature, which may lead to some misunderstanding. For example, the Rayleigh length $R_L \sim \gamma^2\lambda\!\!\!^{-}$ is named "the formation length". Since the waist is always given by $w_0 \simeq \sqrt{L_f\lambda\!\!\!^{-}}$, it follows that $R_L \sim w_0^2/\lambda\!\!\!^{-} = L_f$. However, it should be noted that, conceptually, the formation length can only be discussed in connection with the particle trajectories, and not in free-space. Similarly, the Fresnel diffraction-zone is usually named as the "pre-wave zone", while the Fraunhoffer diffraction-zone is called "wave-zone".From this viewpoint, articles dealing with pre-wave-zone effects actually treat a routine Optical Engineering problem.

It should be remarked that the problem of specifying the field at a mirror position is fundamentally different from what we have done in the previous Sections. Before we considered a system composed by a straight section between two magnets, and radiation was detected downstream of the last magnet. That setup could be treated entirely within a SR-theory approach, and computer codes like SRW could be used to cross-check our results. Here the situation is different. In fact, Eq. (11) must now include integration up to a position z where sources are present

$$\vec{\vec{E}} = \frac{4\pi e}{c}\int_{-L/2}^{L/2} dz' \left[\vec{\nabla}'_{\perp} G\left(\vec{r}-\vec{r}', z-z'\right)\right]_{\vec{r}'=\vec{r}_0(z')} \exp\left[i\omega\left(\frac{s(z)}{v}-\frac{z}{c}\right)\right], \qquad (136)$$

with $z = L/2$, and therefore includes a singularity. In analogy with Eq. (90) one then obtains Eq. (133), where the singularity is isolated in the first field-term, which is entangled with sources, whereas the second term is disentangled.

Note that in the mathematical limit for $\rho \longrightarrow \infty$, Eq. (90) reduces to Eq. (133). Similarly, Eq. (40) reduces to Eq. (133) at $z = L/2$. However, although formally similar, Eq. (90) and Eq. (40) have different physical meaning compared to Eq. (133). In this Section we are characterizing the field *along the straight section*. This gives a different status e.g. to the singularity in Eq. (133) for $r = 0$ and $z = L/2$ compared to the singularity in Eq. (40), also located at $r = 0$ and $z = L/2$. In fact, the singularity in Eq. (40) (which reduces to Eq. (32) in the case $\phi \ll 1$) is related with the sharp-edge approximation: δ has a finite value, and going beyond the accuracy of the sharp-edge approximation (i.e. modelling the edges and accounting for their contribution to the radiation) the integrated flux will not diverge, nor the reconstructed field from the far zone data will. In contrast to this, the singularity in the K_1 term in Eq. (133) at $r = 0$ and $z = L/2$ is due to the fact that the plane at $\hat{z} = L/2$ intercepts the electron trajectory at that point, and is fundamentally related with our model of the electron beam as a filament without transverse dimensions.

9.2 Impact on setups at XFEL facilities

During the last decade, the electron beam energy in linac-based facilities increased up to around 10 GeV and novel effects, which were considered negligibly small at lower energies, became important. In fact, at high energies, condition $L \gg \gamma^2 \lambda\!\!\!^{-}$ becomes unpractical even for optical wavelengths, and the effect of the presence of an upstream bending magnet on TR emissions must be considered. Moreover, when measuring the long-wavelength coherent BTR, i.e. when the radiation wavelength is comparable to, or longer than the electron bunch length, the influence of the upstream bending magnet could be significant even at lower energies. These facts led to several misconceptions that can be found till recently.

An example of application for diagnostic purposes in XFEL setups is given in [47]. In general, monitoring methods based on coherent radiation take advantage of the sensitivity of the coherent spectrum on the bunch form factor, which is related to the bunch length. Coherent radiation from a given setup is thus collected with the help of mirrors and its energy measured, for example with the help of pyroelectric detectors. In order to analyze results, one has to characterize the field distribution at the collecting mirror position.

The setup proposed in [47] uses the last bend in each magnetic compression chicane of LCLS as depicted in Fig. 27. Radiation is collected by a mirror with a hole (that has to be large enough to let the electron beam through) and imaged to the diagnostic station. The hole mirror is positioned after a short straight section, a few tens of centimeters long. Detailed parameters can be

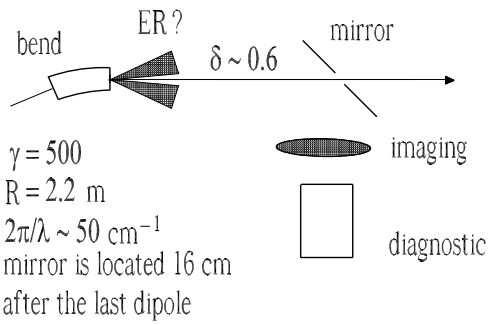

Fig. 27. Layout of the LCLS bunch length monitor, located immediately after the last dipole of the first magnetic bunch compressor.

found in [47]. In the case of the BC1 chicane, for example, the length of the straight section between magnet and mirror is $L = 0.16$ m, the wavelength of interest is of order [7] $\lambda \sim 1$ mm, the electron energy is about 250 MeV, and the radius of the bend is about $R \simeq 2.2$ m.

In [47] one can read: "the critical wavelength of the synchrotron radiation is orders of magnitude smaller than the wavelength range considered here for the bunch length monitor and the synchrotron radiation can be neglected compared to edge radiation". Authors of [47] stress the fact that $\lambda\!\!\!^{-} \gg \lambda\!\!\!^{-}_c$. Such condition is absolutely necessary to satisfy the applicability of ER theory. However, as we have seen, it is not sufficient, as the extra-requirement $\delta \ll 1$ must be satisfied too. If we calculate the parameter $\delta = \sqrt[3]{R^2 \lambda\!\!\!^{-}}/L$ for numbers given above we obtain $\delta \simeq 0.6$. We conclude that synchrotron radiation from the bend cannot be neglected: on the contrary, its effect will be as important as those from the straight section. The sharp-edge approximation fails here.

Note that there are two contributions to the field at the mirror position. The first is the contribution due to bending magnet radiation, while the second is the contribution due to the straight section. The fact that $\delta \simeq 0.6$ indicates that both contributions are of the same order of magnitude. It follows that it is incorrect to neglect the bending magnet contribution. Assuming that calculation of the straight section contribution is performed correctly, this would lead to a quantitatively incorrect numerical result from the viewpoint of practical applications. However, authors of [47] calculate the straight section contribution incorrectly as well. Let us consider the ϕ parameter. The reader may check that in this case the formation length $\gamma^2 \lambda\!\!\!^{-} \simeq 50$ m is much longer than the length of the straight section $L = 0.16$ m, so that $\phi \ll 1$. Therefore, Eq. (135) should be used to calculate the straight-section contribution at the mirror position. Authors of [47] proceed instead

[7] Since we are talking about coherent radiation, the reduced characteristic wavelength $\lambda\!\!\!^{-}$ is related here with the longitudinal size of the bunch σ_{rms}, i.e. $\lambda\!\!\!^{-} \simeq \sigma_{rms}$.

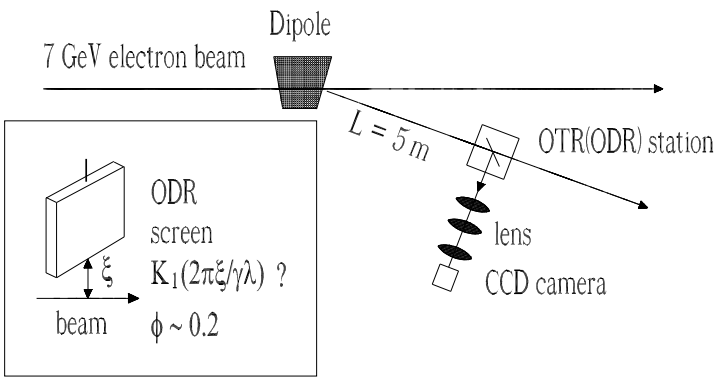

Fig. 28. ODR setup at the APS facility. In this experiment, ODR at visible wavelength is emitted for impact parameter ξ between 1 mm and 2 mm, values close to the Lorentz factor γ times the reduced observation wavelength.

in the following way. First, they recognize that for ER "the Coulomb field is the radiation source due to the sudden change in acceleration". Second, they propagate a K_1 source from the edge of the magnet up to the mirror "by expressing the Coulomb field as a sum of Gauss-Laguerre modes". This corresponds to the second term of Eq. (133). In other words, the field distribution at the mirror position is obtained by propagating a K_1 source located at the upstream bending magnet. It follows that the result in [47] is qualitatively incorrect.

To sum up, in [47], SR from the bending magnet is incorrectly neglected, and in the calculation of ER the downstream source, the first term of Eq. (133), is missed, qualitatively changing the result. The correct procedure to find the field distribution at the mirror for this parameter values ($\delta \sim 1$, $\phi \ll 1$) is to use Eq. (135) to calculate the straight-section contribution at the mirror position, and to sum up the SR contribution from the bending magnet.

We now turn to analyze [48, 49], where a setup similar to that in Fig. 28 is studied from an experimental viewpoint. An electron bunch travels a straight section of length $L \simeq 5$ m downstream of a bending magnet before intercepting an offset mirror at the ODR station. The wavelength considered here is $\lambda \simeq 800$ nm, and the electron energy is 7 GeV. In this case $\gamma^2 \lambda\!\!\!^{-} \simeq 30$ m, i.e. $\phi \simeq 0.17$. Authors of [48, 49] use a downstream virtual source $\sim K_1[\xi/(\gamma \lambda\!\!\!^{-})]$ to characterize the field at the BDR screen, effectively describing an ER setup by means of usual Ginzburg-Frank expression [50] for TR. However, here $\delta \ll 1$ and $\phi \ll 1$. As we have seen before, in this parameter range the correct procedure to evaluate the field distribution at the mirror is to use Eq. (135), which is different from the Ginzburg-Frank expression. In other words, in this parameter-range, the Ginzburg-Frank formula cannot be applied anymore.

Note that in [48] is reported that "the ODR peak signal intensity depen-

dence is consistent with $\exp[-2d/(\gamma\lambda\!\!\!^{-})]$, where d is the distance from beam center to the screen edge, γ is the Lorentz factor". However, in this region of parameters the asymptotic behavior in Eq. (135), does not exhibit any exponential cutoff, nor dependence on $\gamma\lambda\!\!\!^{-}$. Therefore, the interpretation of experimental result in [48] cannot be accepted.

This example and that in [47] help to understand the importance of edge-radiation theory in relation with future XFEL facilities. They also demonstrate the usefulness of similarity techniques in the efficient planning of experimens.

10 Conclusions

In this article we showed how the theory of laser beams can be used to characterize radiation field associated with any Edge Radiation (ER) setup. In fact, in the space-frequency domain, ER beams can be described in terms of laser-like beams, with large transverse dimensions compared to the wavelength. Similarly to usual laser beams, ER beams were shown to exhibit a virtual "waist" with a plane wavefront. The field distribution of ER across the waist turned out to be strictly related to the inverse Fourier transform of the angular field-distribution in the far-zone. As a result, standard Fourier Optics techniques could be taken advantage of, and the field could be propagated to characterize ER beams at any position down the beamline. In particular, we reconstructed the near-field distribution from the knowledge of the far-field ER pattern. This could be accomplished by (i) describing the far-field pattern with known analytical formulas, (ii) finding the virtual source(s) and (iii) propagating the virtual source distribution in the near (and far) zone.

After a qualitative discussion in Section 2, we applied our techniques to a typical setup constituted by a straight section between bends in Sections 3, 4 and 5. These Sections constitute the first comprehensive treatment of ER, in the sense that we consistently used similarity techniques for the first time, allowing discussion and physical understanding of many asymptotes of the parameter space together with their region of applicability. In particular, the main parameters of the theory are found to be δ, the ratio between the bends formation length and the straight section length, and ϕ, the ratio between the length of the straight section and the maximal formation length of ER. Note that introduction of the parameter δ allowed us to define for the first time "how sharp" the edges are, and to specify the region of applicability of ER theory. A classification of regions of observation of interest, which is regarded by us as a novel result, is presented in Section 5.3 with the help of dimensionless parameters.

In Section 6 we applied our treatment to deal with a Transition Undulator Radiation (TUR) setup. As before, we relied on virtual source expressions derived from the far-field pattern. These virtual sources were propagated in free-space in the near zone, thus providing for the first time an exact analytical characterization of TUR in the near zone.

In the following Section 7 we presented the first exhaustive theory of ER within a waveguide. The analysis of the problem was performed by introducing a tensor Green's function technique. This complicates the mathematical structure of equations that depends, contrarily to the unbounded-space case, on the waveguide geometry. We outlined a solution for a homogeneous waveguide with arbitrary cross-section, further specializing it to the case of a circular waveguide. The electric field was found as a superposition of waveguide modes, and was studied for different values of parameters. The main parameter involved in the problem (other than ϕ, δ and $\hat{z}$) was found to be a waveguide parameter Ω, related with the strength of guiding effects. This can be interpreted (at $\phi \ll 1$) as the ratio between the waveguide radius and the radiation diffraction size, and is a purely geometrical parameter.

In Section 8 we presented considerations on the coherent emission of ER. The availability of a large number of photons constitutes an important advantage of coherent ER compared to the incoherent case when this type of radiation is used as a diagnostic tool, where characteristics of the electron bunch can be measured, and electron-beam microbunching can be investigated too.

Finally, in Section 9 we discussed the problem of extraction of ER by a mirror, stressing differences and analogies that this kind of setup presents, compared to those discussed in the previous Sections. Particular attention was given to diagnostics setups for XFEL facilities.

As a final remark, it should be noted that in our work we consistently exploited both theoretical and numerical results from simulation. These approaches are complementary, and we first took advantage of such complementarity. On the one hand, there are situations when existing codes cannot be applied, e.g. the case of a waveguide (Section 7) and the characterization of the field distribution at a mirror position (Section 9), where part of the field is entangled with the sources. In this case, analytical results can be used for practical calculations. On the other hand, computer codes can easily account for finite bending magnet edge length (finite value of δ) in a particular set of problem parameters. From this viewpoint, our theory can be used to prepare, based on similarity techniques, particular sets of problem parameters to be used as input for computer codes, which subsequently return universal plots presenting the accuracy of ER theory in terms of dimensionless parameters.

Acknowledgements

We thank our DESY collegues Martin Dohlus, Michael Gensch and Petr Ilinski for many useful discussions, Massimo Altarelli , Reinhard Brinkmann and Edgar Weckert for their interest in this work.

Appendix: Equivalence of Eq. (90) and Eq. (84)

We want to show that Eq. (90), together with Eq. (87), is equivalent to Eq. (84). We can demonstrate this fact by calculating the sum in Eq. (84), and presenting it in terms of an integration.

We begin expanding the $\mathrm{sinc}(X) = \sin(X)/X$ function in terms of exponential functions. Moreover, we subtract from X in the denominator of $\sin(X)/X$ an infinitesimally small quantity $i\epsilon$, where $\epsilon > 0$, to be dropped at the end of calculations. In other words, we substitute $1/X$ with $1/(X - i\epsilon) = i\int_0^\infty d\xi \exp[-iX\xi - \epsilon\xi]$. We therefore obtain

$$\vec{\tilde{E}} = -\frac{ieL}{\omega\rho^3}\int_0^\infty d\xi \exp\left[-i\frac{\omega L\xi}{4c\gamma^2} - \epsilon\xi\right]\sum_{k=1}^\infty \frac{\nu_{0k}}{J_1^2(\nu_{0k})} \times\left\{\exp\left[\frac{i\omega L}{4c\gamma^2}\right] - \exp\left[-\frac{i\omega L}{4c\gamma^2} - \frac{iL\nu_{0k}^2 c}{2\omega\rho^2}\right]\right\} J_1\left(\frac{\nu_{0k} r}{\rho}\right)\exp\left[-i\frac{\nu_{0k}^2 cL\xi}{4\omega\rho^2}\right]\vec{e}_r\,. \tag{137}$$

Eq. (137) consists of two field terms, corresponding to the two terms inside the {...} parenthesis. Let us consider the first term and demonstrate that such term is in fact a generalization of the virtual source at $z = L/2$ (i.e. Eq. (39) for $z_s = L/2$) accounting for the presence of the waveguide. Using the fact that $J_1(X) = I_0'(iX)/i$, the "'" symbol indicating derivative with respect to the argument, and remembering the Wronskian relation $1/X = I_0(X)K_1(X) + I_1(X)K_0(X)$, we have

$$\frac{1}{J_1(\nu_{0k})} = \frac{2\omega\rho^2}{cL}[I_1(i\nu_{0k})K_0(i\nu_{0k})]\left[\frac{d}{d\eta}I_0\left(\sqrt{-i\frac{4\omega\rho^2\eta}{cL}}\right)\right]^{-1}_{\eta=-icL\nu_{0k}^2/(4\omega\rho^2)}\,. \tag{138}$$

Using Eq. (138) and remembering $J_1(X) = I_1(iX)/i$ we write the first term in Eq. (137) as

$$\vec{\vec{E}}_1 = -i\frac{eL}{\omega\rho^3}\int_0^\infty d\xi \exp\left[-i\frac{\omega L\xi}{4c\gamma^2} - \epsilon\xi\right]\sum_{k=1}^\infty \left[\frac{d}{d\eta} I_0\left(\sqrt{-i\frac{4\omega\rho^2\eta}{cL}}\right)\right]^{-1}_{\eta=-icL\nu_{0k}^2/(4\omega\rho^2)}$$
$$\times\frac{2\omega\rho^2\nu_{0k}}{cL}K_0(i\nu_{0k})\exp\left[\frac{i\omega L}{4\gamma^2 c}\right]I_1\left(i\frac{\nu_{0k}r}{\rho}\right)\exp\left[-i\frac{\nu_{0k}^2 cL\xi}{4\omega\rho^2}\right]\vec{e}_r\,. \qquad (139)$$

We now consider the integral

$$u = \int_{O_1} d\eta \exp[\eta\xi]\frac{\sqrt{-i\eta}}{I_0\left(\sqrt{-i\frac{4\omega\rho^2\eta}{cL}}\right)}\left[I_1\left(\sqrt{-i\frac{4\omega\rho^2\eta}{cL}}\frac{r}{\rho}\right)K_0\left(\sqrt{-i\frac{4\omega\rho^2\eta}{cL}}\right)\right.$$
$$\left.+I_0\left(\sqrt{-i\frac{4\omega\rho^2\eta}{cL}}\right)K_1\left(\sqrt{-i\frac{4\omega\rho^2\eta}{cL}}\frac{r}{\rho}\right)\right]\,, \qquad (140)$$

where O_1 is an integration path on the complex η plane going from $\gamma' - i\infty$ to $\gamma' + i\infty$, $\gamma' > 0$ being a positive number larger than the real part of all singularities of the integrand, and closed by a semicircle of infinite radius in the left half plane. It can be shown that the integrand is a single valued function of η. It follows that u can be calculated as a sum of residues of first order poles located at $\eta = \eta_k = -i\lambda\!\!\!^{-}L\nu_{0k}^2/(4\rho^2)$. We obtain

$$-\frac{2\rho^3\omega^{3/2}}{\pi(cL)^{3/2}}u = \sum_{k=1}^\infty \frac{2\omega\rho^2\nu_{0k}}{cL}K_0(i\nu_{0k})\exp\left[-i\frac{\nu_{0k}^2 cL\xi}{4\omega\rho^2}\right]I_1\left(i\frac{\nu_{0k}r}{\rho}\right)$$
$$\times\left[\frac{d}{d\eta}I_0\left(\sqrt{-i\frac{4\omega\rho^2\eta}{cL}}\right)\right]^{-1}_{\eta=-icL\nu_{0k}^2/(4\omega\rho^2)}\,, \qquad (141)$$

that can be immediately substituted in Eq. (139). The integral along the semicircle in Eq. (140) can be dropped using Jordan's lemma. Therefore

$$\vec{\vec{E}}_1 = \frac{2ie\sqrt{\omega}}{\pi\sqrt{Lc}}\exp\left[\frac{i\omega L}{4\gamma^2 c}\right]\int_0^\infty d\xi \exp\left[-i\frac{\omega L\xi}{4c\gamma^2} - \epsilon\xi\right]\int_{\gamma'-i\infty}^{\gamma'+i\infty} d\eta \exp[\eta\xi]$$
$$\times\frac{\sqrt{-i\eta}}{I_0\left(\sqrt{-i\frac{4\omega\rho^2\eta}{cL}}\right)}\left[I_1\left(\sqrt{-i\frac{4\omega\rho^2\eta}{cL}}\frac{r}{\rho}\right)K_0\left(\sqrt{-i\frac{4\omega\rho^2\eta}{cL}}\right)\right.$$
$$\left.+I_0\left(\sqrt{-i\frac{4\omega\rho^2\eta}{cL}}\right)K_1\left(\sqrt{-i\frac{4\omega\rho^2\eta}{cL}}\frac{r}{\rho}\right)\right]\vec{e}_r\,. \qquad (142)$$

Eq. (142) is easily seen to be the Laplace transform of an inverse Laplace transform. Letting $\epsilon \longrightarrow 0$, it follows straightforwardly that

$$\vec{\vec{E}}_1 = -\frac{2\omega e}{c^2\gamma}\exp\left[\frac{i\omega L}{4\gamma^2 c}\right]\left[K_1\left(\frac{\omega r}{c\gamma}\right) + \frac{K_0\left(\frac{\omega\rho}{c\gamma}\right)}{I_0\left(\frac{\omega\rho}{c\gamma}\right)}I_1\left(\frac{\omega r}{c\gamma}\right)\right]\vec{e}_r\,. \tag{143}$$

Eq. (143) is a generalization for the virtual source located at $z = L/2$ that accounts for the presence of a waveguide (compare with Eq. (87)).

Let us now consider the second term in Eq. (137), which can also be written as

$$\vec{\vec{E}}_2 = \frac{eL}{\omega\rho^3}\sum_{k=1}^{\infty}\frac{\nu_{0k}}{J_1^2(\nu_{0k})}\exp\left[-\frac{i\omega L}{4c\gamma^2} - \frac{iL\nu_{0k}^2 c}{2\omega\rho^2}\right]\frac{1}{\frac{\omega L}{4c\gamma^2} + \frac{L\nu_{0k}^2 c}{4\omega\rho^2}}J_1\left(\frac{\nu_{0k}r}{\rho}\right)\vec{e}_r\,. \tag{144}$$

Since

$$\begin{aligned}&\int_0^{\rho} dr'\; r' K_1\left(\frac{\omega r'}{c\gamma}\right)J_1\left(\frac{\nu_{0k}r'}{\rho}\right) = \\ &\left[\frac{c\gamma\nu_{0k}}{\omega\rho} + \nu_{0k}J_2(\nu_{0k})K_1\left(\frac{\omega\rho}{c\gamma}\right) - \frac{\omega\rho}{c\gamma}J_1(\nu_{0k})K_2\left(\frac{\omega\rho}{c\gamma}\right)\right]\Bigg/\left(\frac{\omega^2}{\gamma^2c^2} + \frac{\nu_{0k}^2}{\rho^2}\right),\end{aligned} \tag{145}$$

and

$$\begin{aligned}&\int_0^{\rho} dr'\; r' I_1\left(\frac{\omega r'}{c\gamma}\right)J_1\left(\frac{\nu_{0k}r'}{\rho}\right) = \\ &\left[\frac{\omega\rho}{c\gamma}I_2\left(\frac{\omega\rho}{c\gamma}\right)J_1(\nu_{0k}) + \nu_{0k}I_1\left(\frac{\omega\rho}{c\gamma}\right)J_2(\nu_{0k})\right]\Bigg/\left(\frac{\omega^2}{\gamma^2c^2} + \frac{\nu_{0k}^2}{\rho^2}\right),\end{aligned} \tag{146}$$

one can write Eq. (144) as

$$\vec{\vec{E}}_2\left(\frac{L}{2},\vec{r}\right) = \frac{4\omega e}{\rho^2c^2\gamma}\sum_{k=1}^{\infty}\frac{1}{J_1^2(\nu_{0k})}\exp\left[-\frac{i\omega L}{4c\gamma^2} - \frac{iL\nu_{0k}^2 c}{2\omega\rho^2}\right]$$

$$\times \int_0^{\rho} dr'\, r' \left[K_1\left(\frac{\omega r'}{c\gamma}\right) + \frac{K_0\left(\frac{\omega\rho}{c\gamma}\right)}{I_0\left(\frac{\omega\rho}{c\gamma}\right)} I_1\left(\frac{\omega r'}{c\gamma}\right) \right] J_1\left(\frac{\nu_{0k} r}{\rho}\right) J_1\left(\frac{\nu_{0k} r'}{\rho}\right) \vec{e}_r \,, \tag{147}$$

because the second and the third terms on the right hand side of Eq. (145) cancel with Eq. (146) multiplied by $K_0(\omega\rho/(c\gamma))/I_0(\omega\rho/(c\gamma))$. Remembering that an expression for the field propagation from some initial point z_i to some final point z_f is given by Eq. (88), one finds that Eq. (147) is obtained by propagating the field distribution

$$\vec{\tilde{E}}\left(-\frac{L}{2}\right) = \frac{2\omega e}{c^2\gamma} \exp\left[-\frac{i\omega L}{4c\gamma^2}\right] \left[K_1\left(\frac{\omega r}{c\gamma}\right) + \frac{K_0\left(\frac{\omega\rho}{c\gamma}\right)}{I_0\left(\frac{\omega\rho}{c\gamma}\right)} I_1\left(\frac{\omega r}{c\gamma}\right) \right] \vec{e}_r \tag{148}$$

up to $z_f = L/2$. This can be seen with the help of Eq. (81), selecting $m = 0$.

Now, Eq. (148) is just a generalized expression, valid in the presence of a waveguide, for a virtual source at $z = -L/2$, which is described similarly to Eq. (143), the difference being only its location position.

It follows that the second term in Eq. (137) is obtained propagating the virtual source at $z = -L/2$ up to position $z = L/2$, that is the second term of Eq. (90).

References

[1] M.M. Nikitin, A.F. Medvedyev, M.B. Moiseyev, and V. Ya. Epp, Sov. Phys. JETP, 52, 388 (1980)

[2] M.M. Nikitin, A.F. Medvedyev and M.B. Moiseyev, IEEE Trans. Nucl. Sci. NS-28,3, 3130 (1981)

[3] E.G. Bessonov, Sov. Phys. Tech. Phys., 28, 837 (1983)

[4] Yu. A. Bashmakov, Rev. Sci. Instrum, 63, 1, 343 (1992)

[5] O.V. Chubar and N.V. Smolyakov, J. Optics (Paris), 24, 117 (1993)

[6] O.V. Chubar and N.V. Smolyakov, in Proceedings of PAC93, 1626 (1993)

[7] R.A. Bosch et al., Rev. Sci. Instrum. 67, 3346 (1995)

[8] R.A. Bosch and O.V. Chubar, "Long wavelength edge radiation in an electron storage ring", Proc. SRI'97, tenth US National Conference, AIP Conf. Proc. 417, edited by E. Fontes (AIP, Woodbury, NY), pp. 35-41 (1997)

[9] R.A. Bosch, Il Nuovo Cimento, 20, 4 p. 483 (1998)

[10] R.A. Bosch, Nucl. Instr. Meth. Phys. Res. A, 431 (1999) 320

[11] Y.-L. Mathis et al. Phys. Rev. Lett. 80, 6, 1220 (1998)

[12] P. Roy, J-B. Brubach et al., Nucl. Instr. Meth. Phys. Res. A, 426 (2001)
[13] R.A. Bosch, R.A. Bosch, Nucl. Instr. Meth. Phys. Res. A, 492, 284 (2002)
[14] R.A. Bosch, Nucl. Instr. Meth. Phys. Res. A, 482, 789 (2002)
[15] G. Geloni, E. Saldin, E. Schneidmiller and M. Yurkov, Optics Communications 276, 1 (2007), 167
[16] K.-J. Kim, Phys. Rev. Lett. 76, 8 (1996)
[17] B.M. Kincaid, Il Nuovo Cimento Soc. Ital. Fis, 20D, 495 (1998) and LBL-38245 (1996)
[18] M. Castellano, Nucl. Instr and Meth. in Phys. Res. A 391 (1997) 375
[19] R.A. Bosch, Nucl. Instr. Meth. Phys. Res. A, 386 (1997) 525
[20] P. Roy et al. Phys. Rev. Lett. 84, 3 (2000)
[21] M. Altarelli et al. (Eds.), XFEL: The European X-Ray Free-Electron Laser. Technical Design Report, DESY 2006-097, DESY, Hamburg (2006) (See also http://xfel.desy.de)
[22] J. Arthur et al. Linac Coherent Light Source (LCLS). Conceptual Design Report, SLAC-R593, Stanford (2002) (See also http://www-ssrl.slac.stanford.edu/lcls/cdr)
[23] Tanaka, T. & Shintake, T. (Eds.): SCSS X-FEL Conceptual Design Report. Riken Harima Institute, Hyogo, Japan, May 2005 (see also http://www-xfel.spring8.or.jp)
[24] G. Geloni, E. Saldin, E. Schneidmiller and M. Yurkov, Opt. Commun. 281, 3762 (2008)
[25] O. Chubar, P.Elleaume and A. Snigirev , Nucl. Instr. Meth. Phys. Res. A, 435, 495 (1999)
[26] D. Bilderback, P. Elleaume and E. Weckert, J. Phys. B: At. Mol. Opt. Phys. 38, 773 (2005)
[27] K.-J. Kim, "Characteristics of Synchrotron Radiation" in Phys. of Part. Acc. 184, AIP Conf. Proc., Am. Inst. of Phys., New Yourk (1984)
[28] G. P. Williams, Rep. Prog. Phys. 69, 301 (2006)
[29] Y. Takayama and S. Kamada, Phys. Rev. E, 59, 6, 7128 (1999)
[30] G. Geloni, E. Saldin, E. Schneidmiller and M. Yurkov, "Paraxial Green's functions in SR theory", DESY 05-032, ISSN 0418-9833 (2005)
[31] J. Jackson, "Classical Electrodynamics", 3rd ed., Wiley, New York (1999)
[32] G. Geloni, E. Saldin, E. Schneidmiller, M. Yurkov, Nucl. Instr. Meth. Phys. Res. A, 584, 1,219 (2008)
[33] E. Saldin, E. Schneidmiller and M. Yurkov, "The Physics of Free Electron Lasers", Springer, Berlin, 2000, ISBN 3-540-66266-9
[34] E. Saldin, E. Schneidmiller and M. Yurkov, Nucl. Instrum. Meth. Phys. Res. A 445, 40 (2000)
[35] S. A. Heifets, Phys. Rev. D, 40, 9, 2097 (1989)
[36] Y. Shibata et al. Phys. Rev. E, 49, 1, 785 (1994)
[37] J. Zheng et al., Physics of Plasmas, 10, 7, 2994 (2003)
[38] C.B. Schroeder et al., Phys. Rev. E 69, 016501 (2004)
[39] G. L. Orlandi, Opt. Commun. 211, 109 (2002)
[40] G. L. Orlandi, Opt. Commun. 267, 322 (2006)

[41] G. L. Orlandi, Proc. FEL2005, 27th International Free Electron Laser Conference, H.-D. Nuhn Ed., 576 (2005)
[42] E.L. Saldin, E.A. Schneidmiller and M.V. Yurkov, Nucl. Instr. and Meth. Phys. Res. A 490, 1 (2002))
[43] S. Heifets, G. Stupakov and S. Krinsky, Phys. Rev. ST AB 5, 064401 (2002)
[44] Z. Huang and K.-J. Kim, Phys. Rev. ST AB 5, 074401 (2002)
[45] E.L. Saldin, E.A. Schneidmiller and M.V. Yurkov, Nucl. Instr. and Meth. Phys. Res. A, 528, 355 (2004)
[46] E.L. Saldin, E.A. Schneidmiller and M.V. Yurkov, Nucl. Instr. and Meth. Phys. Res. A 539, 3 , 4999 (2005)
[47] H. Loos at al., "Relative bunch length monitor for the LINAC coherent light source (LCLS) using coherent edge radiation", in Proceedings of PAC07, Albuquerque, New Mexico, USA, 4189 (2007)
[48] A.H. Lumpkin et al., Phys. Rev. ST AB 10, 022802 (2007)
[49] C.-Y. Yao, A.H. Lumpkin and D.W. Rule in Proceedings of PAC07, Albuquerque, New Mexico, USA, FRPMS001, p. 3850 (2007)
[50] V.L. Ginzburg and I. M. Frank, Soviet Phys. JETP 16, 15 (1946)
[51] D.V. Karlovets and A.P. Potylitsyn, Nucl. Instr. and Meth. Phys. Res. B, in press, (2008), doi:10.1016/j.nimb.2008.02.014
[52] P. Karataev et al., Phys. Rev ST AB, 11, 032804 (2008)
[53] G.A. Naumenko, Nucl. Instr. and Meth. Phys. Res. B, 227, 87 (2005)
[54] P.V. Karataev, Physics Lett. A 245, 428 (2005)
[55] D. Süttelin et al., Nucl. Instr. and Meth. Phys. Res. B, 264, 361 (2007)
[56] G. Stupakov, Y. Ding and Z. Huang, "Calculation of the beam field in the LCLS bunch length monitor", SLAC-PUB-11890
[57] R. A. Bosch, Phys. Rev. ST AB 5, 020701 (2002)
[58] ZEMAX, Optical Design Program, Users Manual, ZEMAX Development Corporation (2005).
[59] GLAD, Theory Manual, Applied Optics Research, 1087 Lewis River Road, 217 Woodland, WA (2004).
[60] J. Bahrdt, Phys. Rev. ST Accel. Beams 10, 060701 (2007)